LARGE EDDY SIMULATIONS OF JET FLOW INTERACTIONS WITHIN ROD BUNDLES

A Thesis

by

NATHANIEL O. SALPETER

Submitted to the Office of Graduate Studies of
Texas A&M University
in partial fulfillment of the requirements for the degree of

MASTER OF SCIENCE

May 2010

Major Subject: Mechanical Engineering

LARGE EDDY SIMULATIONS OF JET FLOW INTERACTIONS WITHIN ROD BUNDLES

A Thesis

by

NATHANIEL O. SALPETER

Submitted to the Office of Graduate Studies of
Texas A&M University
in partial fulfillment of the requirements for the degree of

MASTER OF SCIENCE

Approved by:

Chair of Committee, Yassin A. Hassan
Committee Members, Kalyan Annamalai
William H. Marlow
Head of Department, Dennis L. O'Neal

May 2010

Major Subject: Mechanical Engineering

ABSTRACT

Large Eddy Simulations of Jet Flow Interactions Within Rod Bundles.

(May 2010)

Nathaniel O. Salpeter, B.S., University of Florida

Chair of Advisory Committee: Dr. Yassin A. Hassan

The present work investigates the turbulent jet flow mixing of downward impinging jets within a staggered rod bundle based on previous experimental work. The two inlet jets had Reynold's numbers of 11,160 and 6,250 and were chosen to coincide with the available data. Steady state simulations were initially carried out on a semi-structured polyhedral mesh of roughly 13.2 million cells following a sensitivity study over six different discretized meshes. Very large eddy simulations were carried out over the most refined mesh and continuous 1D wavelet transforms were used to analyze the dominant instabilities and how they propagate through the system in an effort to provide some insight into potential problems relating to structural vibrations due to turbulent instabilities. The presence of strong standing horseshoe vorticies near the base of each cylinder adjacent to an inlet jet was noted and is of potential importance in the abrasion wear of the graphite support columns of the VHTR if sufficient wear particles are present in the gas flow.

ACKNOWLEDGEMENTS

I would like to thank my committee chair, Dr. Yassin A. Hassan, and my committee members, Dr. William H. Marlow, and Dr. Kalyan Annamalai, for their guidance and support throughout the course of this research.

I have much gratitude for the constant assistance, advice, and encouragement of Dr. Hassan, and the assistance of all of my lab colleagues. Finally, I would like to thank my friends and family for their continual support of my education.

NOMENCLATURE

d,	distance to nearest wall
G_b,	bouyancy production term
G_k,	turbulent production term
h,	cell size
$\mathbf{S}$, $\overline{S_{ij}}$	strain rate tensor
S_{ij}^d,	deformation tensor
t,	time
T_{ij},	turbulent stress tensor strain rate tensor.
$\mathbf{v}$,	velocity
$\mathbf{v}_g$,	velocity component ‖ to gravity force
V,	cell volume
$\mathbf{W}$,	rotation rate tensor
Δ,	length Scale
ε,	rate of dissipation of turbulence kinetic energy
κ,	von Karman constant
η,	time scale ratio of the turbulence to the mean strain
μ,	viscosity
μ_t,	sub-grid scale turbulent viscosity
ρ,	density
Y_M,	dilatation dissipation
ω,	specific dissipation rate

TABLE OF CONTENTS

Page

Page

LIST OF FIGURES

Page

Page

Page

Page

Page

LIST OF TABLES

Page

1. INTRODUCTION

The push for safer and more efficient nuclear reactors with less margin for risk has resulted in the need for high fidelity numerical simulations of reactor designs. In order to achieve the necessary confidence level in the simulations being conducted using current computational fluid dynamics (CFD) techniques, it is paramount that numerical models be validated against experimental data representative of phenomena likely to appear within a nuclear power plant.

The focus of this study is partly on the validation of numerical models against results previously published by Amini and Hassan [1] but also on the identification of flow features seen in the numerical results for further investigation both experimentally and through CFD simulations. The experimental study was focused on jet impingement upon a lower plane within a bank of staggered rods parallel to the inlet jet axis, mimicking similar phenomena of the lower plenum of a very high temperature gas cooled reactor (VHTR). Two jets within the rod bundle were used with a single outlet to one side of the channel. This work details a numerical study aimed at making a contribution in the validation of numerical models for such nuclear applications by modeling the experimental facility within the Star-CCM+ v.3.06.006 CFD package and quantifying the level of agreement of the result with the experimental data. Additional analysis of the flow phenomenology seen in the CFD results was also performed. It is important to note that in the process of

---

This thesis follows the style of *International Journal of Heat and Fluid Flow.*

validating numerical models, the cases in which the models have discrepancies from the experimental results are just as important in the determination of model limits as are the results that match closely with the experimental data set.

In the case of mixing within the lower plenum mixing of the VHTR, the importance of such studies are to ensure the absence of hot streaking and hot spots as well as investigate possible locations of turbulence induced vibrations and abrasion within the support structure. Hot streaking is a phenomenon by which hot gas exits the reactor core and exhausts into the lower plenum but does not sufficiently mix prior to reaching the steam generator, thus causing hot spots within other plant components not specifically designed to handle such spikes in temperature.

One investigation at Sandia National Laboratory involves the numerical study of the effect of static helicoidal inserts inside the jet inlets in order to disrupt axial momentum and increase mixing [Rodriguez, El-Genk 2009]. This study looked at both jets with and without helicoidal inserts in the inlet jets; however, the focus of the work was on structures right in the wake of the jet as opposed to the present study in which structures within the rod bundle will be investigated as well.

Studies have been done involving axial flow along rod arrays in which ‘pulsing’ phenomena are found between closely spaced rods. One experimental study investigates channel flows with varying sized rods within it [Rehme K. 1989]. Spectral analysis of the same channel conditions was done a few years later and found very regular azimuthal component fluctuations between the rods [Möller 1992]. The present study has high velocity jet impingement on a lower plane rather

than a uniform cross flow. The similarity with the pulsations of flow between the previous study and this work is in the regions between adjacent rods as well as between rods and adjacent walls. In these locations there is an updraft from the impinged jet striking the wall and moving upwards in the small space between the rods and the wall. In locations of flow past cylindrical rods, the generation of turbulent instabilities presents a structural concern with respect to vibration in the support rods of the VHTR.

Jet impingement studies using numerical methods have suggested the presence of different modes of flow structure in the impinged flow [Li et al. 2005]. In their study, numerical results indicated the presence of two modes downstream of the impingement location. One was that the flow remained along the lower plane and in the other the flow separated from the lower plane and flowed freely within the domain. In the case of the present study, flow within the rod bundle remained in the regime where the flow remained in contact with the impingement plane until coming in contact with the adjacent rods.

The necking of the jet and formation of ring vorticies has been observed in experimental works for round jets in the same range of Reynolds numbers as the present work [F. Shu *et al.* 2005]. In the case of a jet that has a top-hat profile as opposed to a Gaussian profile, a reduced distance (x/D) to the onset of vortex rings has been documented [New *et al* 2006].

Muzzammil and Gangadhariah [2003] experimentally investigated the presence of the primary horseshoe vortex formed around the base of a pier column in a crossflow and the key role that is played by this vortex in the scouring of the loose

surrounding base material. Wear particles that are present in the gas flow after passing through the core may potentially act as an abrasive in locations with strong consistent vorticies over the lifespan of a reactor. Greeley and Iverson [1985] describe shadow zones as features observed in the wake of horseshoe vorticies just following an obstruction and before the onset of turbulent instabilities. This phenomenon of high inertia dust particles settling out of the bulk flow has been described by them as the reason for dust buildup just behind obstructions in windy conditions. When concerned with mixing levels, such dead zones should be kept in mind.

Work by Pardee [1967] investigated graphite dusting rates for brushes in electrical components and found that there is a strong dependence on atmosphere and moisture content. Pardee states that moisture absorbtion into graphite plays the largest role in the dusting phenomenon. Once a threshold moisture content in the atmosphere is exceeded, graphite dusting drops off drastically. Applying this line of reasoning to the VHTR, dry helium with very low levels of residual moisture would lead to a higher rate of dusting than would a flow with moisture content above this threshold. Additionally, helium is only physisorbed and not chemisorbed into the graphite, and only at very low temperatures [Lee and Johnson 1978] not seen in the VHTR. Chemisorbed molecules occupy the active sites of the exposed graphite; however, inert helium is not chemisorbed thus producing no absorption film which counter intuitively facilitates vapor absorption into the graphite [Savage 1948].

Unfortunately, the problem is not quite so simplistic. Additional moisture content in the helium would introduce a host of problems throughout the reactor and

steam generator and is therefore not a viable solution to the issue of dusting. The problem of suspended particles must be addressed in terms of the effect of particles in suspension as well as potential locations of coalescence. This study identifies potential locations of dust coalescence in a staggered rod bundle arrangement similar to that of the VHTR as well as locations of where graphite dust in the flow might act as wear particles and erode structural components in the lower plenum.

Ongoing experimental studies similar to that of Amini and Hassan have been recently performed at the matched index of refraction [MIR] facility at Idaho National Laboratory using a narrower channel [McIlroy Jr. *et al.* 2008]. The narrowed flow section is useful in studies of flows along the reflector wall of the lower plenum but eliminated flow features that are present away from the wall by the introduction of significant wall effects. The experimental data set of Amini and Hassan [2009] provides flow data for a wider range within the bundle as shown in Figure 1. This figure shows two planes within the 3D model and the difference in channel width between studies.

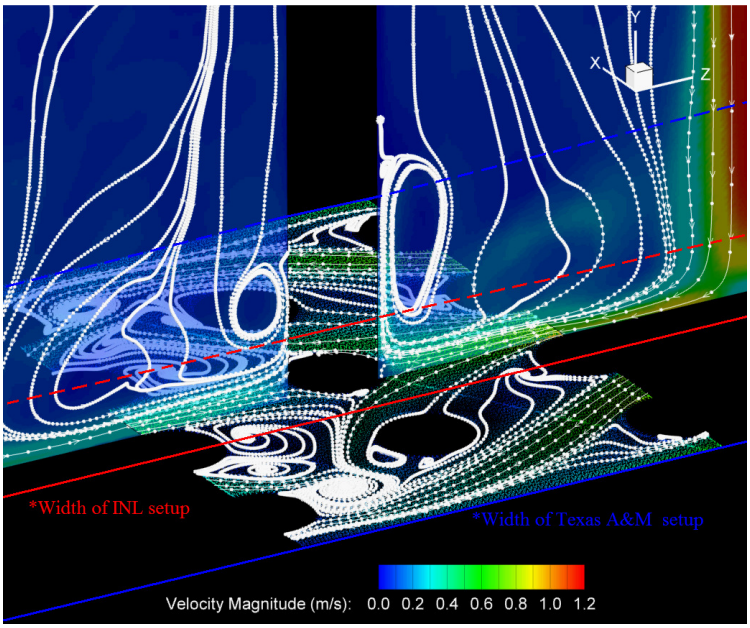

Figure 1. **Illustration of differences in experimental channel widths between Amini and Hassan's study and McIlroy Jr. *et al*'s**

Experimental flow visualization studies by Shu et al [2005] investigated the effect of nozzle shape on flow in water jets in the Reynolds number range of 5,000-10,000. In the case of the axis-symmetric round nozzle, the presence of strong Kelvin-Helmholtz instabilities in the range of 1-5 diameters was observed using the planar laser induced fluorescence (PLIF) technique as shown in Figure 2.

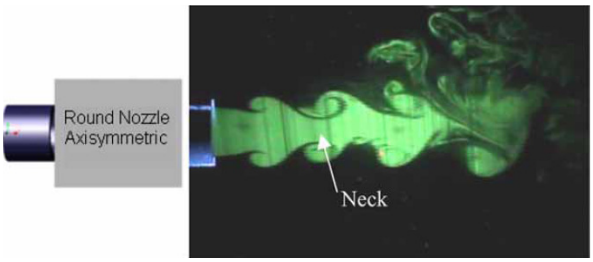

Figure 2. **Flow visualization of F. Shu *et al.*[2005] in which necking occurs in round jet of Re=5,000**

Numerous studies of vortex shedding following cylinders have been performed. Fey *et al.* [1998] developed a new Strouhal(St)-Reynolds number relationship based on experimental data for circular cylinders in uniform flows within the same Reynolds number range of interest as the present study. Other studies in the same Reynolds number range but of two in-line cylinders have been performed. Xu and Zhou [2004] found little to no detectable vortex shedding between the two cylinders for a distance of $L/d<2$; however, there was a rapid reduction in St behind the downstream cylinder as the gap increased from $1<L/d<2$. Angrilli *et al.* [1982] investigated the influence of close proximity walls on the Strouhal number. Their investigation concluded that the wall increases the Strouhal number slightly as it gets closer to the cylinder, thus increasing shedding frequency.

Vortex shedding frequency calculations using the equation for the Sr number should be approached with caution in the case of this study because of the non-uniformity of the flow field. The Strouhal-Reynolds number relationship developed by Roshko [1954] between Reynolds numbers of 300 and 10,000 gave a Strouhal number within 4% of the best fit of experimental data for uniform flow over a cylinder. While this error might be low for a linear approximation, the presence of a regime changes within this region should be noted. Like Roshko, Bloor [1963] observed irregularities in the $200<Re<400$ range as well, but suggested that in this range turbulence was introduced by three dimensional effects. Above $Re=400$, transition takes place before the separation layer curls up. The regularities in the signals taken downstream of the cylinder were found to only occur when transition occurred well within the separated region. Bloor determined that regularities in the

signal occurred for all Reynolds numbers above 1,300. The averaged Reynolds number was 4,641 in the lower plane region of the present study which put the flow regime past the cylinder above Bloor's criteria and near transition between the subcritical flow regime and the presence of Kelvin-Helmholtz instabilities in the shear layer [Fey *et al.* 1998]. As will be shown in the results of the present study, transition between high and lower fluctuation regimes appear to take place as the flow fluctuates in time.

1.1. Experimental Reference Setup

The experimental setup of Amini and Hassan [2009] that was numerically modeled in this study utilized the matched index of refraction (MIR) technique and dynamic particle image velocimetry (PIV) to obtain time resolved two dimensional velocity fields within a staggered rod bundle. The MIR technique relies on the principle that when the test fluid and the solid structures within the domain have a perfectly matched index of refraction, the solid structure no longer refracts the light. This results in no distortion of the light and a completely transparent experimental region for taking measurements. The technique of 2D particle image velocimetry (PIV) relies on a focused plane of high intensity pulsed laser light to illuminate micron sized seeding particles that faithfully follow the flow paths. A high speed camera captures the particles illuminated by the laser. A cross correlation PIV algorithm is applied to the sequence of images and by knowing the frame rate of the captured images and the length scale within the illuminated domain, nearly

instantaneous velocities may be obtained. The rod bundle has a 3:4:3 configuration of 29 rods with pitch to diameter ratios indicated in figure 3.

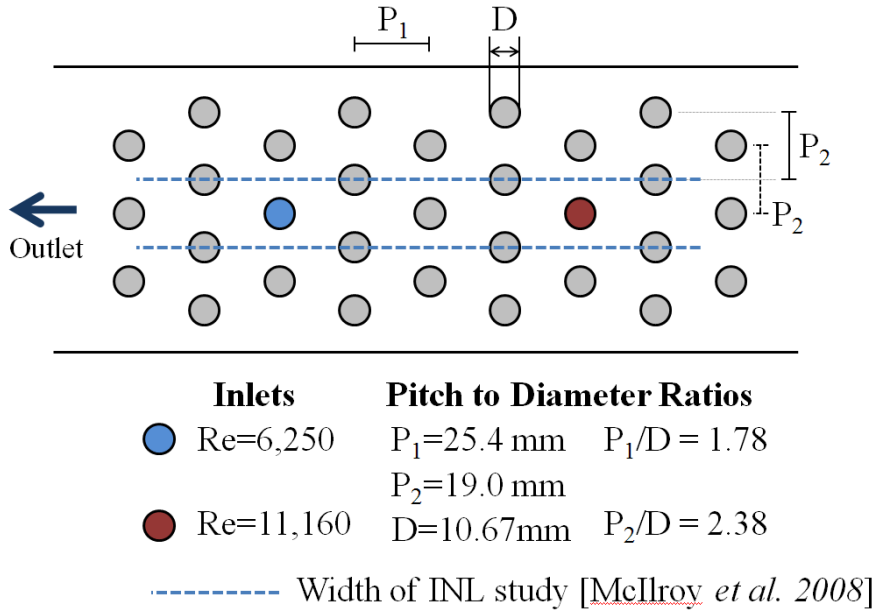

Figure 3. **Rod bundle configuration of Amini and Hassan [2009]**

The rod bundle, as seen in Figure 4, was situated between two flow straighteners present for other experimental investigations not addressed in this experimental study. The straighteners of the experiment were modeled in the computer sided design (CAD) model to mimic the same experimental geometry in the CFD simulations. The inlet tube lengths prior to the jet entrance exceeded 10 diameters. In the case of this work, the inlet tube lengths were modeled with 10 diameter lengths to allow sufficient length for flow development. The viewpoint from which experimental data was captured was the vertical mid-plane bisecting the two inlet jets.

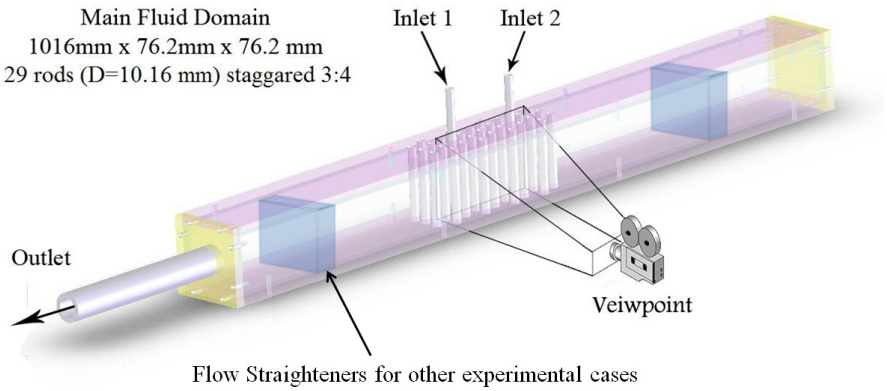

Figure 4. **Experimental setup including flow straighteners and camera viewpoint of data collection**

2. METHODOLOGY

In order to perform the desired CFD simulations, the fluid domain must first be discretized into small pieces over which the governing equations may be applied to obtain the results for a given numerical model. An important part of the discretization process is to ensure that numerical diffusion due to the size of the grid is kept to a minimum. In the following section, descriptions of the turbulence models are given followed by the grid sensitivity method and results.

2.1. Turbulence Model Specifications

The various turbulence models employed throughout the study are outlined in brief in this section. It is suggested that for more in-depth coverage of the presented models, the supplied references be looked into.

2.1.1. Standard k-ε Model

The most frequently seen of all the turbulence models in CFD simulations is the standard k-ε model. The form used has transport equations defined by the work of Jones and Launder (1972) and coefficients defined by Launder and Sharma (1974). The model is known to produce robust results even for less than ideal conditions. The main transport equations involved in the model are:

$$\frac{d}{dt}\int_V \rho k dV + \int_A \rho k\left(v - v_g\right)\cdot da = \int_A (\mu + \frac{\mu_t}{\sigma_k})\nabla k \cdot da + \int_V \left(G_k + G_b - \rho(\varepsilon + \gamma_M)\right)dV \quad (1)$$

$$\frac{d}{dt}\int_V \rho\varepsilon dV + \int_A \rho\varepsilon(v - v_g)\cdot da = \int_A (\mu + \frac{\mu_t}{\sigma_\varepsilon})\nabla\varepsilon \cdot d + \int_V \frac{1}{T}\left(C_{\varepsilon 1}(G_k + G_{n1} + C_{\varepsilon 3}G_b) - C_{\varepsilon 2}\rho\varepsilon + \rho\Upsilon_y\right)dV \quad (2)$$

$C_{\varepsilon 1}$	$C_{\varepsilon 2}$	σ_k	σ_ε
1.44	1.92	1.0	1.3

2.1.2. Realizable k-ε Model

The transport equations and the alterations to certain coefficients [Shih et al 1995] for the realizable k-ε turbulence model are as follows:

$$\frac{d}{dt}\int_V \rho k dV + \int_A \rho k(v - v_g)\cdot da = \int_A (\mu + \frac{\mu_t}{\sigma_k})\nabla k \cdot da + \int_V \left(G_k + G_b - \rho(\varepsilon + \gamma_M)\right)dV \quad (3)$$

$$\frac{d}{dt}\int_V \rho\varepsilon dV + \int_A \rho\varepsilon(v - v_g)\cdot da = \int_A (\mu + \frac{\mu_t}{\sigma_\varepsilon})\nabla\varepsilon \cdot d + \int_V \left(C_{\varepsilon 1}S\varepsilon + \frac{\varepsilon}{k}(C_{\varepsilon 1}C_{\varepsilon 2}G_b - C_{\varepsilon 2}\rho\varepsilon\right)dV \quad (4)$$

The main difference between the standard k-ε model and the realizable model is that the term for turbulent viscosity (*equation 5*) has a coefficient C_μ in it that is not defined as a constant any more but instead by *equation 6-7* which are functions

of mean strain rate, angular velocity of the rotating system, and the turbulence fields k and ε.

$$\mu_t = \rho C_\mu \frac{k^2}{\varepsilon} \tag{5}$$

$$C_\mu = \frac{1}{A_0 + A_s U^{(+)} \frac{k}{\varepsilon}} \tag{6}$$

Where

$$U^{(+)} = (S{:}S - W{:}W)^{\frac{1}{2}} \tag{7}$$

The other change from a constant to a formula is the $C_{\varepsilon 1}$ coefficient (equation 8). These changes result in a more robust dissipation rate equation over the standard model.

$$C_{\varepsilon 1} = \max\left(0.43, \frac{\eta}{5+\eta}\right) \tag{8}$$

Where

$$\eta = \frac{Sk}{\varepsilon} \tag{9}$$

Other coefficients present in the model's formulation are given by the following equations and specified constants.

$$A_s = 6^{\frac{1}{2}} \cos\phi \tag{10}$$

$$\phi = \operatorname{acos} 6^{\frac{1}{2}} W \tag{11}$$

$$W = \frac{S_{ij} S_{jk} S_{ki}}{\left(2^{\frac{1}{2}} \hat{S}\right)} \tag{12}$$

A_0	$C_{\varepsilon 2}$	σ_k	σ_ε
4.0	1.9	1.0	1.2

2.1.3. Large Eddy Simulation (LES) with WALE Subgrid Model

The large eddy simulation (LES) model resolves large scales using the Navier-Stokes equations directly just as in unsteady RANS simulations, and uses a subgrid scale(SGS) model for the turbulent stress tensor. The SGS model resolves the effects of scales smaller than the grid size and their effect on the larger scales. An implicit scheme for time stepping was used instead of an explicit scheme. The ramifications of this is a relaxation of the acceptable Courant Friedrich Levi (CFL) condition to obtain satisfactory results that resolve the dominant structures (less than 5); however, the most refined scales with lower energies might not be fully resolved. The advantage to this method is a drastic reduction in the computational time necessary to run the simulation until fully developed periodic steady state conditions have been reached in the flow. This is due to the ability to choose a time step nearly 10 times larger than that for the standard LES approach.

The selection of time step for the LES simulation was chosen from the CFL condition (equation 13) for the given length scales. The maximum velocity (~1.3m/s) in the flow domain occurs at the high Reynolds number jet entrance into the domain. The cell size for the LES simulation is approximately 0.65mm as discussed in the following section. Applying the CFL condition of 1, the time step chosen is 0.0005s.

$$CFL = \frac{u \cdot \Delta t}{\Delta x} \tag{13}$$

Upon running the simulation, the maximum CFL number in the entire flow domain was a value of 2.08 and values in the range over 1 were only present in the

core of the jet and not in the viscous superlayer where the jet entrains the quiescent domain. The Courant limit below a value of 5 is satisfied in the very large eddy simulation. Very small scale eddies in the viscous superlayer may be expected not to be resolved fully, but the large scale frequencies should present themselves clearly.

The turbulent stress tensor, T_{ij}, is represented below as a function of SGS turbulent viscosity μ_t, kinetic energy k, and the strain rate tensor $\overline{S_{ij}}$.

$$T_{ij} = 2\mu_t \overline{S_{ij}} - \frac{2}{3}(\mu_t \nabla \cdot \boldsymbol{v} + \rho k) \tag{14}$$

Where $\overline{S_{ij}}$ is computed by:

$$\overline{S_{ij}} = \frac{1}{2}(\nabla \boldsymbol{v} + \nabla \boldsymbol{v}^T) \tag{15}$$

The subgrid model used was the wall adapting local eddy-viscosity (WALE) subgrid scale model. The WALE SGS model [Nicoud and Ducros 1999] for turbulent viscosity μ_t is defined by the length scale Δ, density ρ, the strain rate tensor $\overline{S_{ij}}$, the deformation tensor S_{ij}^d, and a constant C_w.

$$\mu_t = \rho \nu \tag{16}$$

$$\nu = (\mathrm{C_w}\Delta)^2 \frac{(S_{ij}^d S_{ij}^d)^{3/2}}{(\overline{S_{ij}}\,\overline{S_{ij}})^{5/2} + (S_{ij}^d S_{ij}^d)^{5/4}} \tag{17}$$

Where the coefficient $C_w = 0.544$ which is near the value $C_w \approx 0.5$ suggested by Nicoud and Ducros [1999] for the best results using the model. The deformation tensor S_{ij}^d is defined by

$$S_{ij}^d = [\nabla \boldsymbol{v} \cdot \nabla \boldsymbol{v} + (\nabla \boldsymbol{v} \cdot \nabla \boldsymbol{v})^T] \tag{18}$$

The length scale Δ is defined as the minimum value between $\mathrm{C_w V^{1/3}}$ and κd where V is cell volume, κ is the von Karman constant, and d is the distance to the nearest wall. The resulting model properly scales near wall eddy viscosity. It has

been demonstrated that the WALE SGS model can better handle laminar to turbulent transitional regimes [Nicoud and Ducros 1999] than the traditional Smagorinsky eddy viscosity model; however, it should be noted that a similar coefficient to that present in the Smagorinsky SGS model is used which has local influence on the flow.

2.2. Discretization

The majority of numerical works published in the infancy of CFD, while showing advancements in the field, were severely hindered by a lack of structured methodology for limiting the extent of error due to numerical diffusion [Roache 1998]; a problem involving discretization error that has since been extensively studied and proper practices have been developed.

Beginning as an editorial policy statement in 1986 in the ASME Journal of Fluids Engineering [Roache et al 1986], sensitivity analysis has since grown into a science of its own. Many revisions and additions have been made to such policies over the years in peer review journals from a wide range of fields in which CFD techniques are either developed further or simply drawn upon as a tool to aid in a study. The process of ensuring the fidelity of a simulation has become as integral a step in CFD as the presentation of the results themselves. The most recent policy statement in the Journal of Fluids Engineering [Celik et al. 2008] emphasizes techniques employing the Richardson's Extrapolation (RE) method and grid convergence indices (GCI). The technique of Richardson's Extrapolation as a method of extrapolating a solution out to its limit has been around long before the

advent of CFD; however, the use of RE as a tool in grid convergence studies is extremely useful, so long as the proper measures are taken to ensure an extrapolated result is obtained that is true to the models and methods being applied.

The objective of any simulation is to obtain high fidelity results; however, many times the results become products of the numerical diffusion artifacts as opposed to the flow physics. A necessary measure to limit such diffusion is to perform a mesh sensitivity study to determine the grid size below which numerical artifacts don't present themselves in the result. Difficulties arise in such efforts due to the advent of the unstructured mesh. In this work, unstructured polyhedral cells were used in the discretization process. In an effort to make the meshes more comparable to one another and limit error sources, a volume modifier was employed in the meshing process that forced the polyhedral cells into a semi-structured pattern within the volume. This process helped homogenize the mesh throughout the domain of interest with the exception of very close to wall features that the mesh must adapt around. The prism layer for all of the meshes was maintained the same as to avoid introducing affects from sources other than the core polyhedral mesh.

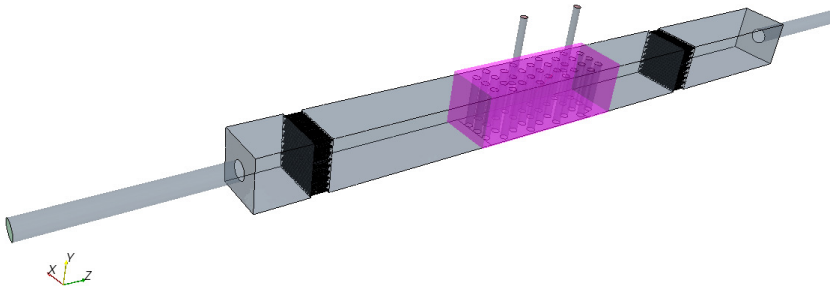

Figure 5. **Numerical domain with volume modifier (pink) for mesh ordering into semi-structured pattern**

The cell sizes within the bundle region of interest had cell sizes of 0.65mm, 0.75mm, 0.9mm, 1.2mm, 2mm, and 3mm. The number of cells for each grid is given in table 1. Figure 6 illustrates the mesh densities with different cell sizes taken along the mid-plane of the channel bisecting both inlet jets. It may be seen that at the coarsest grid sizes, out of plane rods tend to disrupt the semi-structured grid alignment. As the grids are refined, the cell structures in the core regions away from the walls and rods are homogenous. Cell sizes within the rod bundle in the horizontal plane are shown in figure 7. The corresponding cells to rod diameter ratios are indicated in table 2.

Table 1. **Base cell sizes and total number of cells for each grid used in the sensitivity study**

Grid Number	Cell Size (h) in mm	Number of Cells (N)
0	0.65mm	13,207,130
1	0.75mm	10,176,501
2	0.90mm	7,662,692
3	1.20mm	5,603,819
4	2.00mm	4,439,612
5	3.00mm	4,237,281

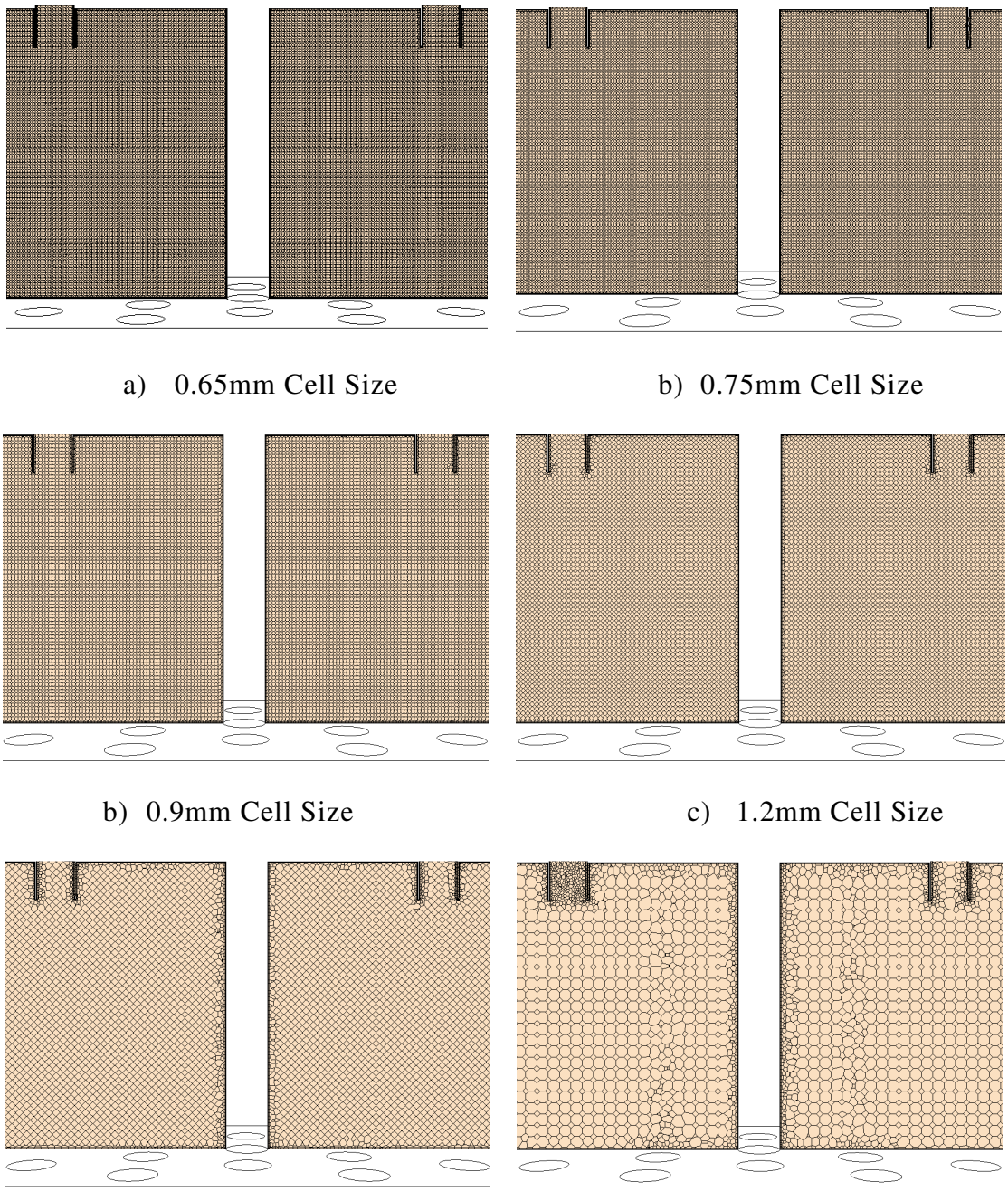

a) 0.65mm Cell Size

b) 0.75mm Cell Size

b) 0.9mm Cell Size

c) 1.2mm Cell Size

d) 2mm Cell Size

e) 3mm Cell Size

Figure 6. **Vertical mid-plane sections of semi-structured polyhedral meshes for sensitivity study**

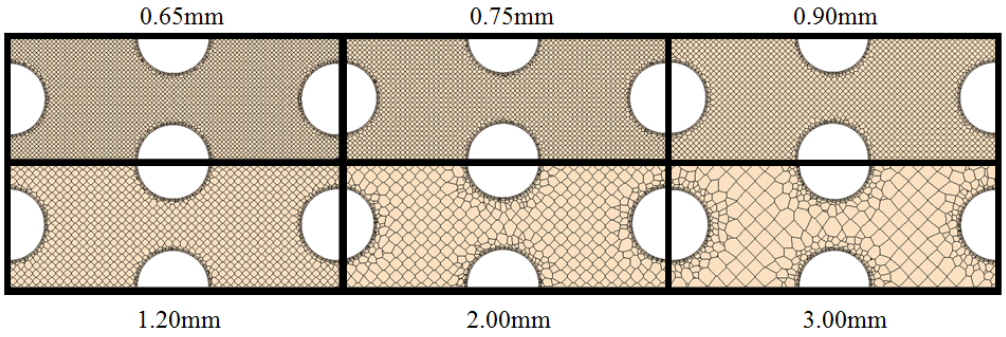

Figure 7. **Horizontal plane sections of semi-structured polyhedral meshes for sensitivity study**

Table 2. **Cell to rod diameter ratio table of sensitivity study grids**

Grid Number	Cell Size (h) in mm	Cell to rod diameter ratio (d_c/D)
0	0.65mm	0.061
1	0.75mm	0.070
2	0.90mm	0.084
3	1.20mm	0.112
4	2.00mm	0.187
5	3.00mm	0.281

Discretization error was quantified using the procedures outlined in the quality control statement of Celik et al. [2008] as well as Roache [1998] which identify accepted techniques by which the Richardson extrapolation(RE) method may be applied reliably. Local and global orders of accuracy, extrapolated results, percent errors, and grid convergence indexes were all calculated in accordance with these accepted practices in an effort to ensure that high fidelity results had indeed been obtained.

In total, the six meshes listed in Tables 1 and 2 were investigated using the realizable k-ε turbulence model with an all-y+ wall function applied to a two cell

prism layer that remained constant between the different grids. The steps by which RE was performed are as follows [Celik et al. 2008]:

Step 1

For grid sizes $h_1<h_2<h_3$, where $r_{21}=h_2/h_1$ and $r_{32}=h_3/h_2$ are near or greater than 1.3, the local apparent order of accuracy, p, of the simulation is calculated with the following expressions:

$$p = \frac{1}{\ln r_{21}} \left| \ln \left| \frac{\varepsilon_{32}}{\varepsilon_{21}} \right| + q(p) \right| \tag{19a}$$

$$q(p) = \ln \frac{(r_{21}^{p} - s)}{(r_{32}^{p} - s)} \tag{19b}$$

$$s = \text{sign}\left(\frac{\varepsilon_{32}}{\varepsilon_{21}}\right) \tag{19c}$$

Where

$$\varepsilon_{21} = \varphi_2 - \varphi_1 \tag{20a}$$

$$\varepsilon_{32} = \varphi_3 - \varphi_2 \tag{20b}$$

Equations (19a-c) were solved using an iterative procedure with an initial guess of φ_1 where φ_n represents the result of the associated grid n. The global order of accuracy is obtained by taking the mean of the local orders to obtain p_{ave}.

Step 2

The extrapolated values φ_{ext}^{21} and φ_{ext}^{32} were calculated using the following equations:

$$\varphi_{ext}^{21} = \frac{(r_{21}^{p}\varphi_1 - \varphi_2)}{(r_{21}^{p} - 1)} \tag{21a}$$

$$\varphi_{ext}^{32} = \frac{(r_{32}^{p}\varphi_2 - \varphi_3)}{(r_{32}^{p} - 1)} \tag{21b}$$

Step 3

The relative errors, e_a^{21} and e_{ext}^{21}, were calculated by the expressions below:

$$e_a^{21} = \left|\frac{\varphi_1 - \varphi_2}{\varphi_1}\right| \tag{22a}$$

$$e_{ext}^{21} = \left|\frac{\varphi_{ext}^{21} - \varphi_1}{\varphi_{ext}^{21}}\right| \tag{22b}$$

Step 4

Calculate the grid convergence index for the most refined mesh with:

$$GCI_{fine}^{21} = F_s \frac{e_a^{21}}{r_{21}^{p_{ave}} - 1} \tag{23}$$

In eqn 5, the F_s coefficient serves as a 'buffer coefficient' for the extrapolated error approximation GCI. In the case of rough grids, a conservative value of 3 may be applied to this factor, and a value of 1.25 in the more refined grid cases [Roache 1998], as in the case of this study. The idea behind this coefficient reducing to a value of 1 for a more refined grid is that as grid cell size gets smaller, the error due to numerical diffusion reduces to the point that any error present between the extrapolated solution and the calculated solution is the absolute error and is no longer an artifact of grid dependency, thus GCI = e in such a case.

The first investigated parameter in the sensitivity study was the velocity magnitude in the axial direction to the inlet jets at both nozzle locations (x=775mm and x=673.4) within the channel. For all grids, line probes sampled 30 points from

the bottom of the channel to points within the inlet jet (y=0mm to y=78.2mm) as shown in figure 8. Grid convergence indices were calculated based on three grids at a time. Grid combinations following the recommendation of having grid size ratios larger than 1.3 [Celik et al. 2008] were used; however, combinations were also used that intentionally violated this practice to investigate the scale of the error in the Richardson extrapolation. This grid sensitivity study was performed using two different Dirichlet boundary conditions, thus giving two separate sets of results using identical grids. Ensuring grid dependence for both cases further insures that the fidelity of the end result has not been compromised due to numerical diffusion. Discrepancies between validation data and numerical results will instead be a direct result of the numerical model or models used.

2.3. Grid Sensitivity Study Results and Discussion

The results presented in this section are those for the sensitivity study performed for the case of Re_{jet1}=11,160 and Re_{jet2}=6,250. In appendix A, results of a sensitivity study are given for the case of Re_{jet1}=13,400 and Re_{jet2}=6,700 to demonstrate that the simulation was grid size independent for multiple boundary conditions.

Figure 8 shows the location of the line probes used to obtain results from each mesh. Given that each mesh has a varying number of cells along this line, a controlled line probe was used with 30 points taken at identical heights for each grid size. In the cases of the very coarse mesh sizes, a certain degree of interpolation

occurs in the result. The error introduced by this interpolation becomes minute as the mesh is refined. Results from the different grids are shown in figure 9.

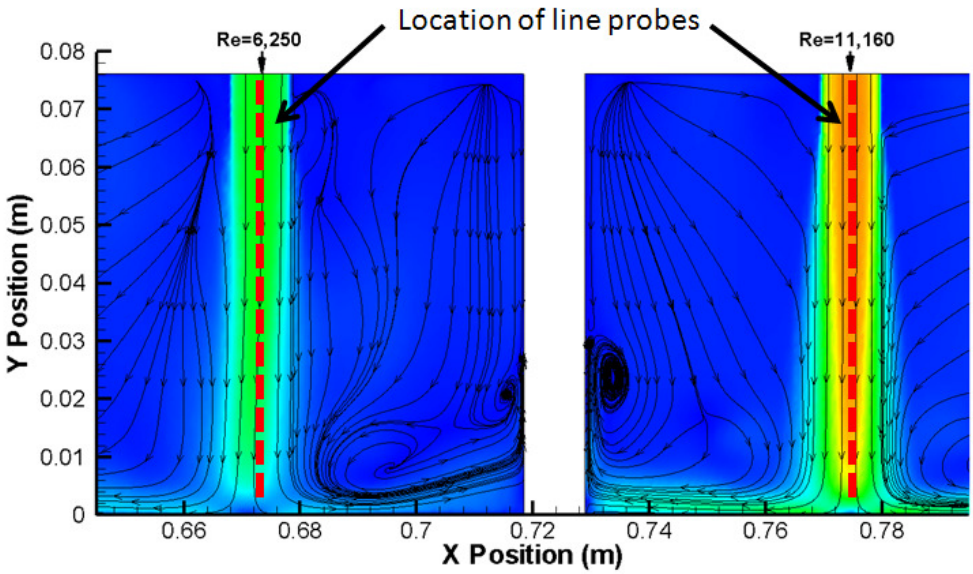

Figure 8. **Axial line probe locations for sensitivity study**

The calculated grid convergence indices (GCI) are presented in figure 10 for both high and low Re jets. Grid convergence indices are presented as a percent and can effectively be interpreted as the percent error of the simulation result based on which grids are analyzed. In the case of GCI – 3;2;0, the reported error would apply to grid 0.

A point of interest in the plot of velocity magnitude versus y-position for the low Reynolds number jet (figure 9) is the crossing of the results of the 0.65mm mesh and the 0.90mm mesh at y=24mm. A cross in the result can be indicative of locally oscillating convergence of the result. This form of convergence may be considered valid as these grid sizes are shown to be in the asymptotic range of convergence in

the neighboring locations. The crossing feature represents itself in the GCI as well as the error between the extrapolated and the calculated results. At the point of the cross, the extrapolated solution is equivalent to the same value. This causes the GCI and the error between the extrapolated and the calculated results of the 0.90mm and 0.65mm grid to drop to zero. This is the cause of the dip seen in the GCI of Re_{jet2} in figure 10.

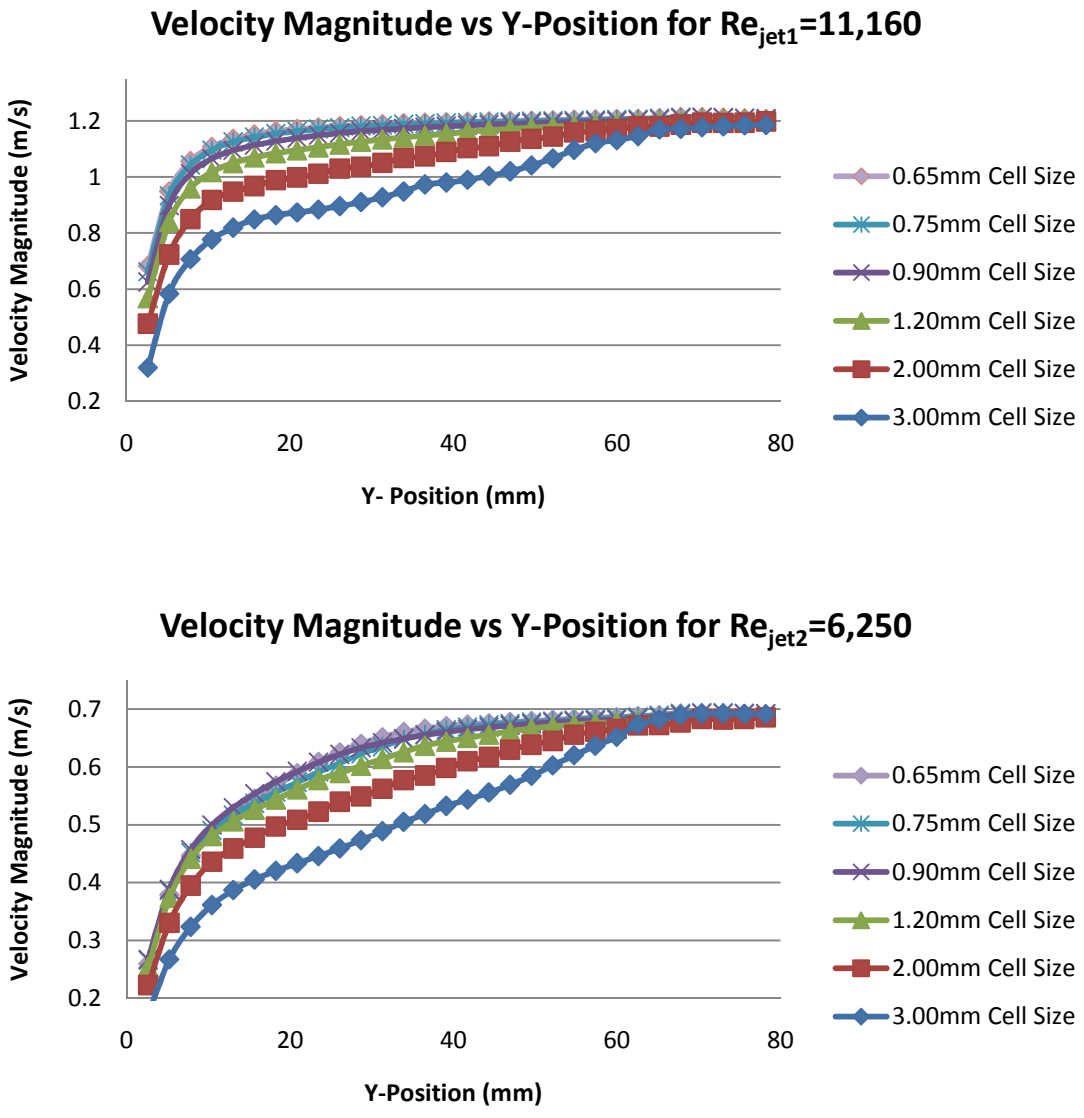

Figure 9. **Axial flow velocity directly below inlet jets Re_{jet1}=11,160 and Re_{jet2}=6,250**

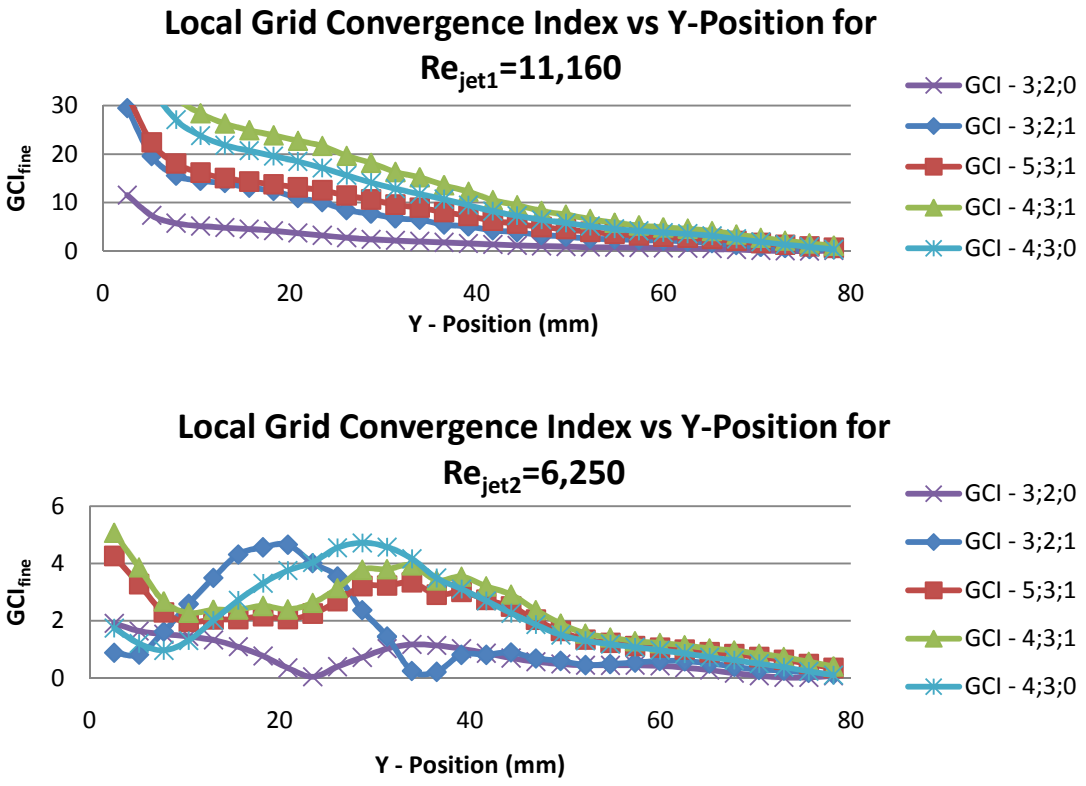

Figure 10. **Grid convergence indices directly below inlet jets Re$_{jet1}$=11,160 and Re$_{jet2}$=6,250**

The extrapolated results presented in figures 11 are zooms of the region near the lower plane between y=0mm and y=50mm. These results illustrate the importance of using three grids that all lie within the asymptotic zone as well as satisfy the grid size ratio of $r_{ik} \gtrsim 1.3$. Extrapolated results obtained using grids not in the asymptotic zone or not following the suggested cell size criteria exhibit a divergence in the extrapolated result leading to unrealistic results. This is shown most prominently in figure 11 by the acceleration towards y=0mm obtained from the extrapolated result of grids 4, 3, and 1.

The extrapolated result that consistently had physically realistic results, had the lowest GCI values, and satisfied the refinement criteria was the extrapolation calculated using grids 3, 2, and 0. This was expected based on the criteria previously mentioned. The results from the extrapolation using these grids were used in the calculation of the relative errors shown in figure 12. This figure clearly shows the decrease in approximation error as the refined grids approach asymptotic convergence on the ideal result that is totally free from numerical diffusion. The global order of accuracy for the two jets were p_{ave}=1.99 in the high Re jet and p_{ave}=3.23 for the low Re jet.

In addition to line probes, the mean vortex diameters of the two primary recirculation zones present adjacent to the central rod were used as sensitivity study parameters with the 0.65mm, 0.90mm, and 1.20mm grid sizes. The recirculation zone metrics are shown in figure 13 and the mean diameter, D_v, is defined as the sum of a_1 and b_1.

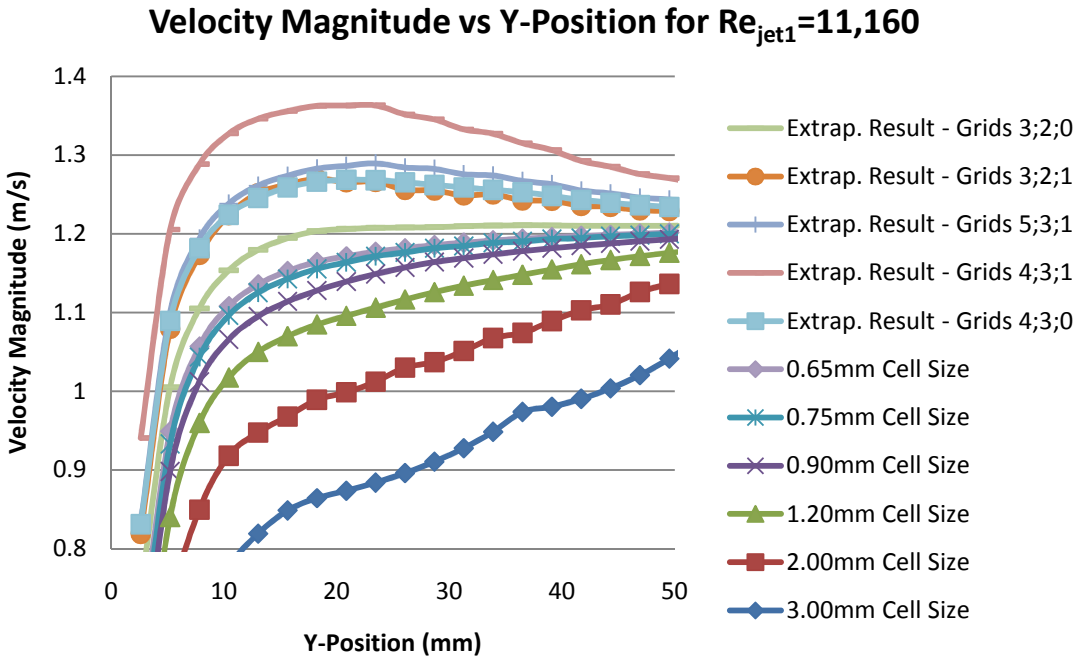

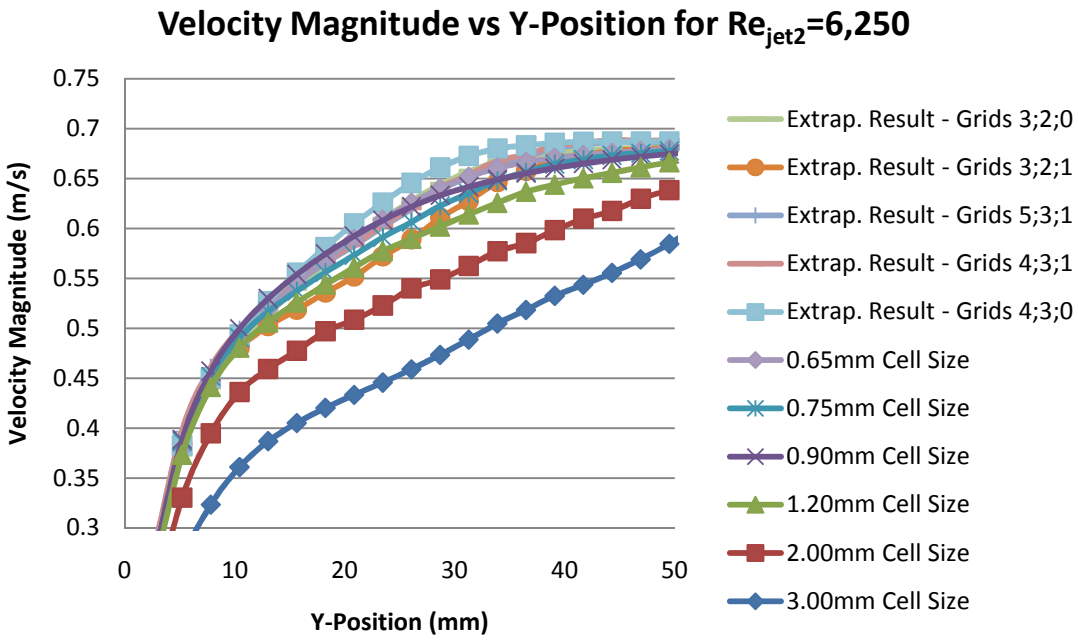

Figure 11. **Extrapolated results directly below inlet jets Re$_{jet1}$=11,160 and Re$_{jet2}$=6,250**

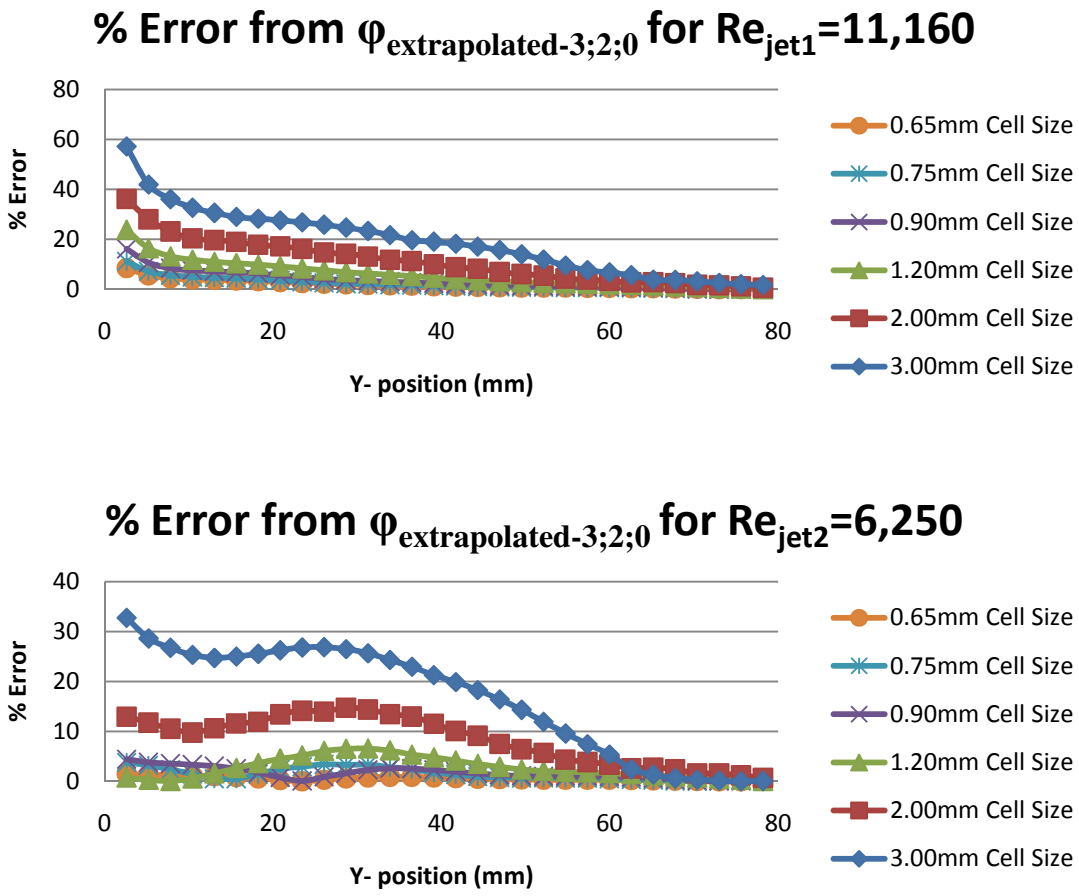

Figure 12. **Error from each grid size to the result extrapolated from grids 3, 2, and 0 for Re_{jet1}=11,160 and Re_{jet2}=6,250**

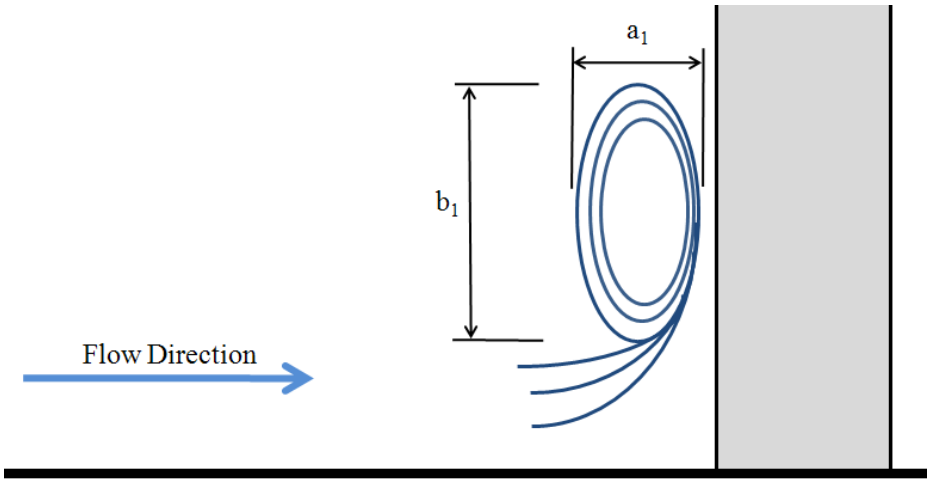

Figure 13. **Mean vortex diameter metrics**

The result of the sensitivity study indicate a 7.3% error(±1.15mm) in the mean diameter of the vortex on the side of the high Reynolds number jet, and 13.6% error(±1.47mm) in the mean diameter on the side of the low Reynolds number jet. This error underlies the difficulty in determining grid size independence in highly three dimensional flows. It should also be noted that the large error present in this parameter is also influenced by the feature size relative to the grid size. The orders of convergence for the primary vorticies on the high and low Reynolds number sides of the central rod are still 2.89 and 3.65 respectively. Unfortunately, in flows with very convoluted structures, large measurable features can be limited which often influences the relative magnitude of errors when dealing with smaller structures. In terms of cell size, an error of 13.6% in the present grid for the low Re jet vortex equates to about 2.5 cell diameters. At the time of this study, the particular grid was at the upper bounds of the computational capabilities available, but the result still provides acceptably resolved flow structure in staggered rod bundles.

The case of Re_{jet1}=11,160 and Re_{jet2}=6,250 has corresponding experimental data obtained in a geometrically identical facility using dynamic PIV [Amini and Hassan 2009]. For this reason, only this case was run using additional turbulence models, and only with the most refined grid. The following section contains the results and analysis of key features and phenomena present in the domain.

2.4. Analysis Methods

Advanced frequency analysis methods have been developed and employed extensively in recent years for the purpose of visualizing a decomposed frequency. The wavelet transform enables instantaneous visualization of the frequencies present and their intensities throughout the length of the signal on a single contour plot. The idea behind wavelets takes root back to Joseph Fourier and his developed method now referred to as the Fourier transform [Fourier 1822] whereby sine and cosine waves are be superimposed to represent another function entirely.

Nearly a century later, Alfréd Haar completed his dissertation at the University of Gottingen in which he established the Haar basis function [Haar 1909]. The function is a simple scalable square step function that which may be used in much the same manner as the sine and cosine functions in the Fourier transform. Work by Paul Levy on the randomness of Brownian motion in the 1930s found that through the use of the Haar function as opposed to the traditional trigonometric functions of the Fourier transform, he could resolve much finer details of the motion.

In 1985 a major advance in the basis functions employed was made through the creation of a continuously differentiable family of functions now known as Meyer wavelet. Meyer's work came in response to new advances in digital signal filtering and processing algorithms developed by Stephane Mallat [Mallat 1989]. Since then, other wavelets functions have been developed, each allowing for the identification of specific signal features. The use of the second derivative Gaussian wavelet, more commonly referred to as the Mexican hat wavelet, results in a decomposition that identifies maximums and minimums in the signal with good time localization.

Similar continuous wavelet basis functions such as the Morlet wavelet [Goupillaud *et al.* 1984] were developed by other researchers simultaneously in other fields. The Morlet wavelet offers its own sets of advantages and disadvantages such as the ability to better resolve details in the frequency domain. The wavelet transform method of signal decomposition is a proven method that offers a very powerful tool for signal analysis. In the case of the present study, convoluted signals are decomposed for analysis through this method as well as with some other complimentary methods such as the Fast Fourier Transform (FFT).

The wavelet transform is a method by which a single defined wavelet basis function $\psi(\mathrm{t})$ is expanded in its range and domain as well as translated such that an entire series of functions or 'atoms' is formed to characterize the signal $s(t)$. The atoms are defined by the function $\psi_{a,b}(\mathrm{t})$ [Misiti *et al* 2007]:

$$\psi_{a,b}(\mathrm{t}) = \frac{1}{\sqrt{a}}\psi\left(\frac{t-b}{a}\right) \tag{24}$$

Where the coefficient b translates the wavelet basis function $\psi(\mathrm{t})$, and a adjusts the scale. The continuous wavelet transform of signal $s(t)$ is defined by the function C_f.

$$C_f(a,b) = \int_{\mathbb{R}} s(t)\overline{\psi_{a,b}(\mathrm{t})}\,dt \tag{25}$$

The coefficients $C_f(a,b)$ give an indication of the correlation between the adjusted wavelet function and the signal for given values of a and b over the entire

time domain. By plotting the coefficients over the entire domain with respect to time and scale, with contour intensity indicating coefficient values, a logical depiction of the decomposed signal over the entire time domain may be viewed in a single plot.

Graphically, this may be shown more readily with the following example.

Example Wavelet Decomposition:

Start with signal $s(t)$ that is to be decomposed, in this case the simple cosine signal in figure 14:

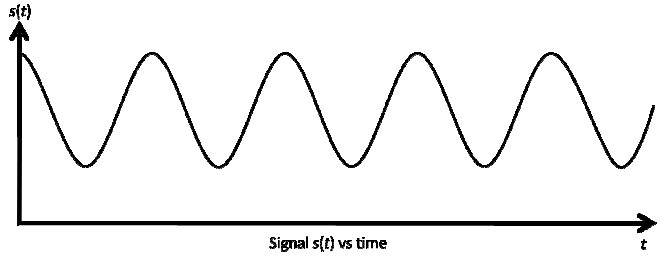

Figure 14. **Sample signal $s(t)$ versus time t**

A desired wavelet is chosen (the reasoning behind the choice of this wavelet is for ease of visual explination). In this case the second derivative of the Gaussian wavelet (aka. the Mexican hat wavelet) shown in figure 15 will be used.

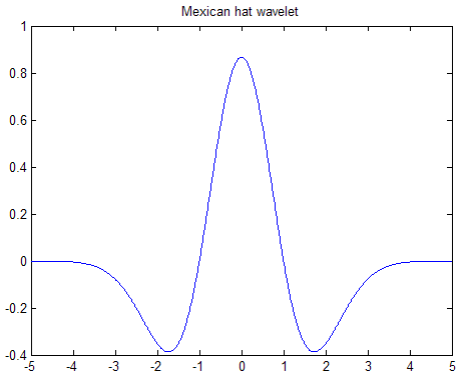

Figure 15. **Mexican Hat wavelet basis function for continuous wavelet transform**

The Mexican hat basis function is defined as:

$$\psi(t) = \frac{2}{\sqrt{3}}\pi^{-\frac{1}{4}}(1-t^2)e^{-\frac{t^2}{2}} \tag{26}$$

The continuous wavelet transform calculates the coefficient that indicates the degree of matching for different wavelet atoms. For a single well-scaled atom, this appears graphically as shown in figure 16.

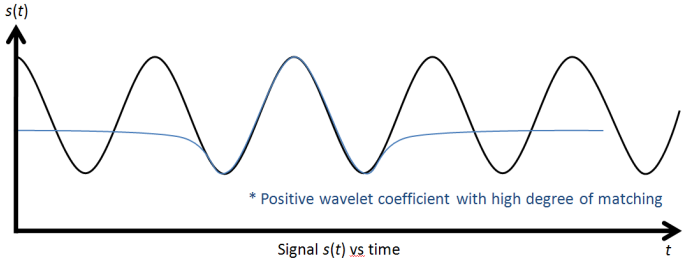

Figure 16. **Signal $s(t)$ with single wavelet atom with high level of matching**

The plot of coefficients takes the form of scale (often period or frequency) vs. time, with color intensity as the contour. The plot for this single atom is a single point with a given intensity indicated in figure 17.

Figure 17. **Coefficient plot for single wavelet atom**

When a multiple series of atoms are taken at the same translation in time, the coefficient plot becomes populated as shown in figure 18.

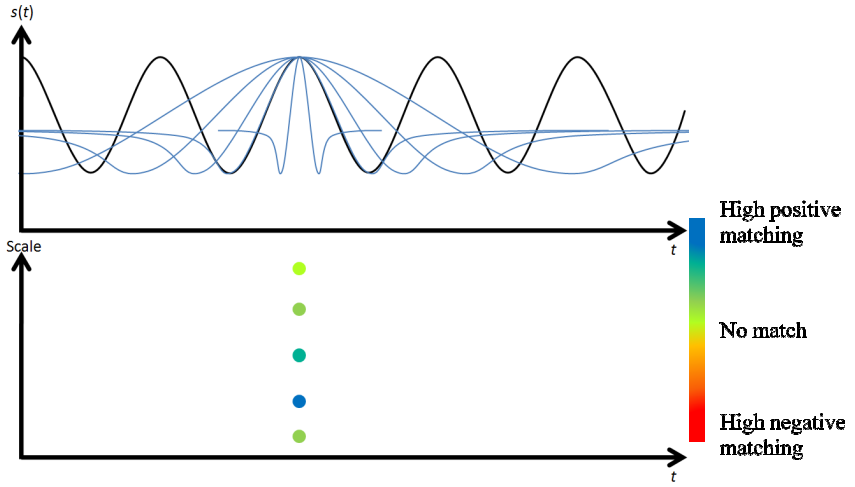

Figure 18. **Multiple atoms with varying degrees of matching**

By extrapolating this population to a continuous series of atoms, translating them over the entire domain, and allowing atoms to take the negative form, key frequencies become identifiable within the coefficient plot presented in figure 19.

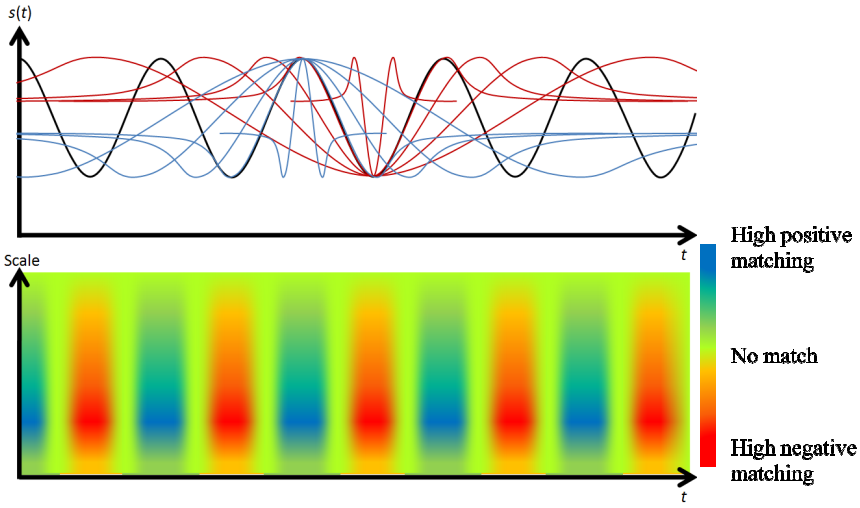

Figure 19. **Continuous wavelet transform over entire time domain**

In the case of multiple frequencies superimposed upon one another, the advantages of the wavelet transform become apparent. As seen, the Mexican hat wavelet does a good job identifying local maximums and minimums within the signal. The application in the current study utilizes a color contour that is based on the absolute value of the contribution rather than separately identifying positive and negative contributions. An example of this is shown in the next example. Other wavelet basis functions offer other advantages such as the ability to better identify fine gradients in the signal.

Take the case of a signal made up of two sine waves with intensities of 0.3 and 1.0 and frequencies of 10 Hz and 50 Hz respectively.

$$s(t) = 0.3\sin(2\pi 10t)+\sin(2\pi 50t) \tag{27}$$

Applying the wavelet transform and setting the scale in terms of frequency, the coefficient plot is obtained and both characteristic frequencies are visualized independently over the time domain in figure 20. It should be noted that the frequency domain is inversely related to the period; therefore, a lower period denotes a higher frequency. As the period approaches zero, the frequency approaches infinity; hence the large jump in frequency near the origin.

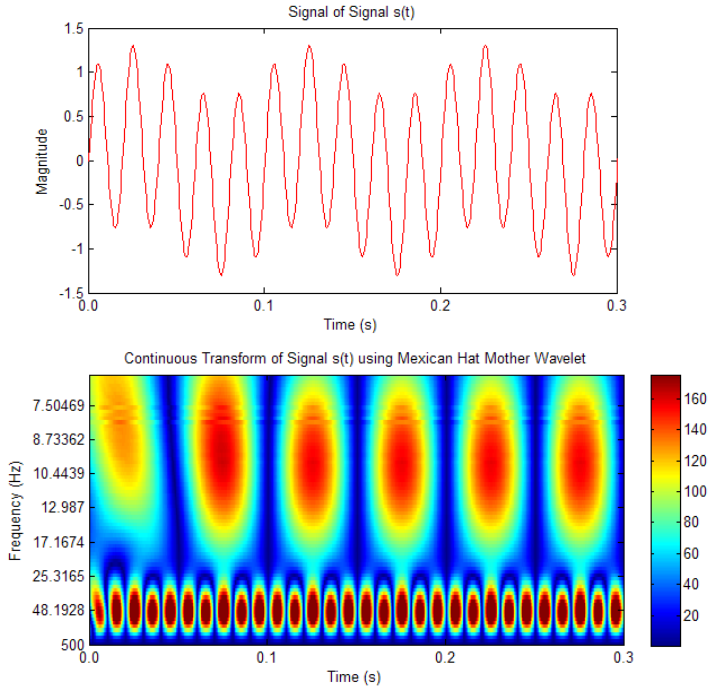

Figure 20. **Continuous wavelet transform of superimposed signal *s(t)* using the Mexican Hat wavelet**

Two different identified signals are present in the wavelet coefficient plot at the frequencies 10 Hz and 50 Hz. The 'legs' seen between the lower and higher frequency signals indicate that they are in phase with one another. The distortion near t=0 takes place due to the filtering algorithm being performed over a finite

domain. There is no distortion at t=0.3 due to the length of the signal extending beyond that which is plotted. In practice, the coefficients at the beginning and end of the plot are ignored to avoid the effects error introduced by this mechanism. Many times signals are doubled or tripled before the wavelet transform is done such that there is sufficient data to accurately decompose the signal. Sufficient results were obtained in this study to avoid the use of this technique.

The use of the Morlet wavelet, shown in figure 21, on the same signal will produce a different coefficient plot due to the high gradients of the basis function. This makes the wavelet ideal for identifying gradients in the signal with high accuracy in the frequency domain.

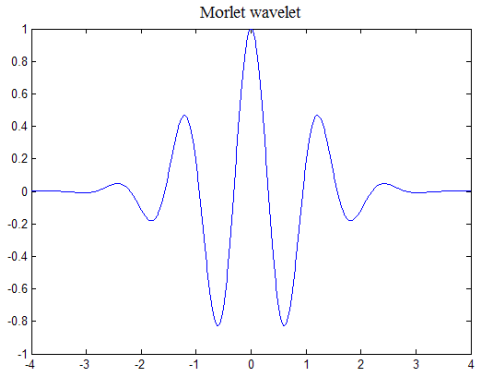

Figure 21. **Morlet wavelet basis function**

The Morlet basis function is defined by the following equation [Goupillaud *et al.* 1984]:

$$\psi(t) = e^{-\frac{t^2}{2}} \cos(5t) \tag{28}$$

The plot of coefficients, in figure 22, obtained from the wavelet transform using the Morlet basis function shows a tightened frequency resolution. As the focus of this study was around the study of turbulent structures and frequencies present within the rod bundle, the Morlet basis function was used in the analysis of the signals.

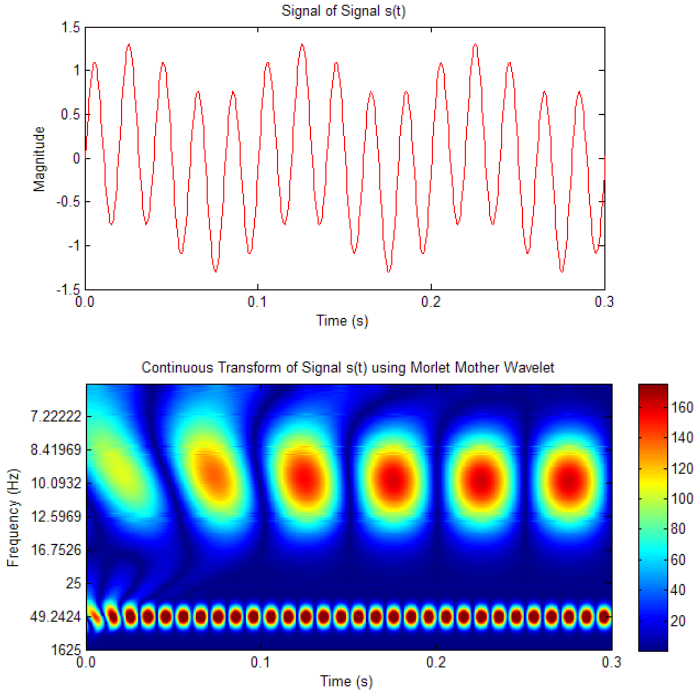

Figure 22. **Continuous wavelet transform of superimposed signal *s(t)* using the Morlet wavelet**

Another well established spectral decomposition method is the Fast Fourier Transform (FFT). While the use of FFT in identifying frequencies present in a given signal is extremely useful, it lacks the ability to decompose the signal for every sampled point in time. Figure 23 presents the FFT spectrum for the signal $s(t)$ with the two present frequencies clearly identified by the peak locations as well as the intensity indicated by the magnitude of the peak.

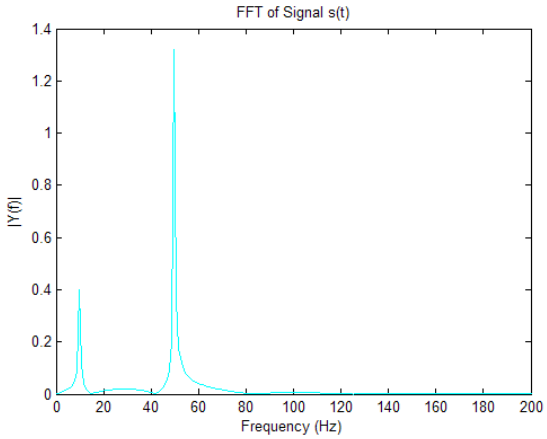

Figure 23. **Fast Fourier Transform of signal s(t)**

The use of various frequency analysis methods to complement one another improves on the comprehensiveness of the study. While the wavelet transform provides an instantaneous depiction of the signal, FFT is useful for decomposing the signal over the entire domain as well as providing a secondary decomposition for analysis.

3. RESULTS

3.1. Jet Spreading Rate and the Viscous Superlayer

Steady state results, while not entirely representative of a flow dominated by unsteady flow phenomena, are still useful in identifying regions of interest to be investigated in unsteady results, as well as providing good points of comparison with time averaged experimental data. The experimental data of Amini and Hassan [2009] is presented as a time averaged velocity field obtained using dynamic 2D PIV. Comparison between simulation results using various numerical models was performed using line probes taken in the axial direction within each jet, and then plotted on the same axis for each jet. In addition to steady state models, time averaging of the LES results was also performed over roughly 1400 time steps for a total simulation time of 0.7 seconds.

Jet dispersion is one parameter for comparison amongst the different models. An arbitrarily threshold value for the jet 'edge' was set to be 15% of the peak jet velocity obtained by the probe nearest to the inlet. This threshold value was kept constant for the remaining probes and was chosen because it gave the best compromise between spreading and velocity field variation on the fringe of the jet. Figures 24-26 show jet widths at varying heights between the inlet and 1.1cm from the bottom plane of the channel.

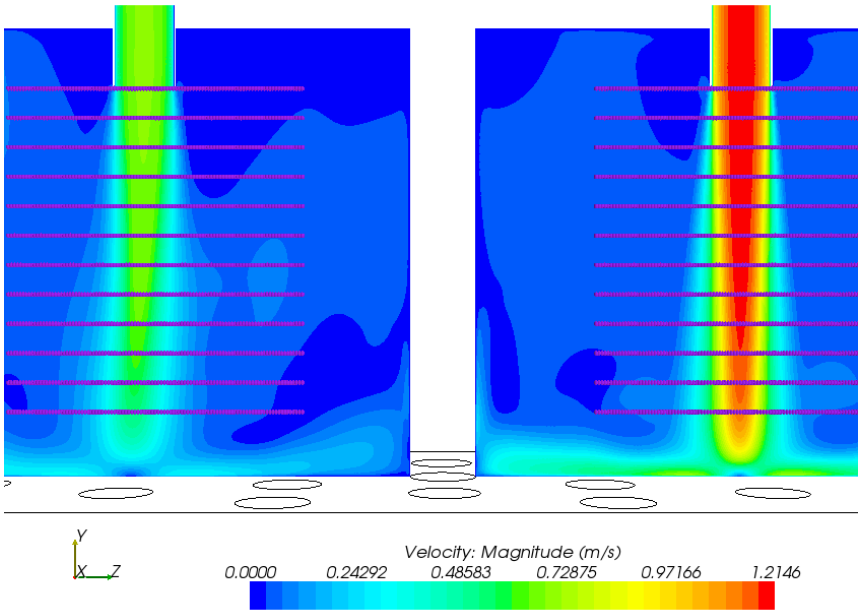

Figure 24. **Line probe locations under each jet at increments of 5mm shown on the scalar result plot obtained using the realizable k-ε model.**

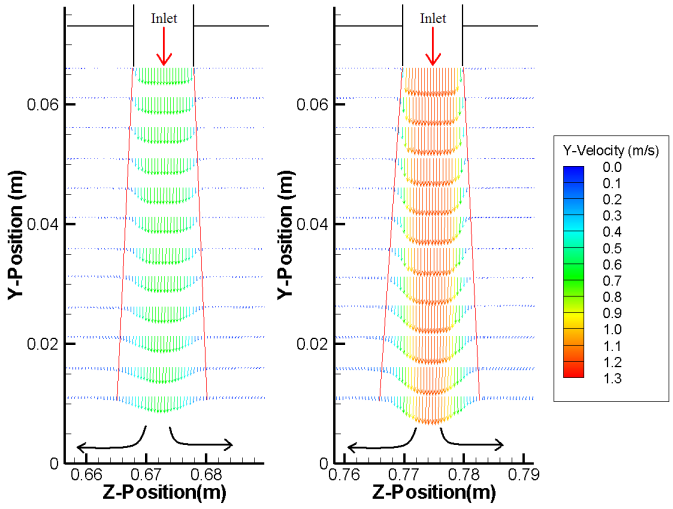

Figure 25. **Velocity profiles along line probes of the averaged LES results for the two jets Re=6,250(left) and Re=11,160(right).**

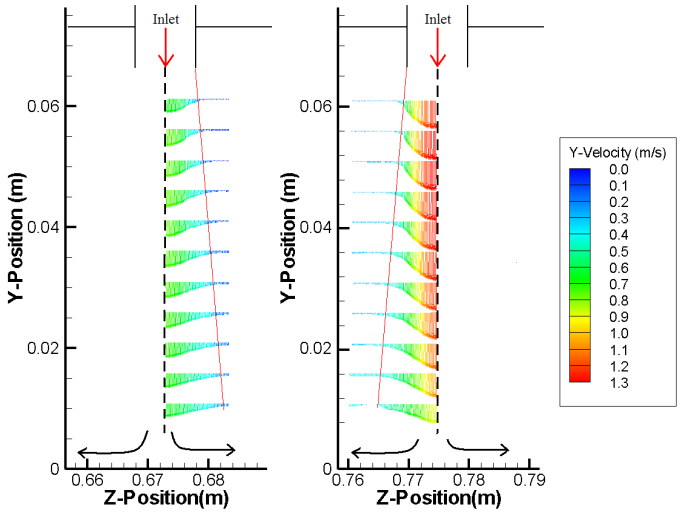

Figure 26. **Velocity profiles along line probes of the averaged experimental data [Amini and Hassan 2009] for the two jets Re=6,250(left) and Re=11,160(right).**

The velocity profiles at the jet nozzle outlets in the experimental data and numerical results differed from one another. The experimental data shows outlet conditions partway between a top-hat velocity profile and a Gaussian profile, whereas the numerical results have a well defined top-hat profile. The different profiles can have profound differences on the turbulent shear layer of the jet wake as demonstrated by New *et al* [2006]. It was shown that a top-hat velocity profile resulted in a dramatic reduction in the dimensionless length y/D to the formation of large scale Kelvin-Helmholtz vorticies in the viscous superlayer around the jet plume. Parabolic entrance profiles tend to produce less coherent vortex structures and increased disintegration of flow structures into small scale eddies.

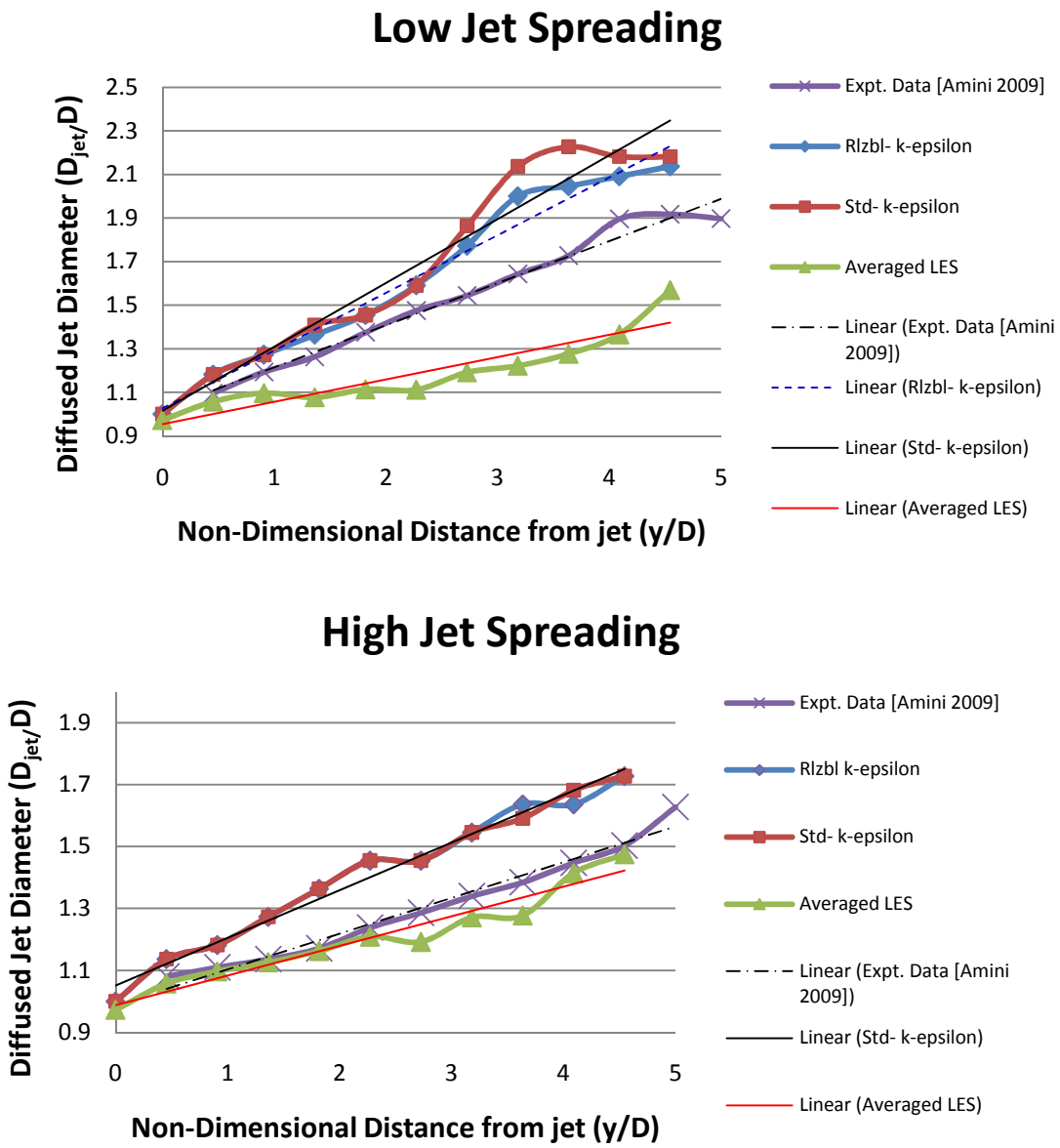

Figure 27. **Spreading jet diameter with respect to distance from inlet nozzle**

Compiling the spreading jet diameters for all the models compared, as well as the experimental data [Amini and Hassan 2009] in figure 27, it is seen that in the case of the high velocity jet, the two variations of the k-epsilon model give nearly identical spreading rates, while the averaged result of the LES simulation has far

less diffusion. Table 3 gives the half angles of the extrapolated line for each jet case. It is possible that this came as a result of a high transfer of turbulent energy from the large scales to the SGS due to a high SGS coefficient, thus leading to decreased mixing in the jet plume and less spreading. This effect has been documented by Ilyushin and Krasinsky [2005] for the Smagorinsky SGS model and a more in depth sensitivity study of the effect of the coefficient choice in the WALE SGS model should be performed. The experimental data falls between both the steady state models as well as the time averaged LES results. The spreading angle of the jets may be estimated by taking the half angle of the linear extrapolations plotted in figure 27.

The spreading angles in the low Re jet illustrate the higher diffusion of the k-epsilon models compared to the experimental data, while the averaged LES results underestimated the spreading angle. While the averaged LES results may have come closer to the averaged experimental data than the other turbulence models for the high Re jet, it is important to keep in mind the effect of averaging on the result as well as uncertainty limits in both experimental data and numerical results. Due to the crude nature of the particular spreading rate analysis, it should not be relied upon independently for determination of model applicability to such flow regimes. Additionally, in the case of highly unsteady flows, steady state and time averaged results can be very limiting.

Table 3. **Spreading half-angles of the two jets using different models**

Jet Case	Low Re Jet	High Re Jet
Experimental Data	4.35°	2.60°
Standard k-epsilon	6.59°	3.46°
Realizable k-epsilon	5.95°	3.46°
LES	2.31°	2.15°

3.2. Recirculation Zones

A key phenomenon present within the lower plenum is the formation of recirculation zones. Within the lower plenum these may present the problem of hot spot formation along the support rods due to insufficient mixing. Two primary recirculation zones are present in the results where the jet plumes impact the columns in the vertical mid-plane. In the standard and realizable k-ε turbulence models, large vorticies were present where the flow strikes the rod and is directed upwards away from the bottom plane. Secondary vorticies are present at the separation point above the main vortex. Near the bottom edge of the rod, the flow appears to separate in the y direction with the flow that goes downwards partially doubling back on itself. This point observed in the time averaged results of the LES simulations presents itself as a small vortex. Vortexes around the base of a cylinder may be an indication of the presence of horseshoe vorticies as seen in previous studies of crossflow around a cylinder [Muzzammil and Gangadhariah 2003].

The steady state results along the vertical mid-planes show the same basic trend with the time average of the LES results. The key differences lie in the size and position of the two primary recirculation zones against the central rod, as well as the presence of secondary and tertiary recirculation zones. The locations midway between the impinging jets and the central rod ($x \approx 0.695$m and 0.750m) show splitting features in the streamlines. In the case of the simulations using the standard and realizable k-ε models, a recirculation zone only appears to be present on the side of the lower Re jet; however, the averaged LES results indicate the presence of a tight vortex on the high Re jet side as well.

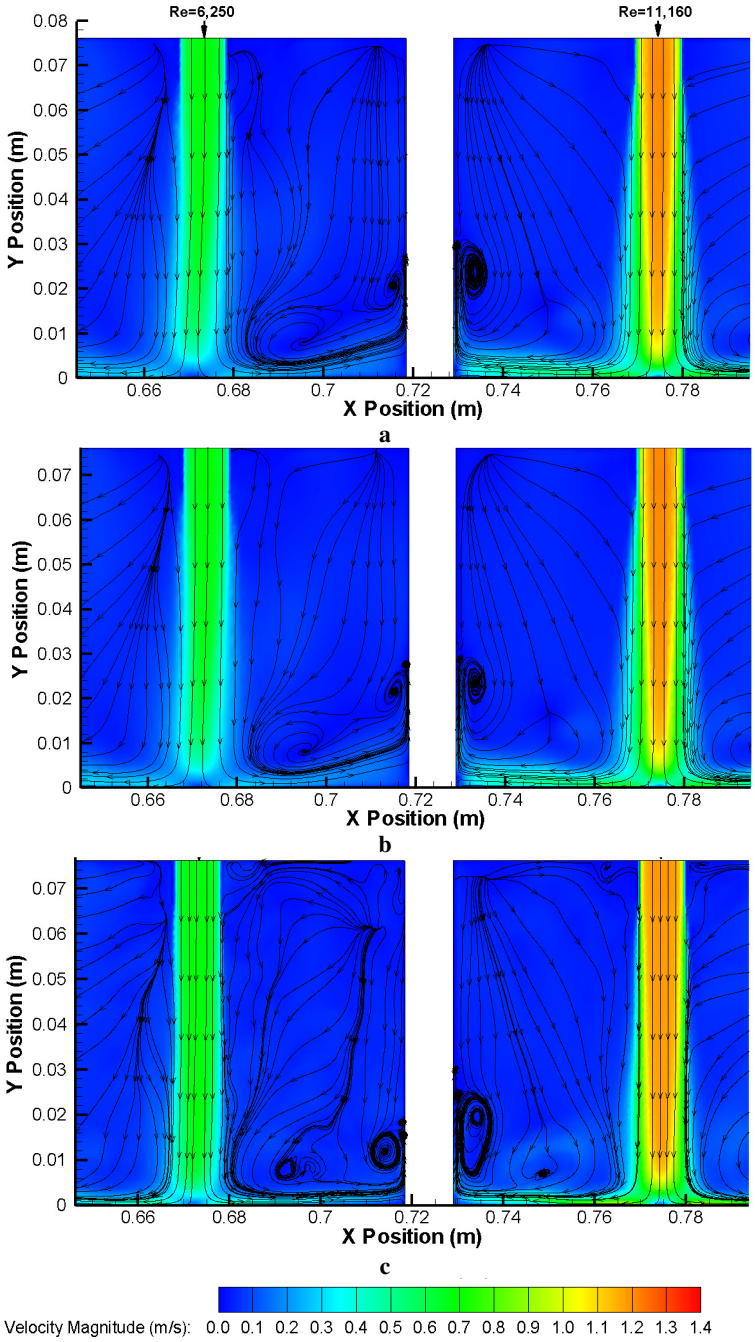

Figure 28. **Steady state results in the vertical mid-plane bisecting the two jets for the *a)*standard k-ε model, the *b)* realizable k-ε model, and *c)* time averaged results from the LES model**

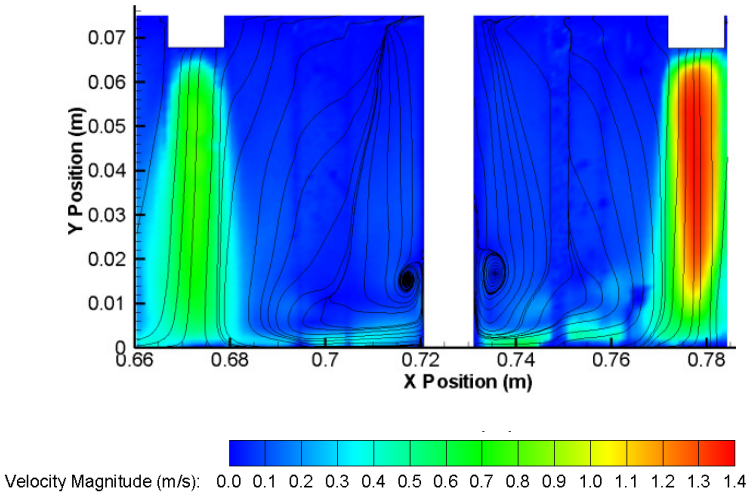

Figure 29. **Time averaged results in the vertical mid-plane for the experimental data [Amini and Hassan 2009]**

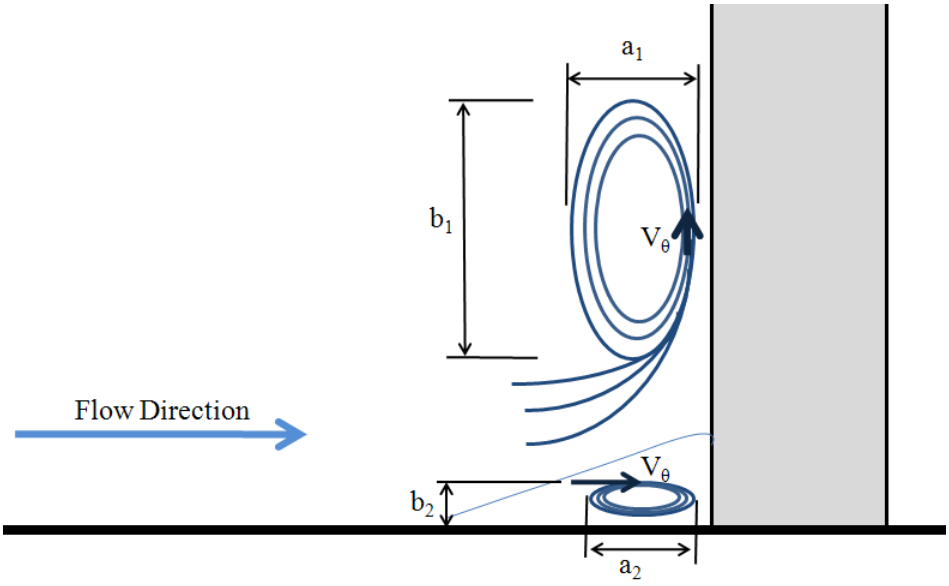

Figure 30. **Definition sketch of quantification metrics for primary and horseshoe vorticies**

Quantifying the size of the vorticies shown in figures 28 and 29 for comparison between models and experimental data is done by calculating the mean vortex diameter D_v, vortex velocity V_θ, and vortex strength Γ from the quantities shown in figure 30. Vortex quantities are defined by equations 29-31.

$$D_v = a_i + b_i \quad (29)$$

$$V_\theta = \pi N D_v \quad (30)$$

$$\Gamma = \pi V_\theta D_v \quad (31)$$

Comparing the results in table 4 between the steady state models, time averaged LES results, and the time averaged experimental data, several model features become evident.

The primary vortex is measured by a_1 and b_1 and the smaller horseshoe vorex by a_2 and b_2. The high Re or low Re designation for the jet vortex refers to which vortex is being quantified. The high Re vortex is on the same side of the central rod as the high Re jet, and likewise is the same for the low Re vortex. The horseshoe vortex was present on both sides of the central rod in the LES results and the metrics are similarly calculated. Between the compared metrics, the realizable k-ε model most nearly simulated the size of the primary vorticies; however the vortex velocity, rotations per second, and vortex strength differed. Strengths of the primary vorticies varied widely between the models and the experimental data. The k-ε models both under predicted the vortex strength in comparison to the experimental data while the time averaged LES results over predicted the result.

Comparing the vortex strength of the primary and horseshoe vortices in the LES results indicates the horseshoe vortex on the high Re number side of the central rod is 2.6 times the strength of the primary vortex on the same side. On the low Re number side, the horseshoe vortex is only 70% the strength of the corresponding primary vortex. Further study both experimentally and numerically on a more refined scale is needed into the interaction to draw more concrete conclusion on the

relation between primary and horseshoe vortex strengths for a complex flow as in this study.

Table 4. **Metrics of primary and horseshoe vortex results**

Turbulence Model	Jet Vortex	Dv (m)	Mean Vel. Mag. (m/s)	Max Vortex Vel. (m/s)	Rotations /s	Vortex Strength (m^2/s)
Realizable k-ε model	High Re	0.0159	0.0280	0.0449	0.9000	0.0039
(Primary vortex)	Low Re	0.0102	0.0176	0.0217	0.6755	0.0012
Standard k-ε model	High Re	0.0187	0.0308	0.0540	0.9195	0.0052
(Primary vortex)	Low Re	0.0097	0.0123	0.0166	0.5454	0.0006
Averaged LES Results	High Re	0.0257	0.0679	0.1086	1.3435	0.0231
(Primary vortex)	Low Re	0.0143	0.0703	0.0935	2.0862	0.0207
Averaged LES Results (Horeshoe Vortex)	High Re	0.0023	0.1244	0.1563	21.7617	0.0610
	Low Re	0.0031	0.0624	0.0738	7.5734	0.0145
Ave. Experimental Results (Primary vortex)	High Re	0.0152	0.0374	0.0701	1.4655	0.0082
[Amini and Hassan 2009]	Low Re	0.0100	0.0297	0.0478	1.5162	0.0045

It is important to remember that the flow is highly three dimensional and that out of plane rods are present at locations midway between the impingement sites and the central rod. These out of plane rods are even closer to the impinging jet and have strong horseshoe vorticies that travel around the base of the cylinders. These vorticies interact in the vicinity of the mid-plane and fluctuations in the horizontal plane take place. In the case of the standard and realizable k-ε turbulence models between the high Re jet and the rod, the steady state aspect of the models contribute to the simulation favoring both sides nearly the same, therefore averaging out each of the counter-rotating vorticies formed by the flow striking the out of plane rods. In the case of the averaged LES results, it is possible that one side was favored

slightly more than another, leading to the presence of a small vortex in this region. Between the lower Re jet and the central rod, recirculation zones were observed for all cases, but the averaged LES results showed a larger more pronounced zone (figure 28c).

The time averaged experimental data [Amini and Hassan 2009] shown in figure 29 indicates the presence of the same two primary recirculation zones adjacent to the center rod. The same characteristic splitting of the streamlines as the out of plane features alter the flow patterns, although there was no identification of a vortex in this location. It is possible that the experimental uncertainty, as well as the averaging of data acquired in 5000 frames taken over five seconds averaged out such vorticies.

In the unsteady LES results, entrainment features are more readily identified than in the steady state results due to averaging. High jet entrainment of the surrounding semi-quiescent fluid is indicated by the streamline tendency towards the jets. Jet entrainment is highly dependent on viscous interaction between the surrounding fluid and the jet at the viscous superlayer. Instability at the inlet location induces a slight pressure gradient in the jet plume. The result of an initial perturbation of the jet is the development of a strong Kelvin-Helmholtz instability. This perturbation causes the jet core region to shrink causing an increase in speed as mass is conserved within the viscous superlayer. This increase in velocity in turn results in a reduction in pressure according to Bernoulli's principle which leads to a further buildup in the plume. The resulting vortex that is produced axisymetrically around the jet plume travels down until it reaches the impingement layer, growing as

it travels further into the domain. This ring vortex formation leads to the presence of what will be referred to as psuedo slugs within the jet plume. The term pseudo slugs stems from the presence of very high entensity pressure and velocity waves in these necked locations that travel with a very high periodicity.

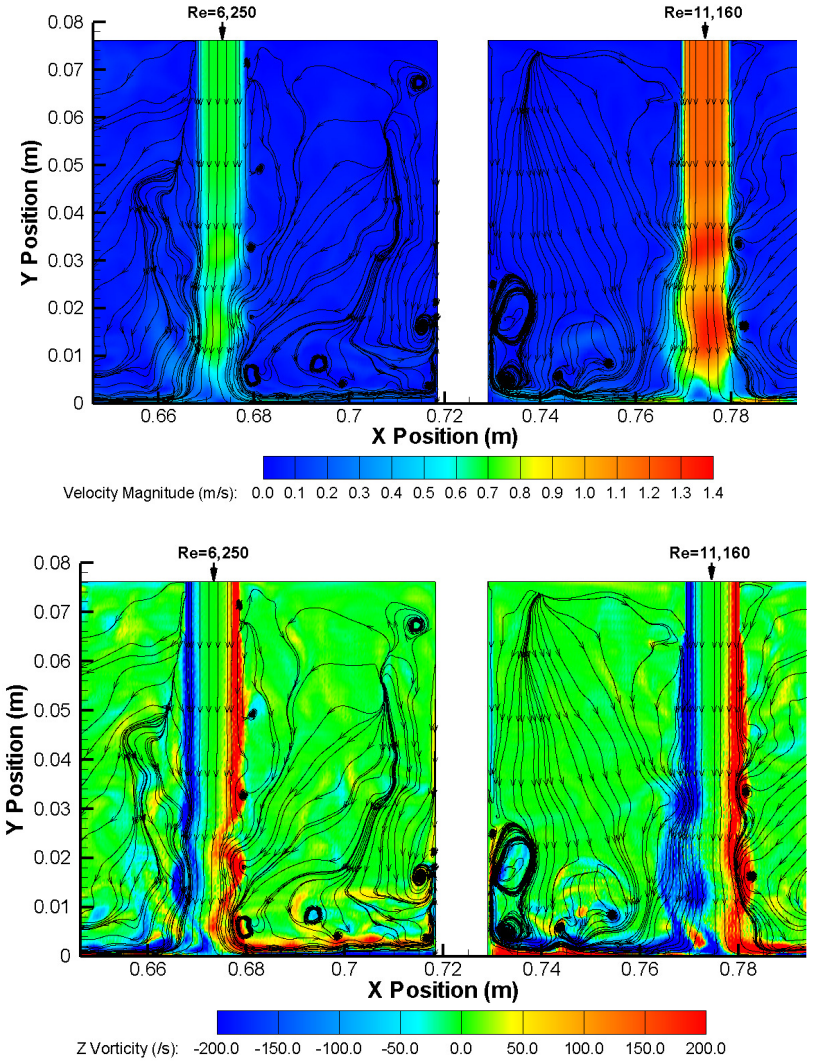

Figure 31. **Instantaneous velocities and out of plane Z vorticity components illustrating vortex structures in the viscous superlayer**

The necking of the jet and formation of ring vorticies has been observed in experimental works for round jets in the same range of Reynolds numbers as investigated in the present work [F. Shu *et al.* 2005]. In the case of a jet that has a top-hat profile as opposed to a Gaussian profile, a reduced distance (y/D) to the onset of vortex rings has been documented [New *et al* 2006] and it is possible that the strong presence of these structures in the numerical results but not the experimental data is due to slightly different entrance profiles causing the presence of different entrainment regimes within the domain. The velocity and vorticity fields in figure 31 as well as the iso-surface plot in figure 32 show the formation of tight vortex rings and the high velocity in the jet at these necked locations due to the Kelvin-Helmholtz instability.

In the near wall region at the base of the rod, a very tight vortex is present in the time averaged LES results. Figure 33 illustrates the position of horsehoe vorticies along the base of the cylinder adjacent to the impinging flow and figure 34 shows the location of the resulting shadow zone following the cylinder. Doubling back of streamlines as seen in figure 35, in the k-ε models indicate a possible horseshoe vortex that was not completely resolved. Instantaneous LES results in figure 36 show a large well defined vortex present in this location. In the case of the experimental data shown in figure 37, this vortex is not present. It is possible that the horseshoe vortex is not present in the actual case; however it should be noted that measurements in this region cannot be said to be conclusive due to obstructions and aberrations in the wall material near the edges of the experimental facility.

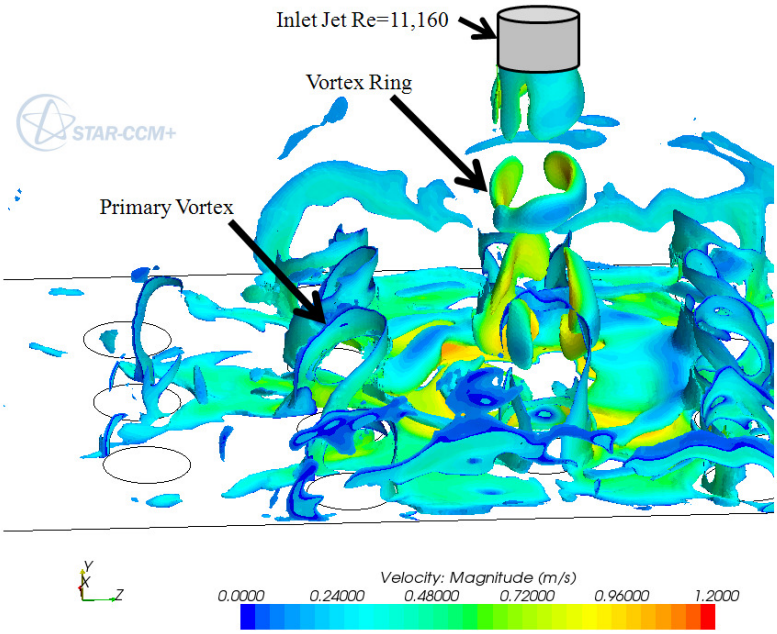

Figure 32. **Vorticity iso-surfaces with velocity magnitude scalar coloration of instantaneous LES results**

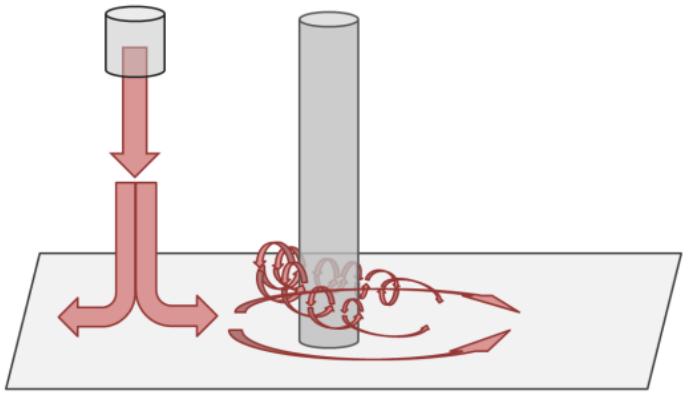

Figure 33. **Single horseshoe vortex around a column**

The importance of these horseshoe vorticies is threefold. The first is the potential formation of hotspots in these locations; the second is the possible abrasion at the base of the graphite support rods; and the third is the settling of dust particles in the shadow zone in the wake of the support rod. The nearly constant presence of

high intensity horseshoe vorticies, illustrated by figure 33, around the base of the cylinders could be points of high abrasion for a material prone to dust formation such as graphite if wear particles are present in the gas flow. Muzzammil and Gangadhariah [2003] experimentally investigated the presence of the horseshoe vortex formed around the base of a pier column in a crossflow and the key role played by this vortex in the scour of the surrounding base. While the case of scour at a pier base is focused on sand removal from the location of the vortex, the presence of wear particles in the flow, such as other dust particles released from the core, could potentially abrade the lower graphite plate. The insulation later at the bottom of the lower plenum of the VHTR is composed of one meter of nuclear graphite and 200mm of carbon-carbon composite [MacDonald 2003].

While the possible abrasion that might result in the locations of the horseshoe vorticies is a point of interest, the potentially more important issue lies in the shadow zones of the rods. In the horizontal plane 2mm from the plane of impingement, shadow zones presented themselves in the results. Shadow zones are features observed in the wake of horseshoe vorticies just following the cylinder and before the onset of the turbulent instabilities. This phenomenon has been described by Greenly and Iverson [1985] as the reason for dust buildup just behind obstructions in windy conditions. These zones are important as they may act as traps for the dust produced in the reactor core. These particles will not be filtered out of the system properly and in the event of a large break loss of coolant accident (LOCA) scenario, the rapid depressurization of the reactor vessel would cause any such buildups to be released suddenly from the vessel into the containment.

Shadow zones are observed for most locations following rods in the numerical results as regions of relatively stagnant flow, although the size and shape vary largely based on the location relative to the two impinging jets. It may be seen in the instantaneous velocity profile of the LES results that the impinged jet at a given instance tends to one side of the central rod.

The steady state and time averaged LES results in figure 38 indicate an even distribution to both sides of the rod. Figure 39 presents an instantaneous snapshot of the flow and shows a clear channeling to one side of the central rod. From the times averaged result and this instantaneous result, there is turbulent switching in the bundle; however, the switching is evenly distributed to both sides of the bundle. Experimental data in the horizontal plane to validate this result was not available at the time of this study.

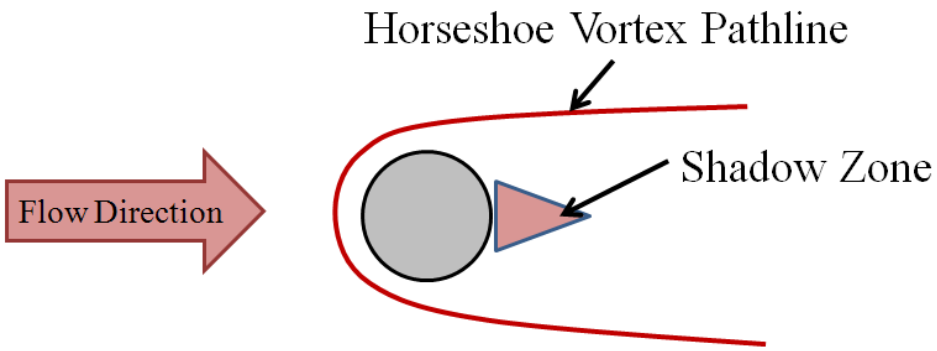

Figure 34. **Shadow zone in the wake just following a cylindrical obstruction**

These results are in agreement with those seen by Johnson *et al* [2006] in which the presence of standing wakes downstream of the cylinders were seen. Their unsteady simulations and experimental data seem to confirm these shadow zones as

standing wakes following the cylinders; however, at the time of the publication it was unsure as to the accuracy of both the numerical results and experimental data. The results presented in the subsequent wavelet transform section indicate very low velocities in these locations; however, there were still measurable frequencies in the ranges calculated by means of the of the Strouhal number equation for the case of uniform flow past cylindrical structures.

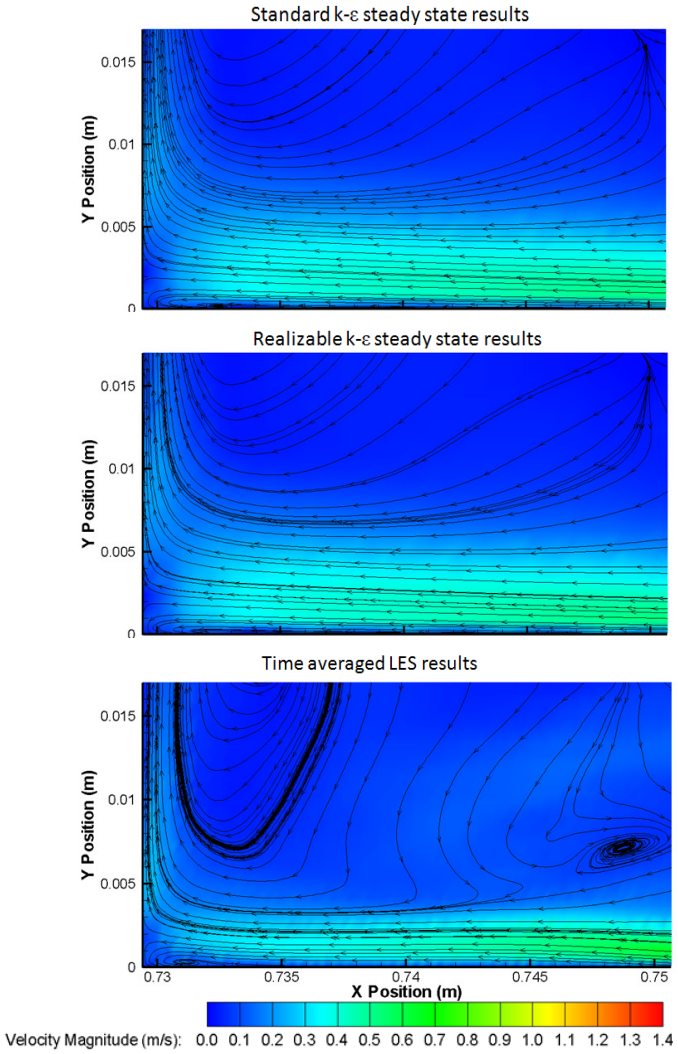

Figure 35. **Numerical results of flow along the vertical mid-plane at the central cylinder base (located at x=0.729m)**

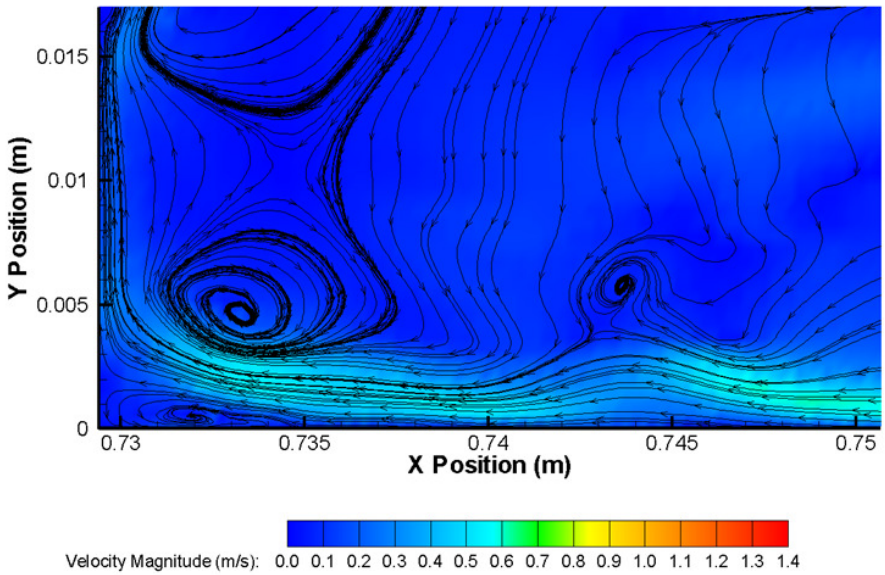

Figure 36. **Instantaneous LES results of flow along the vertical mid-plane at the central cylinder base (located at x=0.729m)**

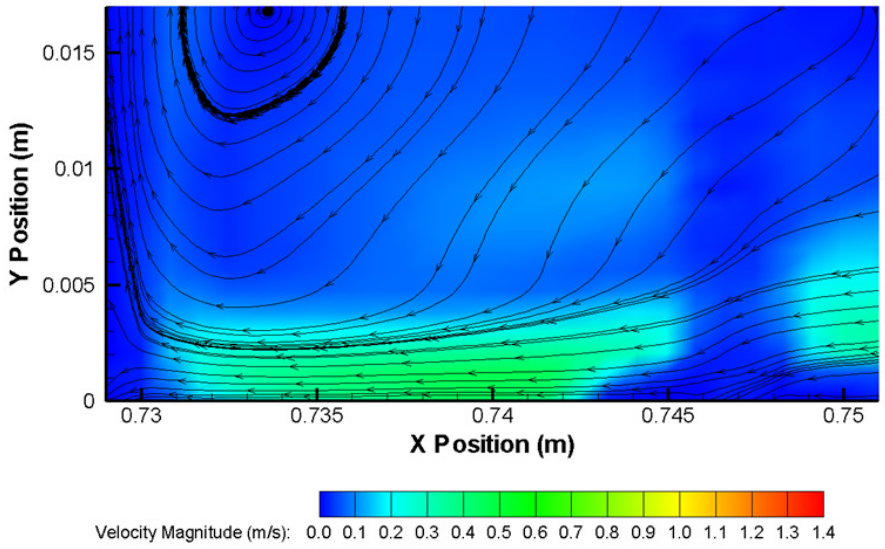

Figure 37. **Time averaged experimental data of flow along the vertical mid-plane at the central cylinder base (located at x=0.729m)**

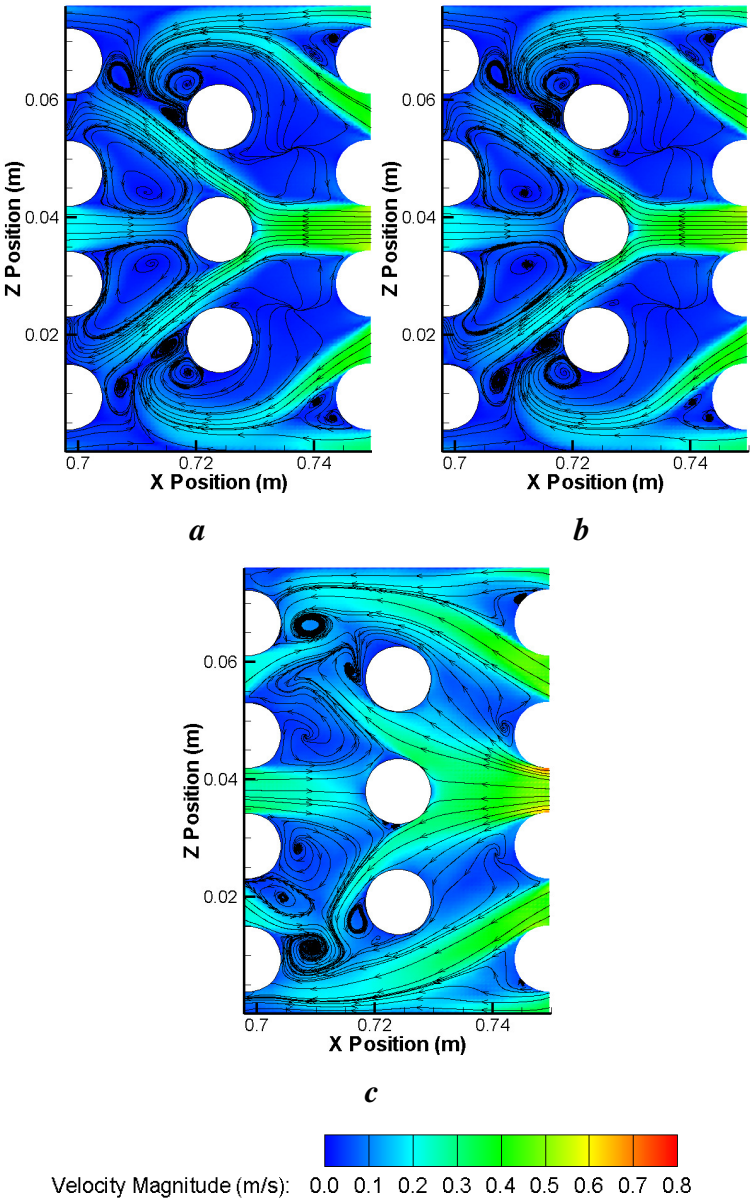

Figure 38. **Steady state results in the horizontal plane 2mm from the bottom plane for the *a)*standard k-ε model, the *b)* realizable k-ε model, and *c)* time averaged results from the LES model**

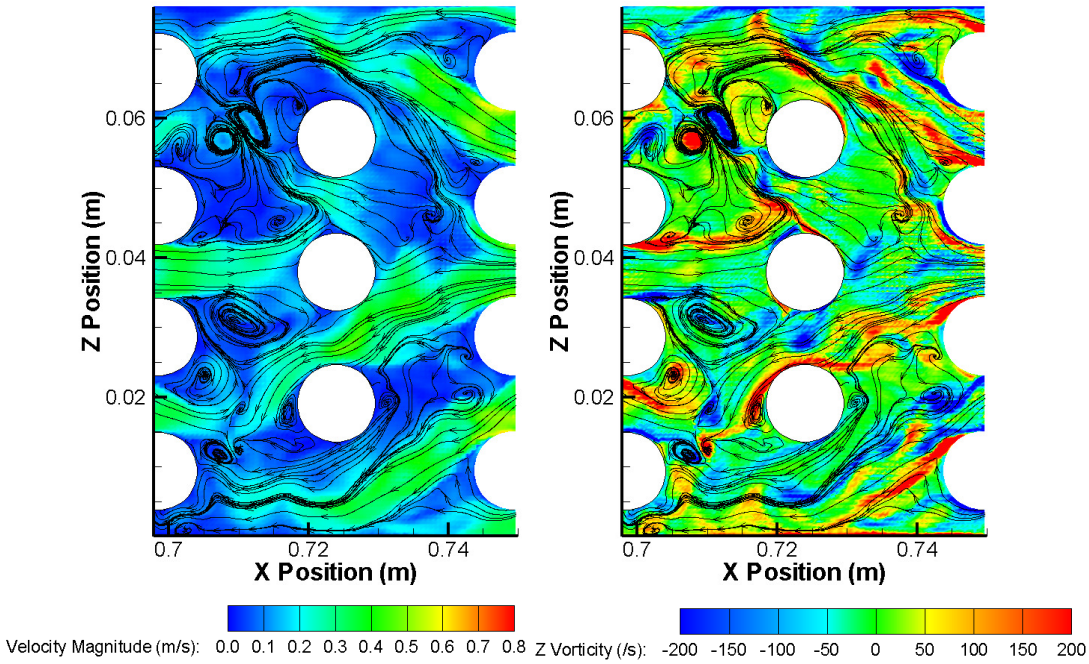

Figure 39. **Instantaneous LES results of velocity and out of plane vorticity scalars**

3.3. Wavelet Transform Frequency Analysis

A difficulty in the analysis of unsteady CFD simulations is the amount of information present in the results. To focus the scope of this work, transient signals were extracted from the results in the vertical mid-plane bisecting the two inlets as well as a horizontal plane 2mm from the bottom. The horizontal plane at y=2mm was chosen because it lies in the impingement plane of the jets and the vortex shedding in the flow past the cylinders is present as well.

Signals in the vertical midplane were extracted from the results at the locations shown in figure 40. The Morlet mother wavelet was used for its ability to identify sharp gradients in the signal. This characteristic ability gives it particularly good frequency resolution as opposed to some of the other mother wavelets. The continuous wavelet decomposition of the velocity magnitude signal at point 10

(figure 41) illustrates the dominant frequency introduced by the periodic Kelvin-Helmholtz(KH) instability of the entrainment of surrounding fluid in the location two diameters from the jet inlet. The dominant frequency present occurs around 43 Hz as seen in both the wavelet coefficient plot as well as the peak at 43 Hz in the FFT plot. The decomposition of the signal obtained at point 2, 6.5 diameters from the inlet jet, is shown in figure 42. The dominant frequency remains the same as before; however, the intensity has increased as the KH instability continues to grow. Additional frequencies are detected in the range of 10Hz to 30Hz. The source of these frequencies remains unknown for certain; however, it seems possible that these are the result of fluctuations in the centroid of the impingement location about the signal location.

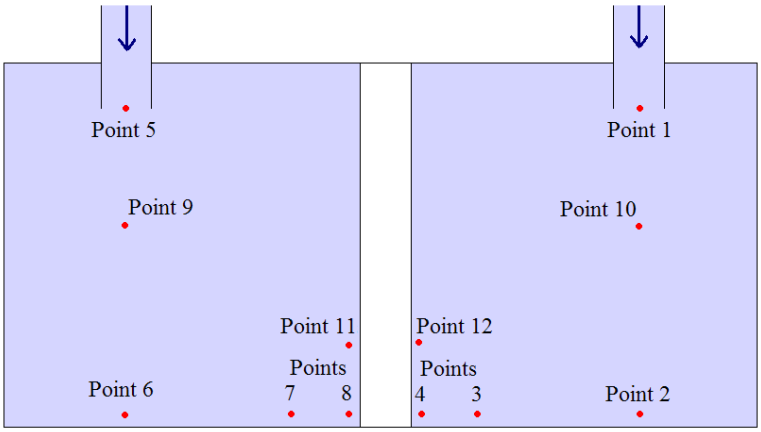

Figure 40. **Extraction point locations along the vertical mid-plane for wavelet analysis**

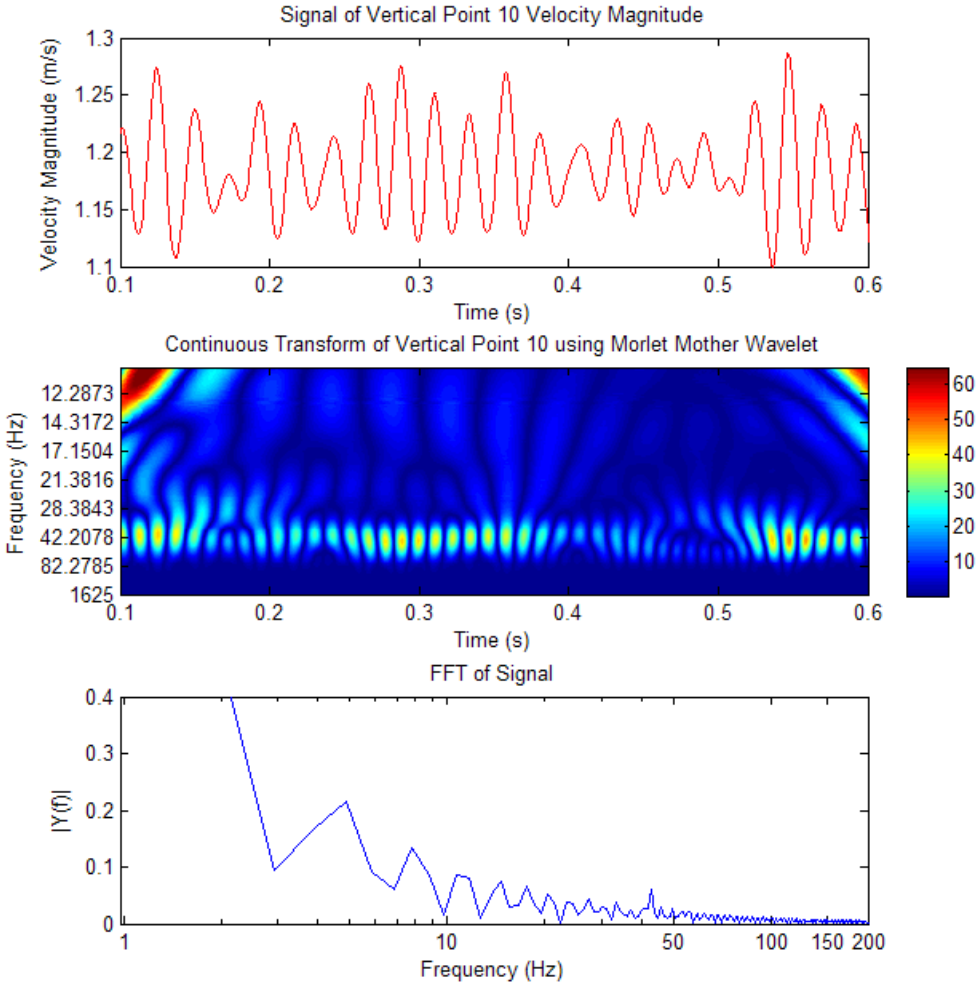

Figure 41. **Wavelet transform of vertical point 10 using the Morlet mother wavelet**

As the jet spreading occurs, fluctuations induced by the presence of out of plane rods as well as turbulent spots along the lower plane of the channel alter the characteristic frequencies in the flow. The decompositions of points 4 and 4 in figures 43 and 44 show results along the lower impingement plane just prior to impinging the central rod. Newly introduced turbulent frequencies in the range of 7 Hz to 30 Hz are seen due to other sources. It should be noted that frequencies present in the very low range of less than 4 Hz should be taken with care. The

filtering mechanism of the wavelet transform is such that the low pass filters require a longer signal to avoid influence of the finiteness of the signal.

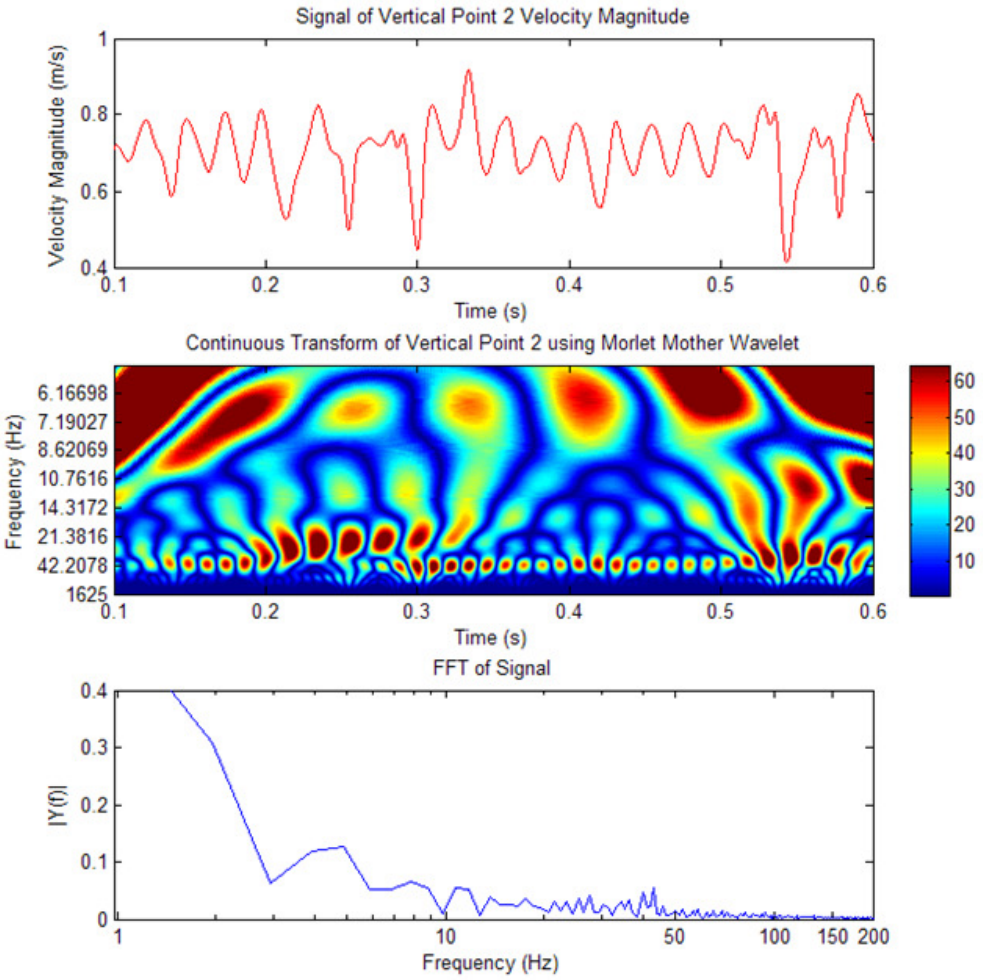

Figure 42. **Wavelet transform of vertical point 2 using the Morlet mother wavelet**

The presence of the frequency spike at 7.8 Hz in the signals of both points 3 and 4 can be linked to the vortex shedding of the out of plane rods. The impingement layer of the jet is a high velocity flow approximately 3-4mm thick extends outward from the impingement locations. The mean velocity magnitude of

the time averaged LES results for the region indicated in figure 45 is 0.435m/s. The Reynolds number for flow across a cylinder depends on the region over which the average velocity is taken.

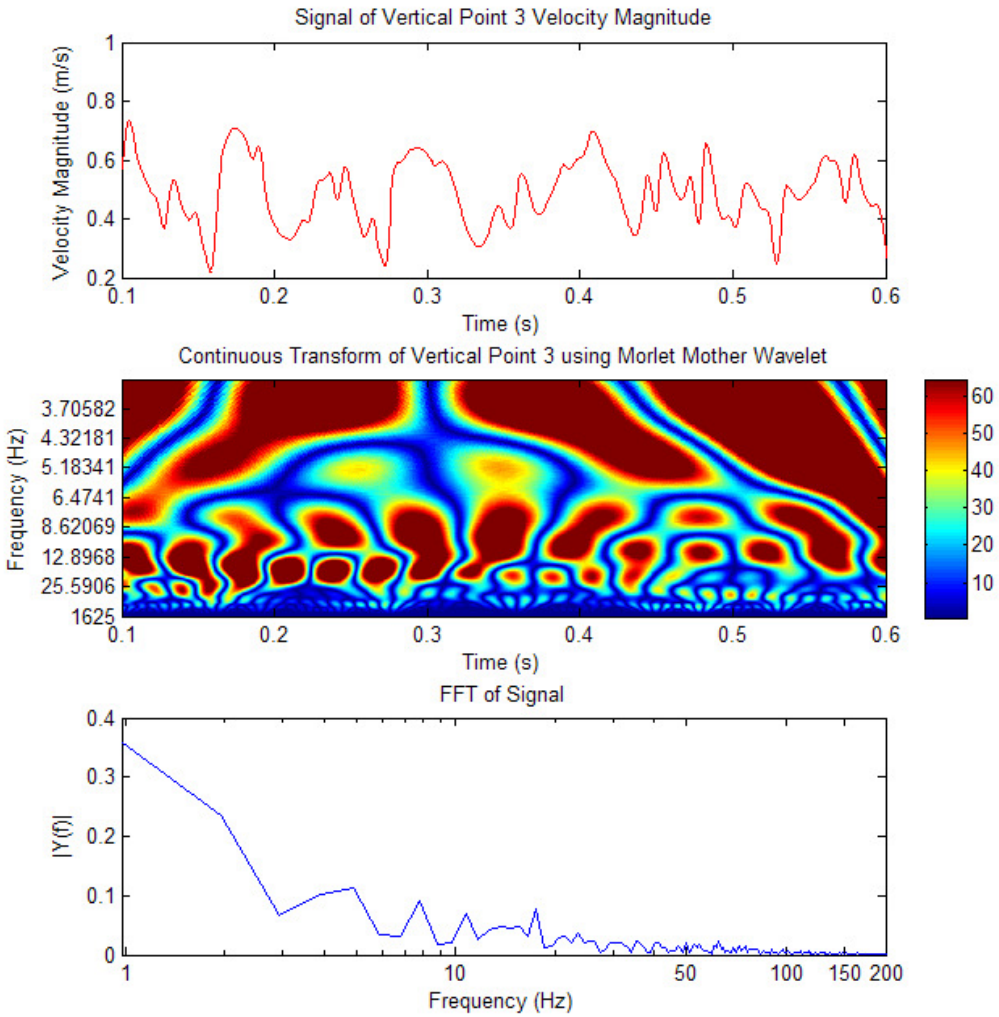

Figure 43. **Wavelet transform of vertical point 3 using the Morlet mother wavelet**

Vortex shedding frequency calculations using the equation for the Sr number should be approached with caution in the case of this study. Variation in the size of the region of interest changes the mean Reynolds number used in the calculation.

The Strouhal-Reynolds number relationship (*Eq.32*) developed by Roshko [1954] between Reynolds numbers of 300 and 10,000 gave a Strouhal number within 4% of the best fit of experimental data for uniform flow over a cylinder. While this error might be low, the presence of multiple regime changes within this region should be noted. Like Roshko, Bloor [1963] observed irregularities in the 200<Re<400 range as well, but suggested that in this range turbulence was introduced by three dimensional effects. Above Re=400, transition takes place before the separation layer curls up. Regularity in the signal was found to only occur when transition occurred well within the separated region. Bloor determined this occurred for Reynolds numbers above 1,300. In the near wall region of the present study, the averaged Reynolds number was 4,641 which put the flow regime past the cylinder near the transition between the subcritical flow regime and the presence of Kelvin-Helmholtz vortices in the shear layer [Fey *et al.* 1998]. The Strouhal number based on Roshko's formulation was 0.211 for this mean Re number. When the region of averaging was enlarged to include more of the low velocity core region, the difference in the Reynolds number changes the calculated frequency enough to note.

$$Sr = 0.212 - \frac{2.7}{Re} \tag{32}$$

$$Sr = \frac{f \cdot D}{V} \tag{33}$$

$$f = \frac{Sr \cdot V}{D} = \frac{0.211 \cdot 0.435}{0.01067} = 8.60Hz \tag{34}$$

If the Sr number is reduced, or the average velocity region is expanded, the effect on the frequency may be altered up or down by a few of Hz. Regions with the

same widths but with heights of 3mm and 2mm had mean velocities of 0.360m/s and 0.435m/s respectively. For the lower mean velocity region, Sr changes a negligible amount; however the shedding frequency reduced to 7.12Hz. The wavelet transforms indicate that frequencies vary in time and drift in and out of different regimes as the flow patterns evolve. It seems acceptable to take the results of the Sr number calculation as a general guide in identifying the source of dominant frequencies as long as this variability is kept in mind.

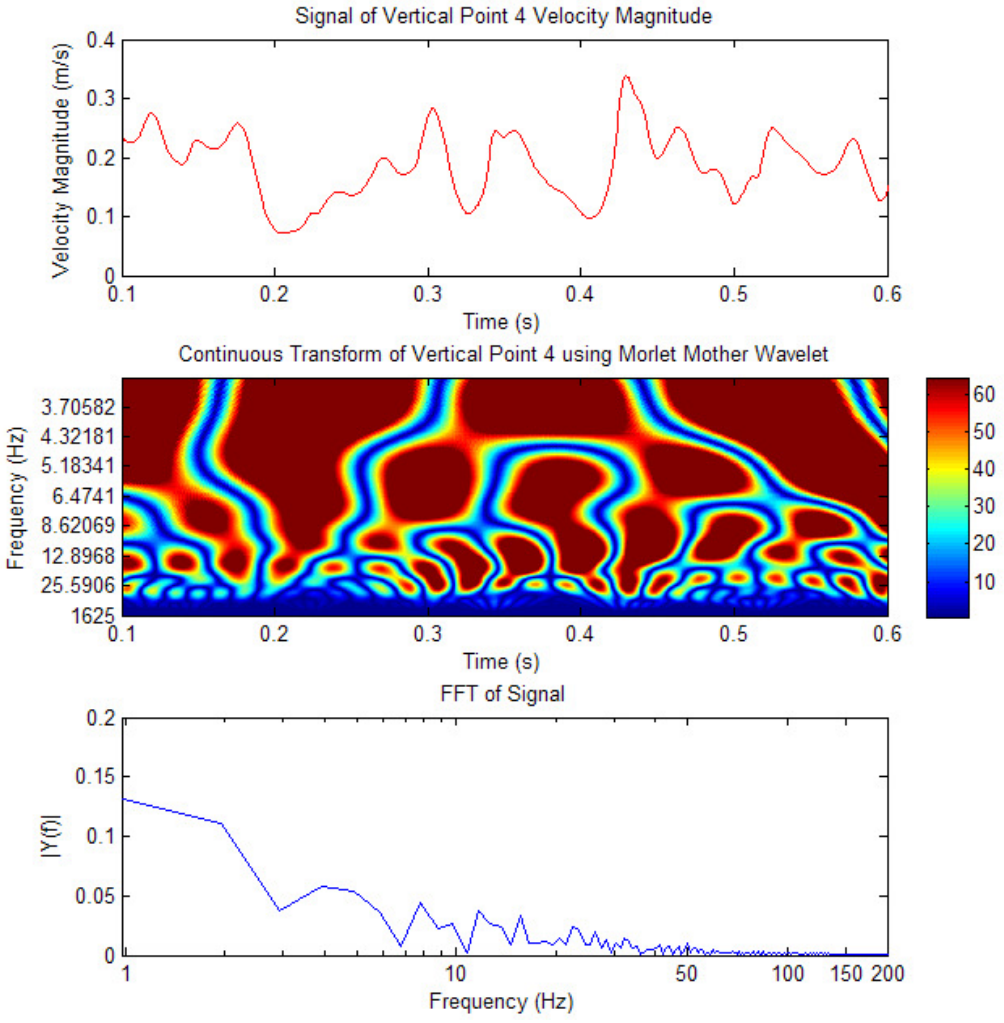

Figure 44. **Wavelet transform of vertical point 4 using the Morlet mother wavelet**

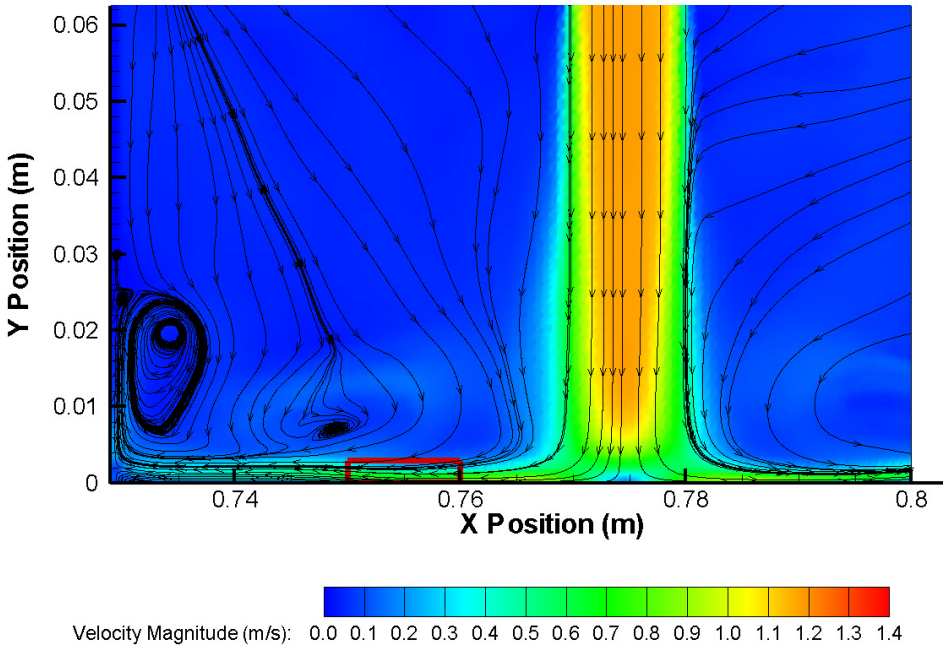

Figure 45. **Zone of velocity averaging in time averaged LES results for frequency estimation**

Looking at the low Re jet signal decomposition of point 9 in figure 46, the entrainment fluctuations observed are 24.4 Hz which is approximately half the frequency of that seen as in the high Re jet. The ratio of Reynolds numbers between high and low jets is equivalent to the ratio of the dominant frequencies in each jet within 0.4% of one other.

The wavelet transform of the signal at point 6 (figure 47) taken along the bottom plane below the low Re jet has remnants of the 24 Hz dominant frequency generated by the KH instability in the jet superlayer, but has also developed frequencies characteristic to point 2 taken below the high Re jet. A characteristic frequency around 7 Hz again presents itself and another around 20 Hz. After observing the presence the 7 Hz frequency in various locations within the vertical mid-plane of the channel, the next step performed was the same frequency analysis

of signals acquired within the thin horizontal impingement layer at y=2mm from the lower plane. The remaining vertical mid-plane points may be found in Appendix A.

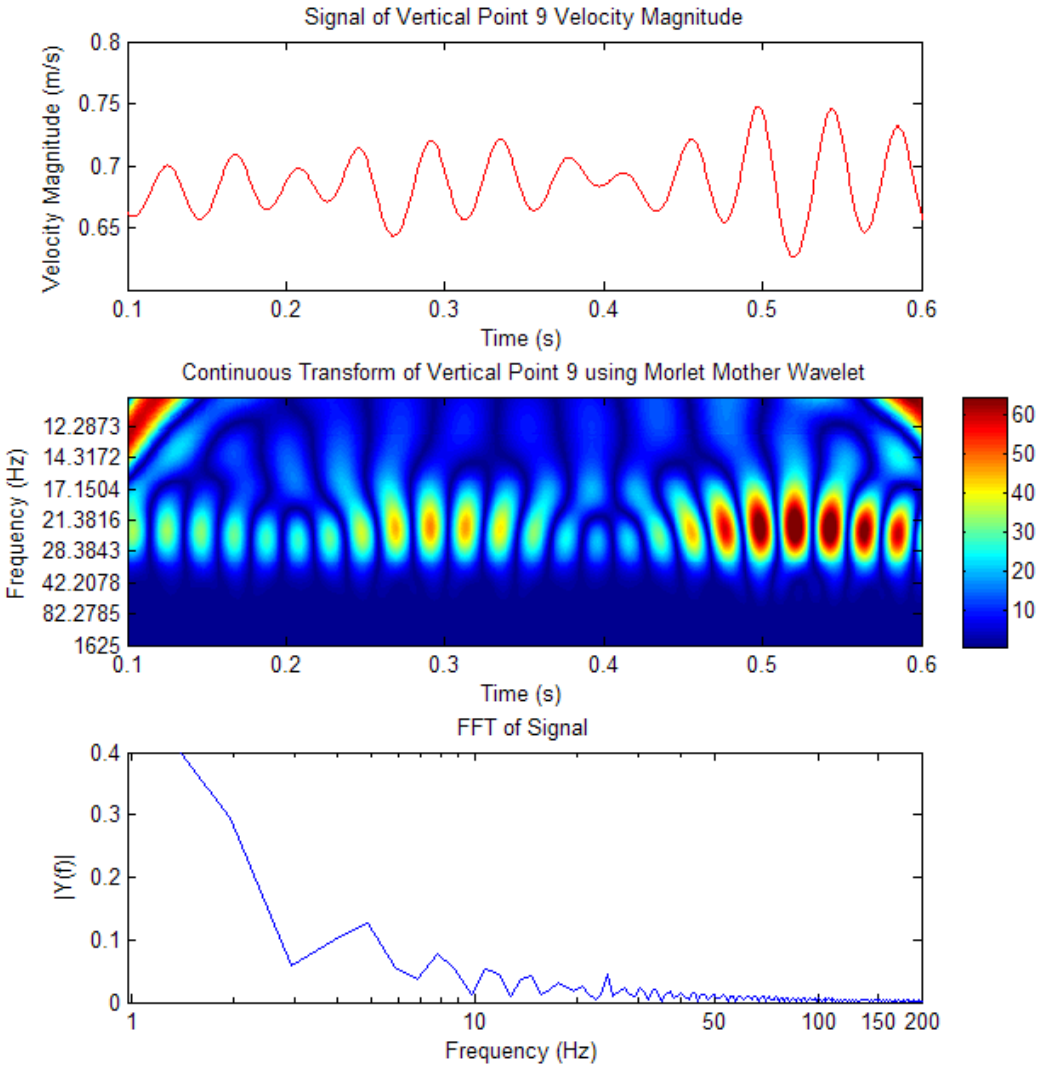

Figure 46. **Wavelet transform of vertical point 9 using the Morlet mother wavelet**

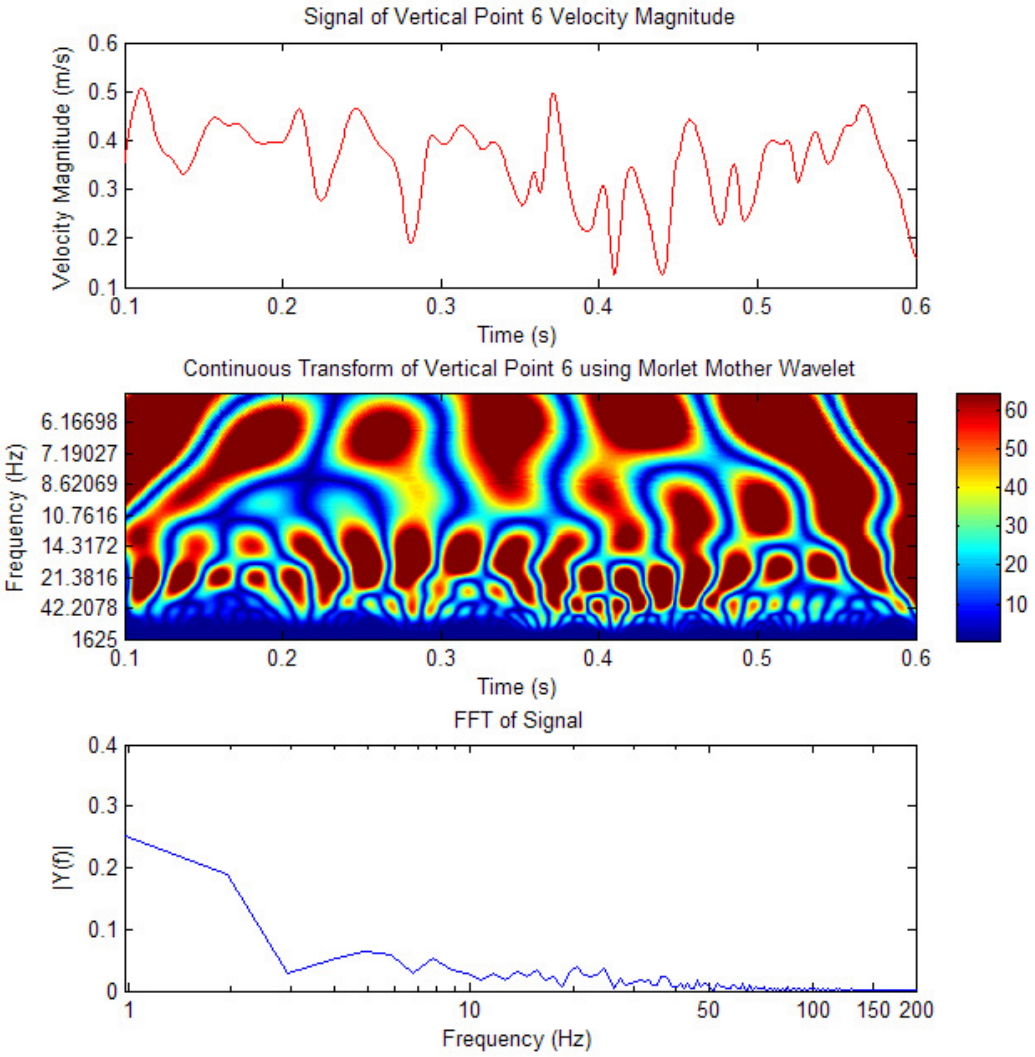

Figure 47. **Wavelet transform of vertical point 6 using the Morlet mother wavelet**

Frequency decomposition was also done for points in the horizontal plane 2mm from the bottom and in the locations indicated in figure 48. The decomposition for point 1 in figure 49 showed a shift in the signal frequency at the 20 Hz range to 42 Hz between times 0.1s and 0.25s and then back down to 30 Hz by t=0.4s. The velocity magnitude signal at this point shows that the velocity increased from a low of around 0.03m/s at 0.15s to a high of around 0.30m/s around 0.3s before again

reducing through the remainder of the signal. There is an apparent correlation with the increase in the mean velocity to the increase in frequencies in the high range.

The signal at point two in figure 50, which just follows the rod midway between the high Re jet impingement site shows similar dominant frequencies to those in point 3 of the vertical mid-plane (indicated in blue font in figure 48). A low frequency around 4 Hz is present over the entire time domain and a well defined frequency around the 8 Hz range is present from 0.1s until 0.45s at which point it transitions to a higher range of 13 Hz with remnants of the 8 Hz signal still present.

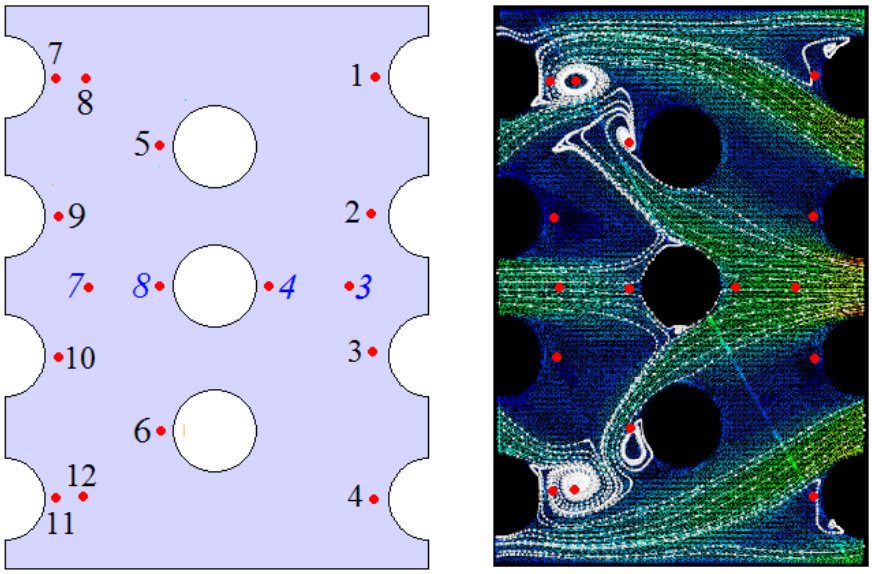

Figure 48. **Locations of signal probes in the horizontal plane 2mm from the bottom plane. Numbers in blue signify the points previously obtained in the vertical mid-plane**

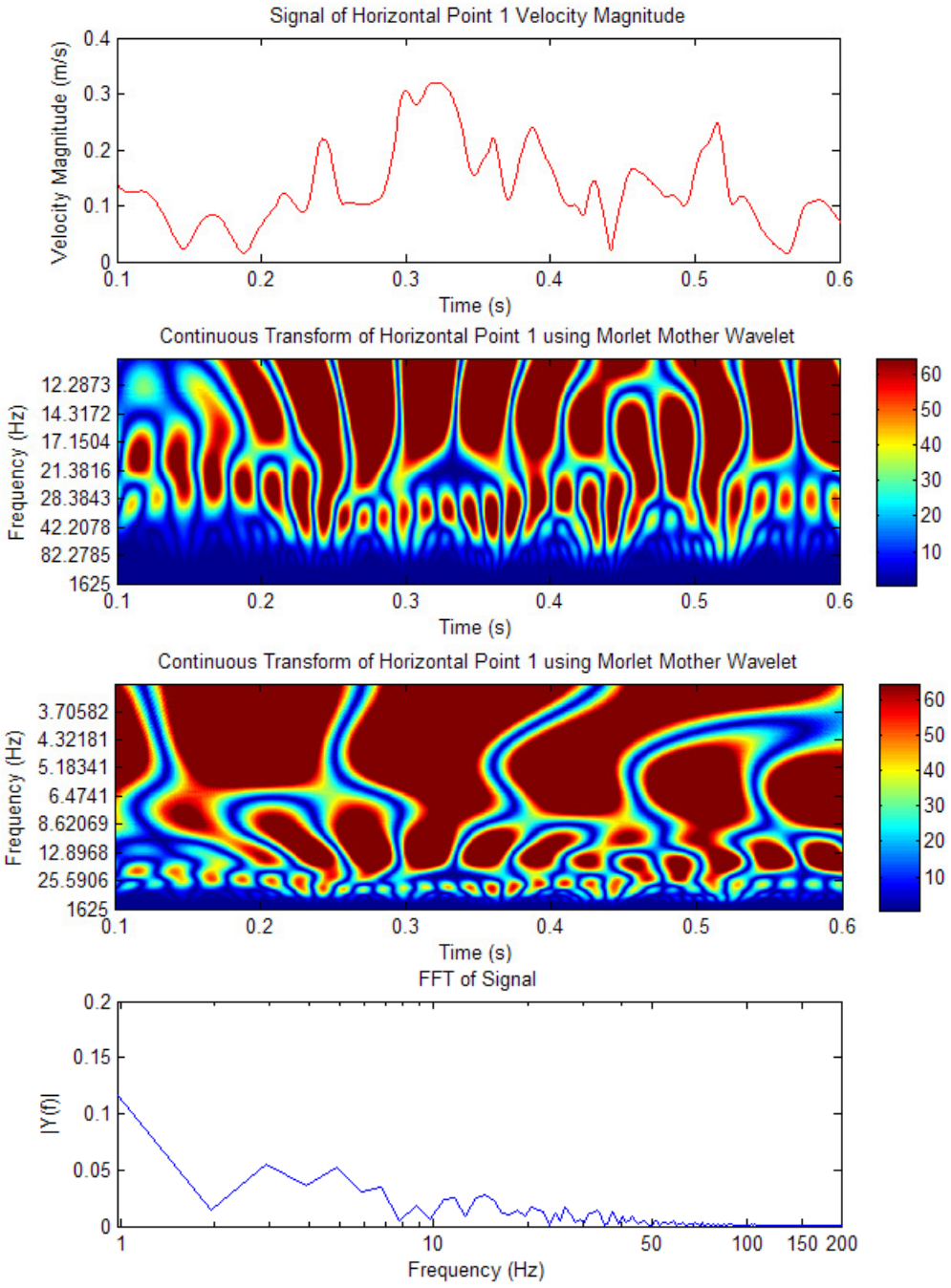

Figure 49. **Wavelet transform of horizontal point 1 using the Morlet mother wavelet**

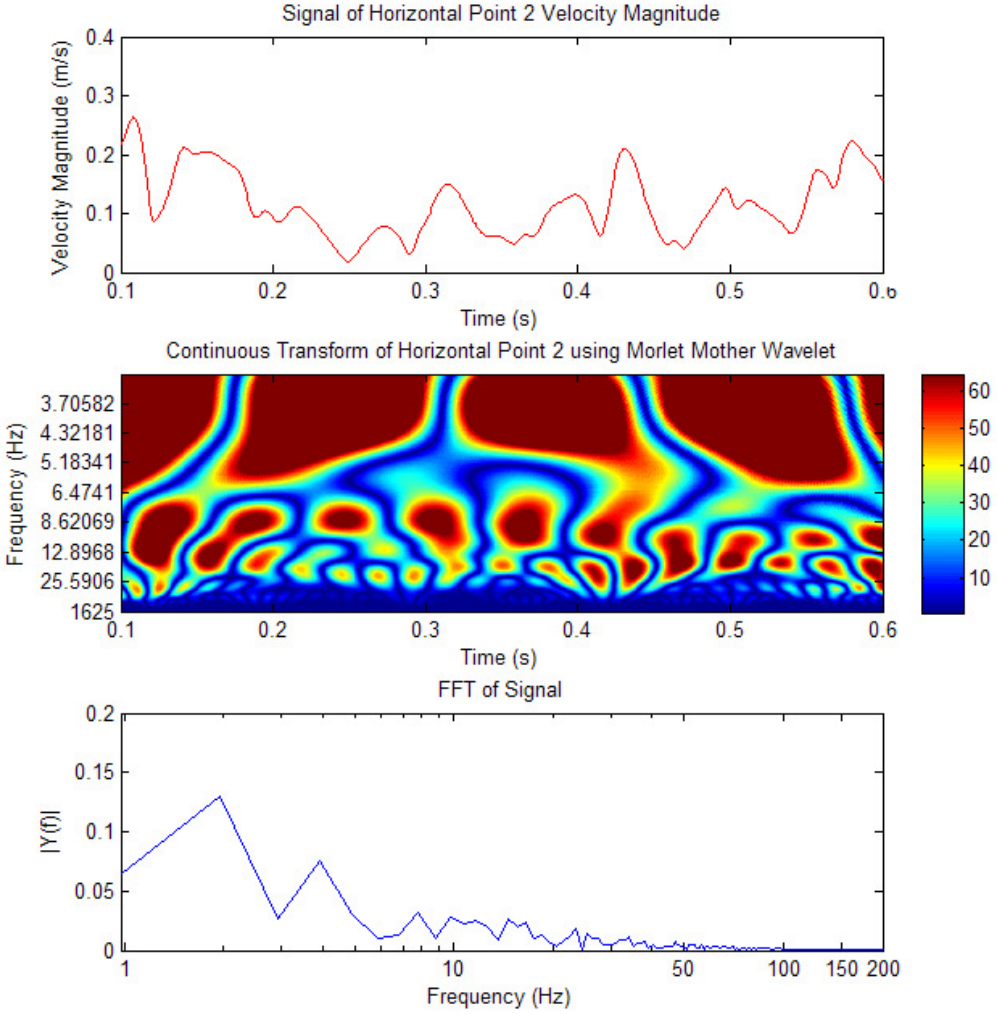

Figure 50. **Wavelet transform of horizontal point 2 using the Morlet mother wavelet**

When this signal was compared with that of point 3 in the horizontal plane (figure 51), a dominant frequency was seen at 3-4 Hz throughout the time domain similar to point 2. There was also a frequency present around 13 Hz in between times 0.1s and 0.445s at which point it diminished. Between 0.1s and 0.45s, both points 2 and 3 had distinctively different frequencies. As the 13 Hz frequency diminished in the point 3 signal at 0.45s, signal 2 picked up traces of the same

frequency. This shift seems to indicate a change in the channeling of flow from one side of the central rod to the other. The time average of the flow in the horizontal plane for the LES results indicate that there is an equal preference to both sides, while the unsteady results indicate a characteristic switching of the flow from one side to the other as opposed to reaching a steady state free of large fluctuations.

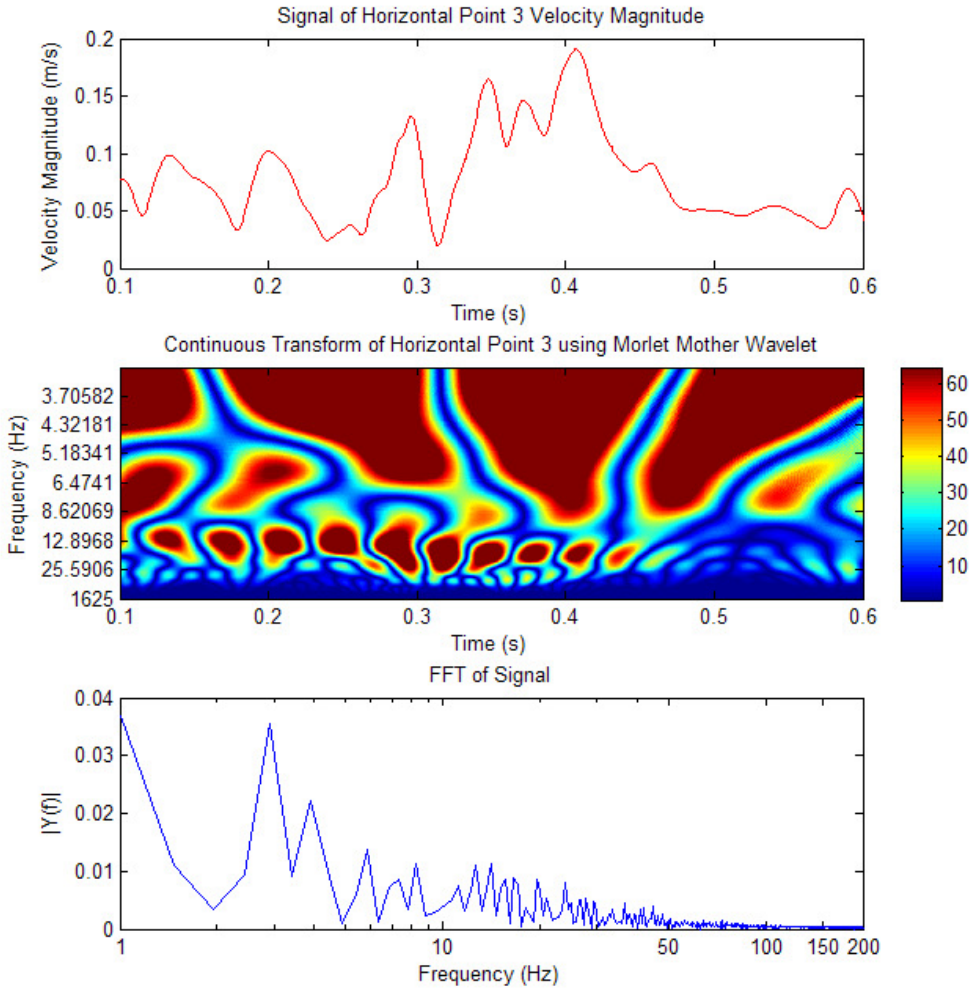

Figure 51. **Wavelet transform of horizontal point 3 using the Morlet mother wavelet**

At signal locations 5 and 6 (figures 52 and 53), a dominant frequency was present around 6 Hz and the two signals were out of phase from one another by

about 0.25s. As the flow from the high Re jet impingement hit the central rod and lost much of its momentum upward, the remaining flow split to both sides of the rod. As the split flow passes the secondary rods, turbulent fluctuations are generated by the flow separation from these rods in the same fashion as before but with a decreased frequency due to the lower velocity as the impinged flow continue to decay further from the impingement site.

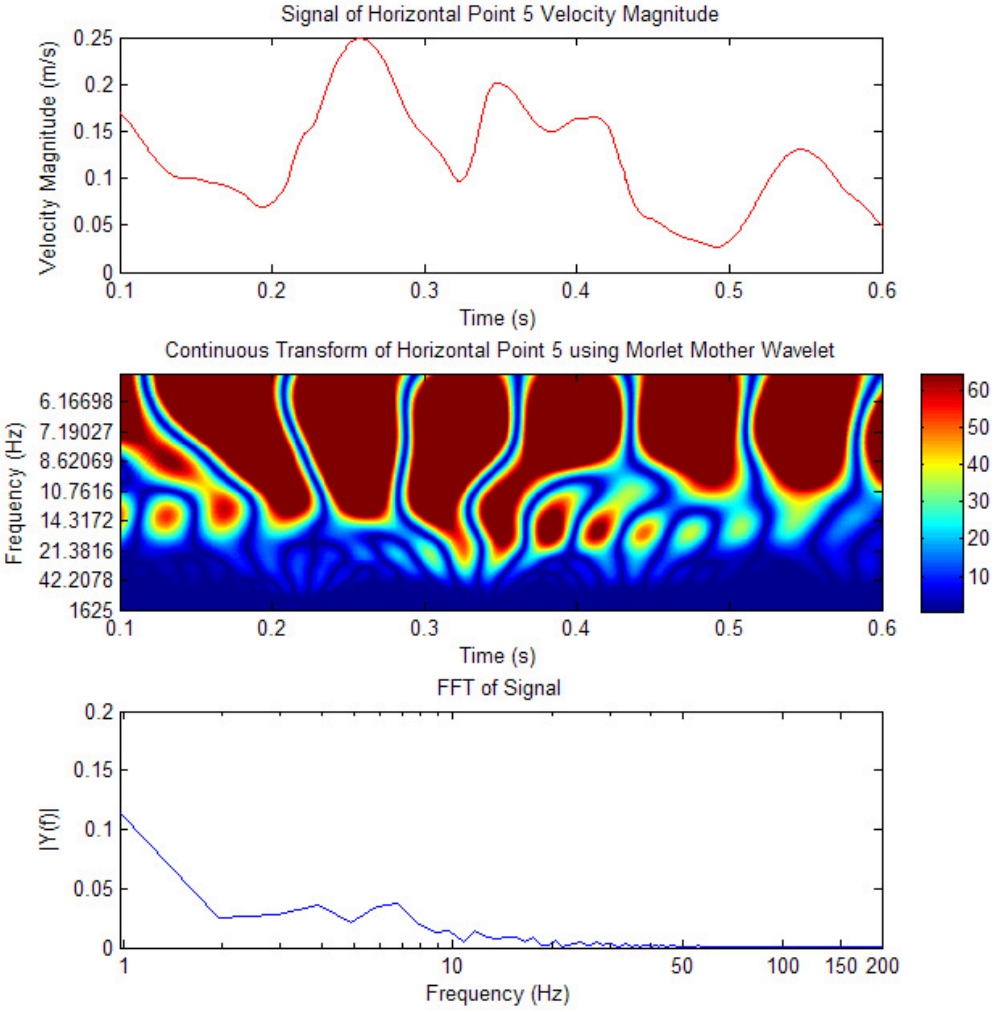

Figure 52. **Wavelet transform of horizontal point 5 using the Morlet mother wavelet**

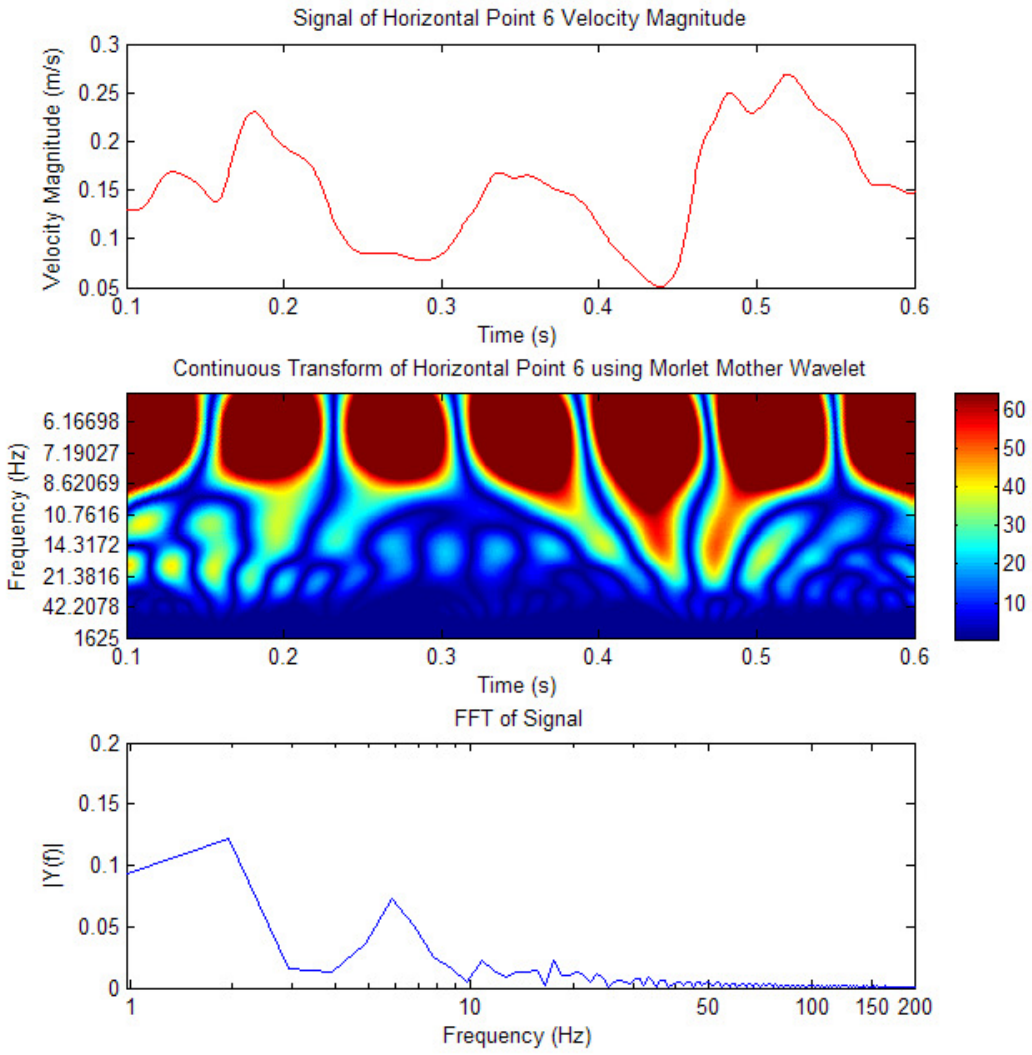

Figure 53. **Wavelet transform of horizontal point 6 using the Morlet mother wavelet**

After the shift in flow preference was observed between points 2 and 3, it seemed logical that the shift would also present itself in the signals throughout the rest of the domain. Points 7 through 12 all exhibited large changes in the dominant frequencies present between 0.4s and 0.6s. Point 7 was located behind a rod near the lower Re jet; however, while the flow from the high Re jet tended towards that side of the bundle (0.1s through 0.4s), the dominant frequency present was around 9

Hz. When the flow shifted to the other side of the channel, a well defined frequency around 18 Hz became clear in the decomposition shown in figure 54.

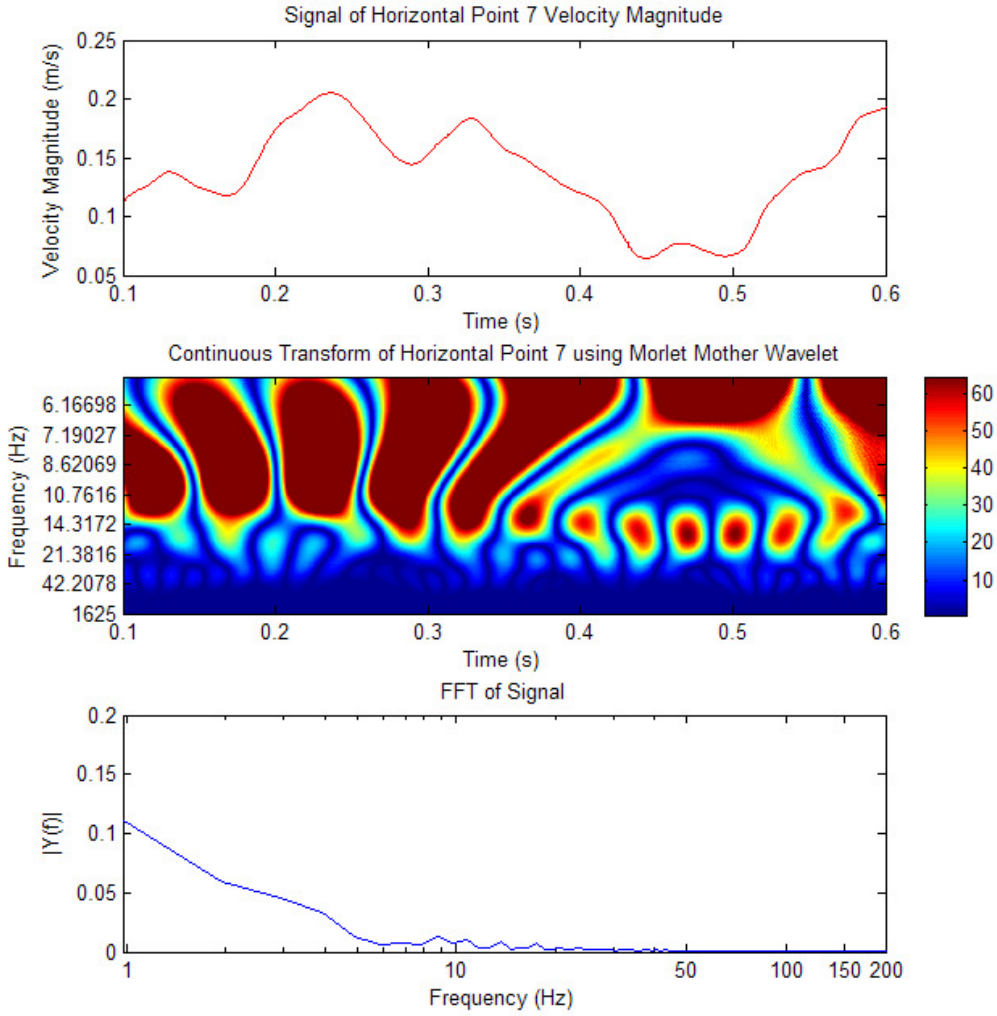

Figure 54. **Wavelet transform of horizontal point 7 using the Morlet mother wavelet**

The signal in point 9 (figure 55) showed a trend inverse of that seen in point 7 (figure 54). As the flow shifted, the frequency reduced and peaks in the intensity of the lower frequencies are seen while only faint remnants of the higher frequency remained. Velocities at points 9 and 10 (figures 55 and 56) were significantly lower than those recorded at points 7, 11, and 12 (figures 54, 57, and 58 respectively) due

to the larger shadow zone created both by the low Re jet flow past the two rods upstream of the points, and the flow of the high Re jet around the central rod causing a channeled flow away from these signal locations. It is in these locations that one might expect large dust particles with high inertia to be thrown from the main flow and deposited into piles.

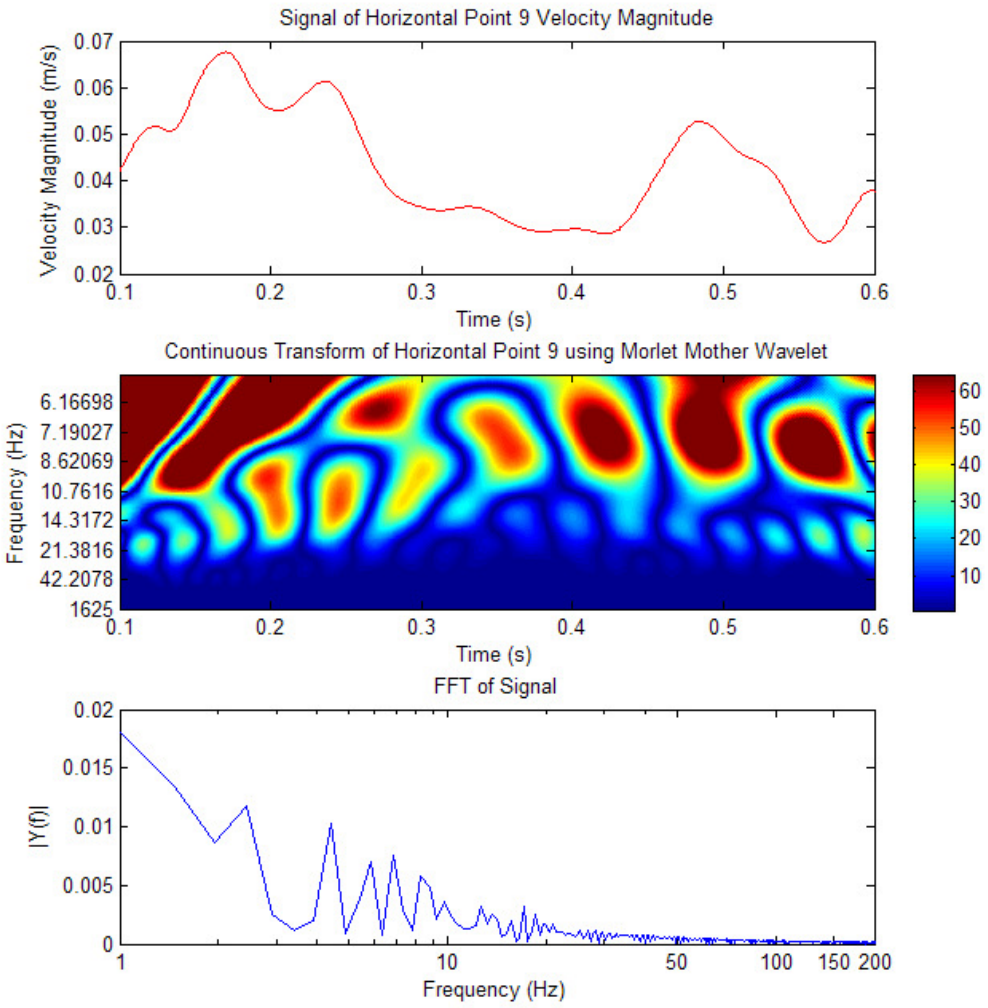

Figure 55. **Wavelet transform of horizontal point 9 using the Morlet mother wavelet**

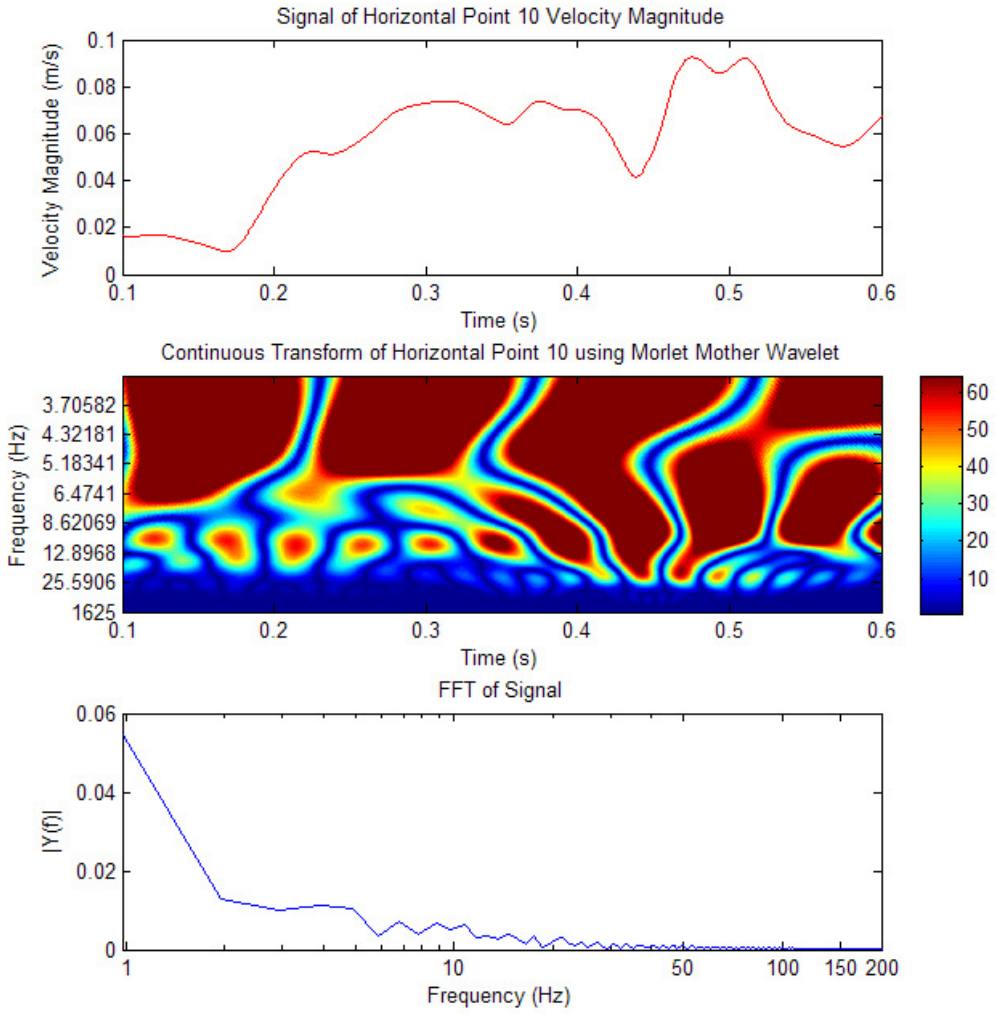

Figure 56. **Wavelet transform of horizontal point 10 using the Morlet mother wavelet**

Interpretation of the wavelet coefficient plots via comparison from one neighboring point to another emphasized the relationship between flow direction, dominant and overlapping frequencies, and how all of these frequencies contribute to the overall flow structure present in rod bundles. The coefficient plot obtained from the wavelet transform decomposition of the velocity magnitude signal at point 12 (figure 58) emphasized many of the advantages of this form of analysis.

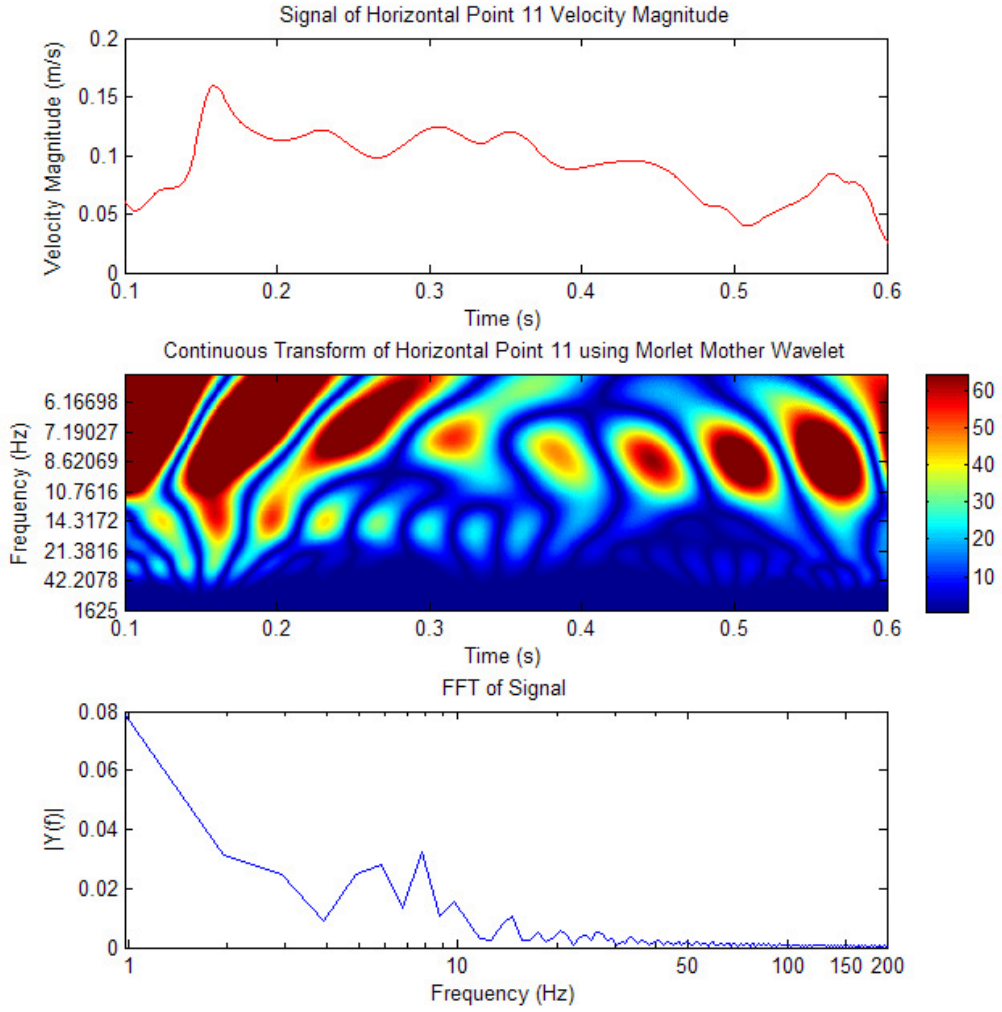

Figure 57. **Wavelet transform of horizontal point 11 using the Morlet mother wavelet**

Initially, very distinct frequencies at different scalesare present in the coefficient plot. Faint frequencies at the 26 Hz range seem to stem from the dominant entrainment frequency observed in the vertical mid-plane signal of the low Re jet (figure 51). Frequencies in the range of 12 Hz and 7 Hz are present in several locations in the horizontal plane as flow passes the rods and induces turbulent fluctuates in the wakes. As the flow transitioned around 0.4s on the high Re jet side, a strong increase in the sominant frequency was seen at point 12 by the moving from

4 Hz to 12 Hz between 0.4s and 0.55s. This form of analysis is very powerful in the understanding of unsteady flow structure interactions within the domain.

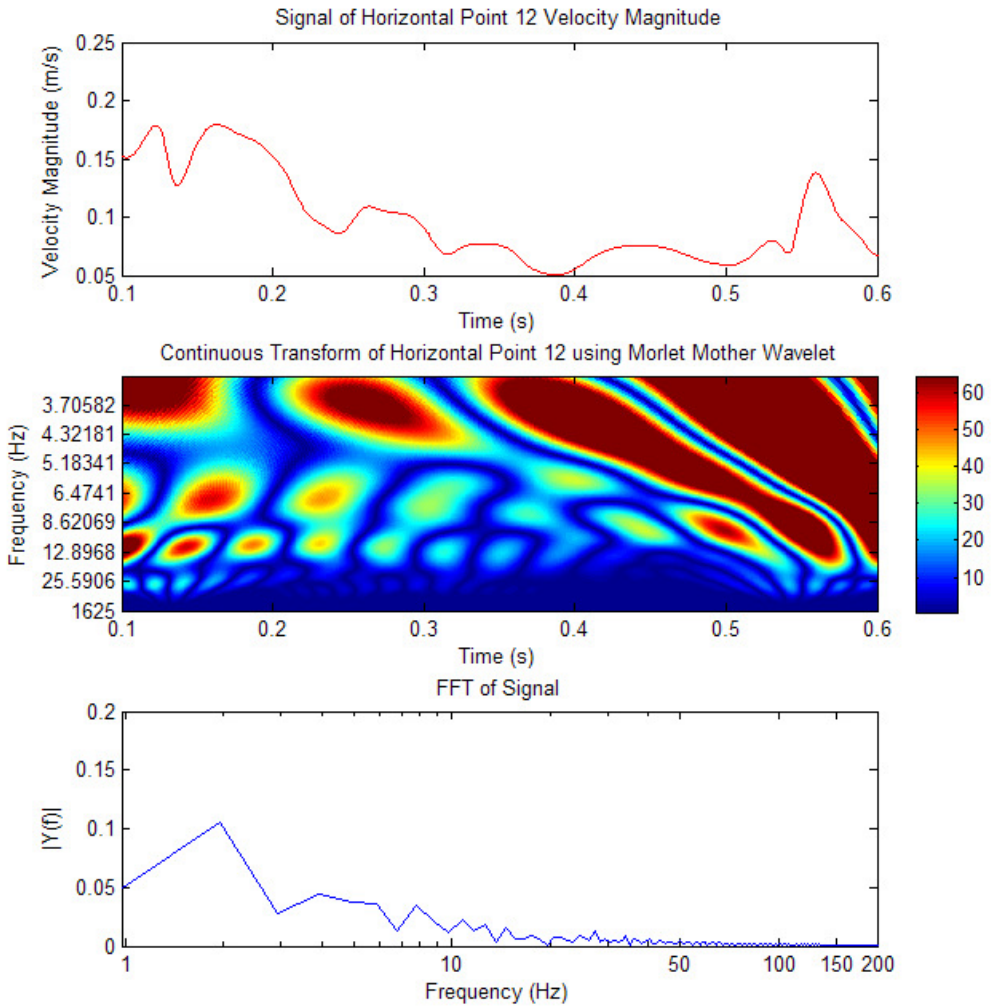

Figure 58. **Wavelet transform of horizontal point 11 using the Morlet mother wavelet**

4. CONCLUSIONS

In this study of jet flow mixing and interaction in a staggered rod bundle, proper guidelines were employed in the development of a computational grid that ensured the mesh limited the amount of error present in the numerical result due to factors other than the turbulence models employed. The discretized model offered acceptable results, but due to limitations in the computer cluster employed, further refinement of the mesh was not possible at the time of the study to obtain grid convergence criteria below 2% for all measured parameters. Despite this, global convergence orders were still between 2^{nd} and 4^{th} order. In future numerical studies of the same experimental setup, it would be beneficial to complete this simulation on a mesh with cells down to the 300μm range and time steps of 0.0001s. Such a mesh would be in the range of 50 million cells and would require a significantly larger cluster to perform the calculation.

The results of the work emphasized the importance of knowing the boundary conditions present in the actual VHTR and the difficulty faced when coupling 1 dimensional system codes to high fidelity 3 dimensional CFD simulations. Very little is known at the boundary condition in such couplings and as previous literature suggests, there is a high level of dependence on the inlet jet conditions. In this study, the inlet boundary conditions had a top-hat profile which is suspected to have led to an increase in vortex ring generation during jet entrainment than would have been present with round Gaussian jet profiles. Further work into the actual profile present in the lower plenum of the VHTR should be investigated as this profile

might have a profound influence on the level, frequency, and starting lengths Kelvin-Helmholtz instabilities.

All models both steady and unsteady identified the two primary vorticies present along the central rod with the Realizable k-ε turbulence model most closely modeling the vortex sizes of the time averaged experimental data [Amini and Hassan 2009]. The averaged large eddy simulation (LES) results overestimated vortex size, rotation rate, and vortex intensity compared to the experimental data. It is possible that by running additional time-steps the averaged result will approach the experimental data; however, the averaging of the unsteady result nearly defeats the purpose of running unsteady simulations from the start. Unsteady comparisons of vortex metrics including those mentioned as well as the drift in the vortex location over time would be particularly useful in understanding the vortex interaction.

Small horseshoe vortices present between the primary vorticies, the bottom plane, and the rods were observed in the LES results. Given sufficient wear particles present in the flow due to the release of graphite dust as coolant passes through the reactor core, these vorticies in the lower plenum should be investigated for possible locations of abrasion over the long lifespan of a reactor.

Future investigation of dust buildup in the shadow zones present in the bundle should be performed both experimentally and numerically. Experimentally this may be done by scaling the dust particle size and density appropriately to the test fluid being used and circulate the flow continuously until the particles have settled out. Numerically this may be done by performing LES simulations with a Lagrangian particle tracking solver.

Despite the discrepancy between the experimental data and the LES results, frequency information obtained through the analysis of the unsteady results using the fast Fourier transform (FFT) and the wavelet transform decomposition of the point signals throughout the domain provide useful insight into possible flow interactions. Well defined Kelvin-Helmholtz vortex formation occurred in the entrainment process of the jets as they entered the main fluid body. These vortex rings were generated with characteristic frequencies of 24Hz and 43Hz for the jets of Reynolds numbers 6,250 and 11,160 respectively. The ratios of the vortex shedding frequencies of the two jets to the ratio of the jet Reynolds numbers fell within 0.4% of one another.

Frequencies present following the staggered rods in the horizontal plane of the jet impingement at height y=2mm coincided with those estimated to be present in uniform flow past a cylinder by the Strouhal-Reynolds number relationship of Roshko and the correlation of Sr with shedding frequency. The caveat in relying on this relationship alone when using steady state results is the shift of frequencies as the flow fluctuates on the different scales, both locally and globally within the domain. Structurally speaking, analysis of the presence of consistent and well defined frequencies located at the base of the support structure in the lower plenum of the VHTR may or may not be an issue but should still be investigated. A multi-physics study coupling a CFD analysis using LES with structural finite element analysis methods in the support rods could provide a good insight into structural dynamics under different flow conditions in the lower plenum.

REFERENCES

Angrilli, F., Bergamaschi, S., Cossalter, V., 1982. Investigation of wall induced modifications to vortex shedding from a circular cylinder. J. of Fluids Eng., 104, 518-522.

Amini N., Hassan Y. A., 2009. PIV measurements of jet flows impinging into a channel containing a rod bundle using dynamic PIV. Int. J. of Heat and Mass Transfer, 52, (23-24), 5479-5495.

Bloor, S., 1963. The transition to turbulence in the wake of a circular cylinder. J. of Fluid Mech., 19, (2), 290-304.

CD-Adapco Group, 2008. Star-CCM+ Methodology and User Guide. Version 3.02.006.

Celik, I.B., Ghia, U., Roache, P.J., Freitas, C.J., Coleman, H., Raad, P.E., 2008. Procedure for estimation and reporting of uncertainty due to discretization in CFD applications. J. of Fluids Eng.,130 (7), 1-7.

Fey, U., König, M., Eckelmann, H., 1998. A new Strouhal-Reynolds number relationship for the circular cylinder in the range 47<Re<2e10. Physics of Fluids. 10, (7), 1547-1549.

Fourier, J., 1822. Théorie analytique de la Chaleur, Paris.

Greeley, R., Iversen, J.D., 1985. Wind as a Geological Process on Earth, Mars, Venus, and Titan. Cambridge Univ. Press, New York.

Goupillaud, P., Grossman, A., Morlet, J., 1984. Cycle-octave and related transforms in seismic signal analysis. Geoexploration, 23, 85-102.

Haar A. 1909. Zur theorie der orthogonalen Funktionensysteme. Mathematische Annalen, 69, 331–371.

Johnson, R.W., Guillen, D.P., Gallaway, T., 2006. Investigations of the application of CFD to flow expected in the lower plenum of the prismatic VHTR. Idaho National Laboratory. INL/EXT-06-11756, pp.53-54.

Jones, W.P., Luander, B.E. 1972. The prediction of laminarization with a two-equation model of turbulence. Int. J. of Heat and Mass Transfer, 15, 301-314.

Launder, B.E., Sharma, B.I., 1974. Application of the energy dissipation model of turbulence to the calculation of flow near a spinning disc. Letter in Heat and Mass Transfer, 1, (2), 131-138.

Lee, P.K., Johnson, J.L., 1978. High current brushes, Part II: effects of gases and hydrocarbon vapors. IEEE Transactions on Components, Hybrids, and Manufacturing Technology, CHMT-1, (1), 40-45.

Li, X., Gaddis, J.L., Wang, T., 2005. Multiple flow patterns and heat transfer in confined jet impingement. Int. J. of Heat and Fluid Flow. 26, (5), 746-754.

MacDonald, P.E., 2003. NGNP preliminary point design – results of the initial neutronics and thermal-hydraulics assessments. Idaho National Engineering and Environmental Laboratory. INEEL/EXT-03-00870, 17.

Mallat, S.G., 1989. A theory of multi-resolution signal decomposition: The wavelet representation. IEEE Trans. on Pattern Anal. Mach. Intel., 11, (7), 674–693.

McIlroy Jr., H.M., McEligot, D.M., Pink, R.J., 2008. Measurement of turbulent flow phenomena for the lower plenum of a prismatic gas-cooled reactor. Nucl. Eng. Des., doi:10.1016/j.nucengdes.2008.07.020

Misiti, M., Misiti, Y., Oppenheim, G., Poggi, J.-M., 2007. Wavelets and Their Applications. ISTE Ltd., pp. 2-6.

Möller, S.V., 1992. Single-phase turbulent mixing in rod bundles. Experimental Thermal and Fluid Science. 5, (1), 26-33.

Muzzammil, M., Gangadhariah, T., 2003. The mean characteristics of horseshoe vortex at a cylindrical pier. Journal of Hydraulic Research, 41, (3) 285-287.

New, T.H., Lim, T.T., Luo, S.C., 2006. Effects of jet velocity profiles on a round jet in cross-flow. Experiments in Fluids, 40, (6), 859-875.

Nicoud, F., Ducros, F., 1999. Subgrid-scale stress modelling based on the square of the velocity gradient tensor. Flow, Turbulence and Combustion, 62, 183-200.

Pardee, R.P., 1967. Moisture dependence of silver-graphite brushes in air, nitrogen, helium, and carbon dioxide. IEEE Transactions on Power Apparatus and Systems. 86, (5), 616-625.

Rehme, K., 1989. Experimental observations of turbulent flow through subchannels of rod bundles. Experimental Thermal and Fluid Science, 2, (3), 341-349.

Roache, P.J., Ghia, K., White, F., 1986. Editorial policy statement on the control of numerical accuracy. ASME Journal of Fluids Engineering, 108, (1), 2.

Roache, P.J., 1998. Verification and validation in computational science and engineering. Hermosa Publishers. Albuquerque, New Mexico.

Rodriguez, S.B., El-Genk, M.S., 2009. Numerical investigation of potential elimination of 'hot streaking' and stratification in the VHTR lower plenum using helicoid inserts. Nuclear Eng. And Design, 240 (5) 995-1004.

Roshko, A., 1954. On the development of turbulent wakes from vortex streets. National Advisory Committee for Aeronautics, rpt. 1191.

Savage, R.H., 1948. Graphite lubrication. Journal of Applied Physics, 19, (1), 1-10.

Shih, T.-H., Liou, W.W., Shabbir, A., Yang, Z., Zhu, J., 1995. A new k-ε eddy viscosity model for high reynolds number turbulent flows -- model development and validation. Computers and Fluids, 24, (3), 227-238.

Shu, F., Plesniak, M.W., Sojka, P.E., 2005. Intermediate-origin nozzles to control jet structure and evolution, J. of Turbulence, 6, (26), 2-18.

Xu, G., Zhou, Y., 2004. Strouhal numbers in the wake of two inline cylinders. Expt. In Fluids. 248-256.

APPENDIX A

ALTERNATE SENSITIVITY STUDY

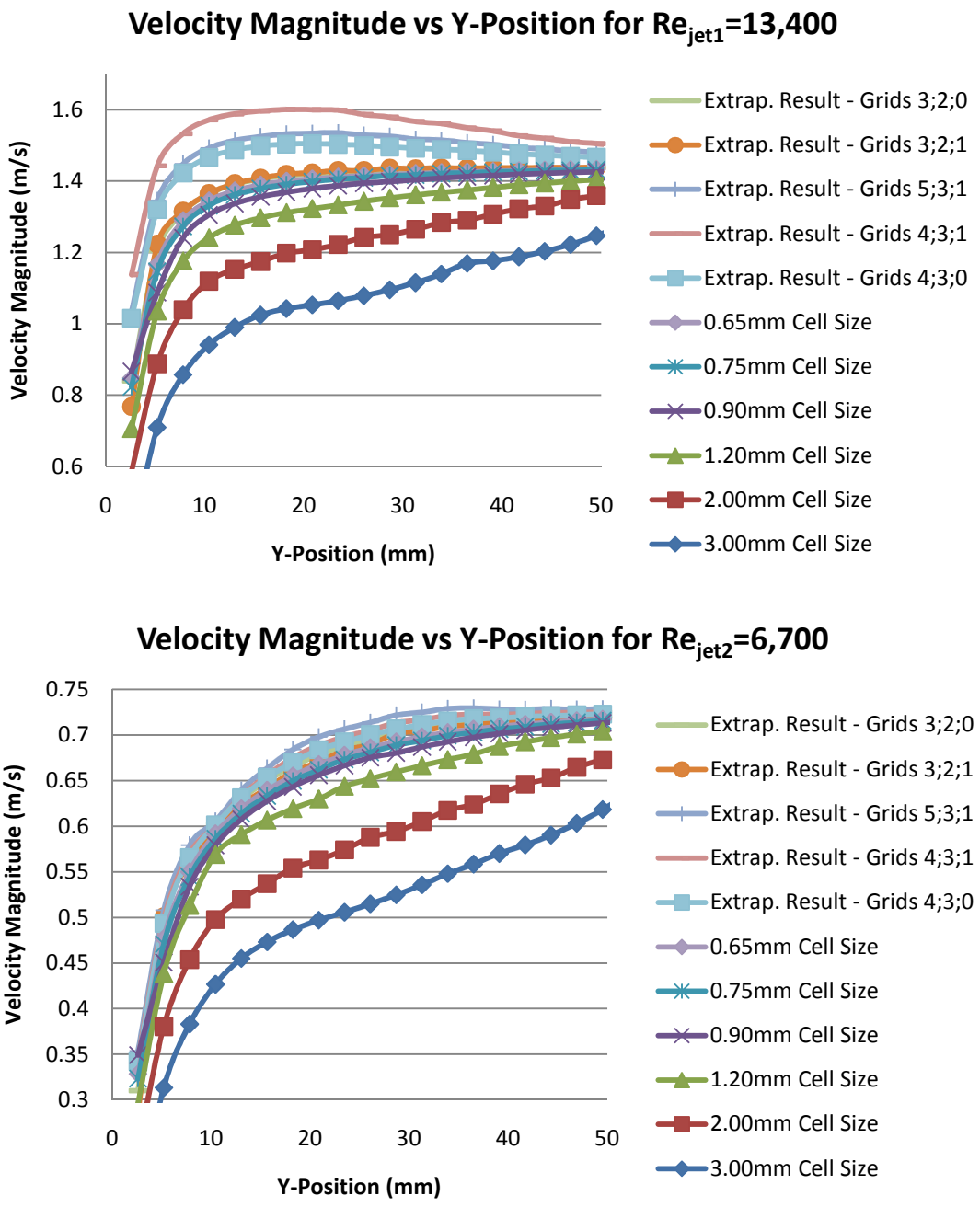

Figure 59. **Extrapolated results directly below inlet jets Re$_{jet1}$=13,700 and Re$_{jet2}$=6,700**

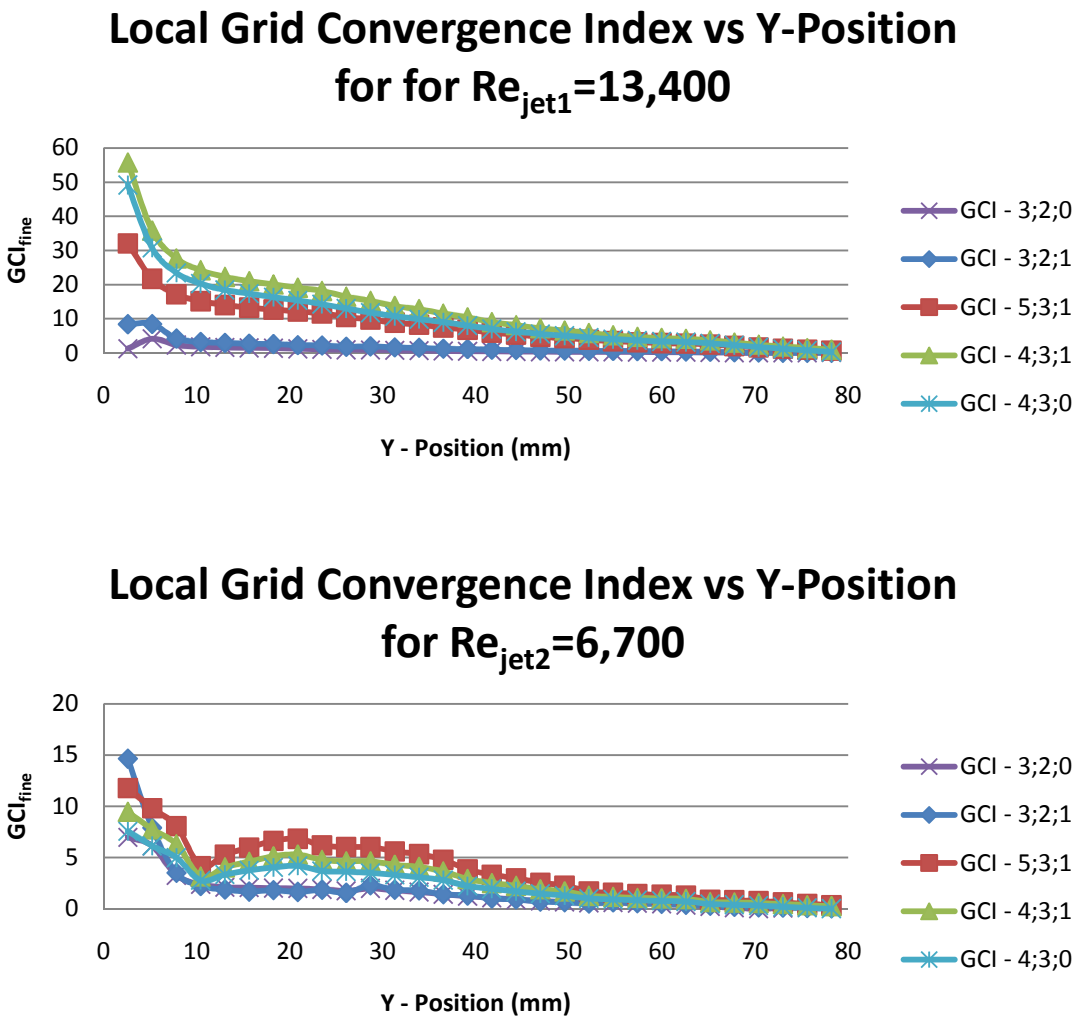

Figure 60. **Grid Convergence Indices directly below inlet jets Re$_{jet1}$=13,400 and Re$_{jet2}$=6,700**

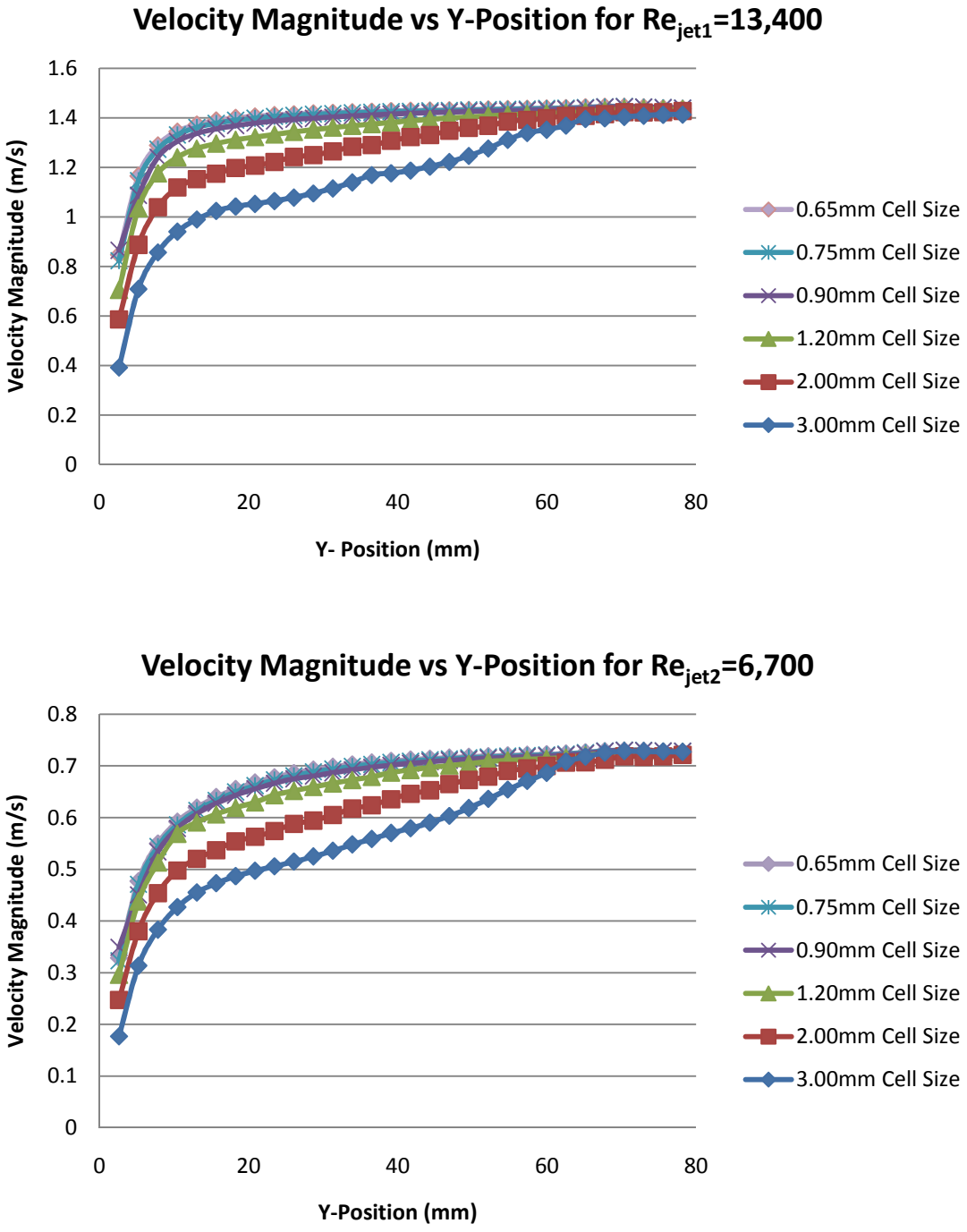

Figure 61. **Axial flow velocity directly below inlet jets Re$_{jet1}$=13,400 and Re$_{jet2}$=6,700**

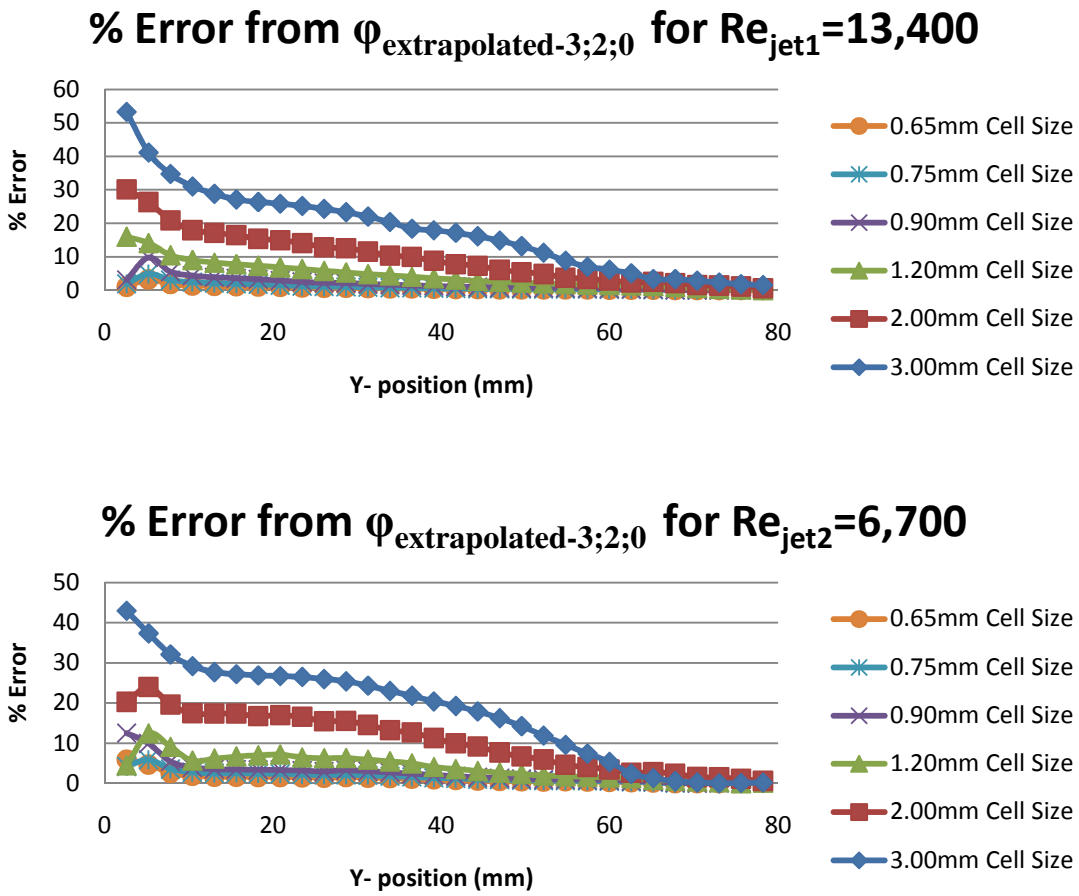

Figure 62. **Error from each grid size to the result extrapolated from grids 3, 2, and 0 for Re_{jet1}=13,700 and Re_{jet2}=6,700**

APPENDIX B

ADDITIONAL WAVELET TRANSFORM DECOMPOSITIONS

B.1 Vertical Mid-plane Points

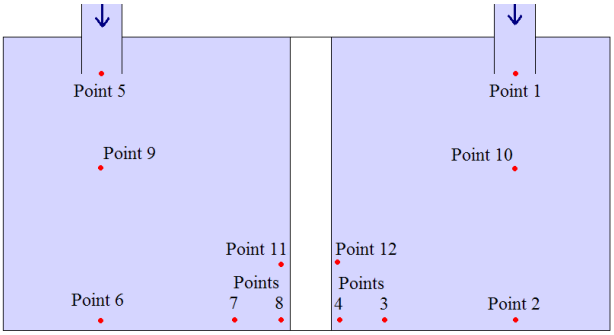

Figure 63. **Extraction point locations for wavelet analysis**

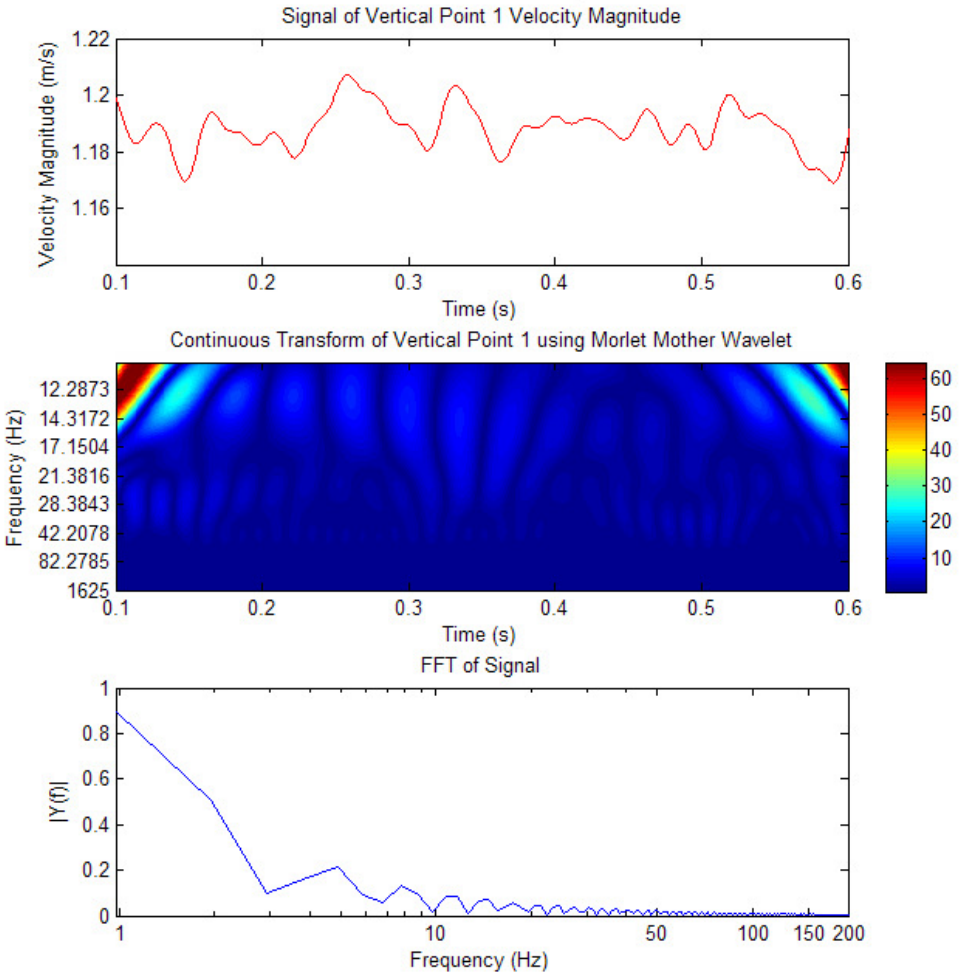

Figure 64. **Wavelet transform of vertical point 1 using the Morlet mother wavelet**

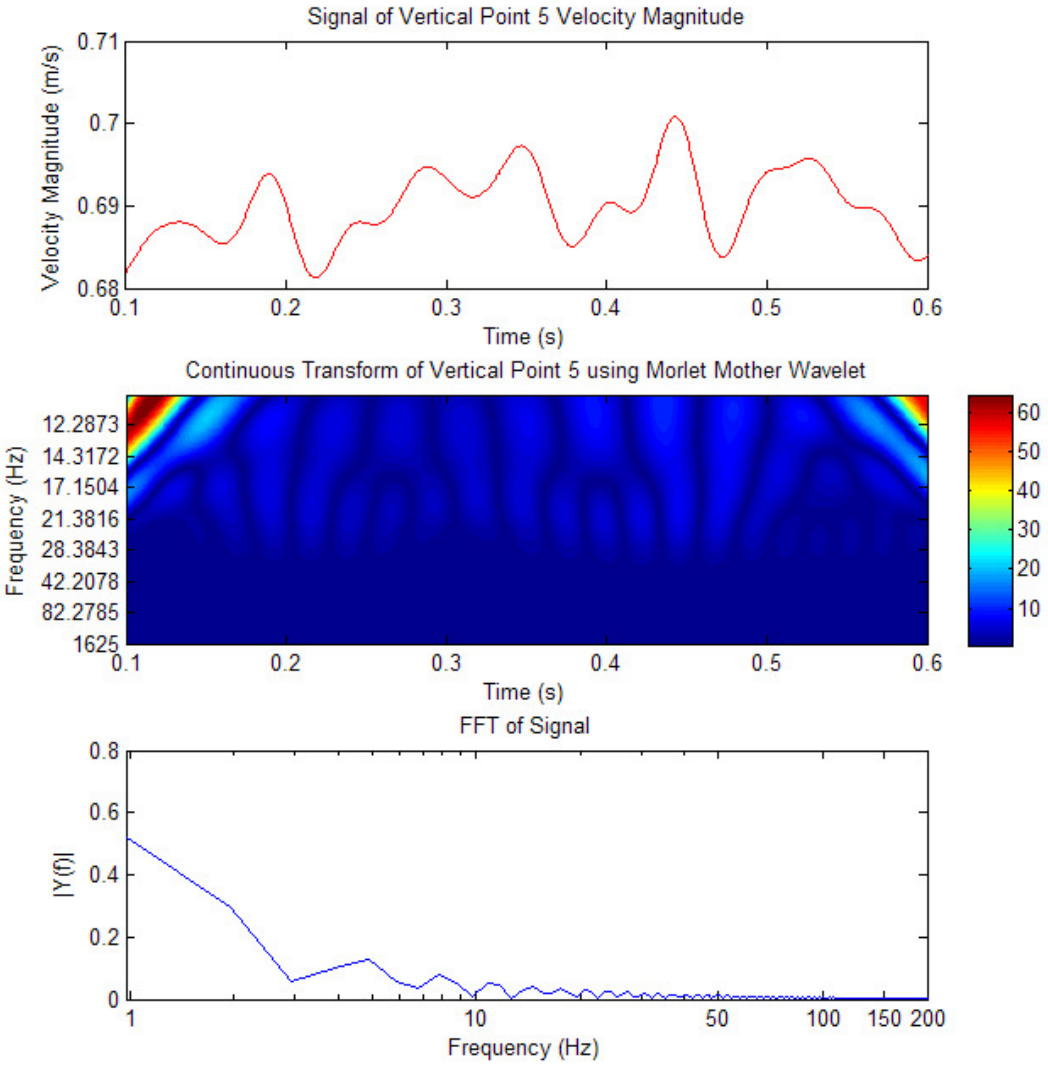

Figure 65. **Wavelet transform of vertical point 5 using the Morlet mother wavelet**

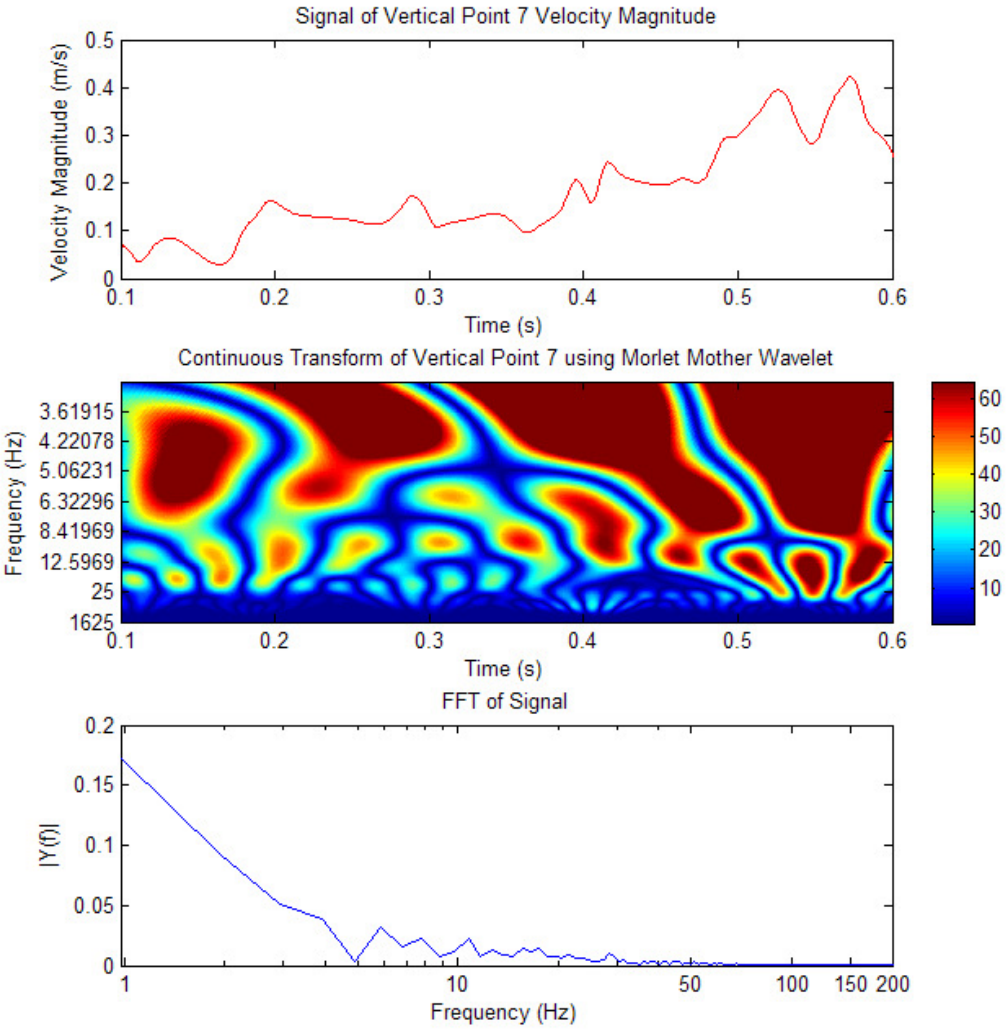

Figure 66. **Wavelet transform of vertical point 7 using the Morlet mother wavelet**

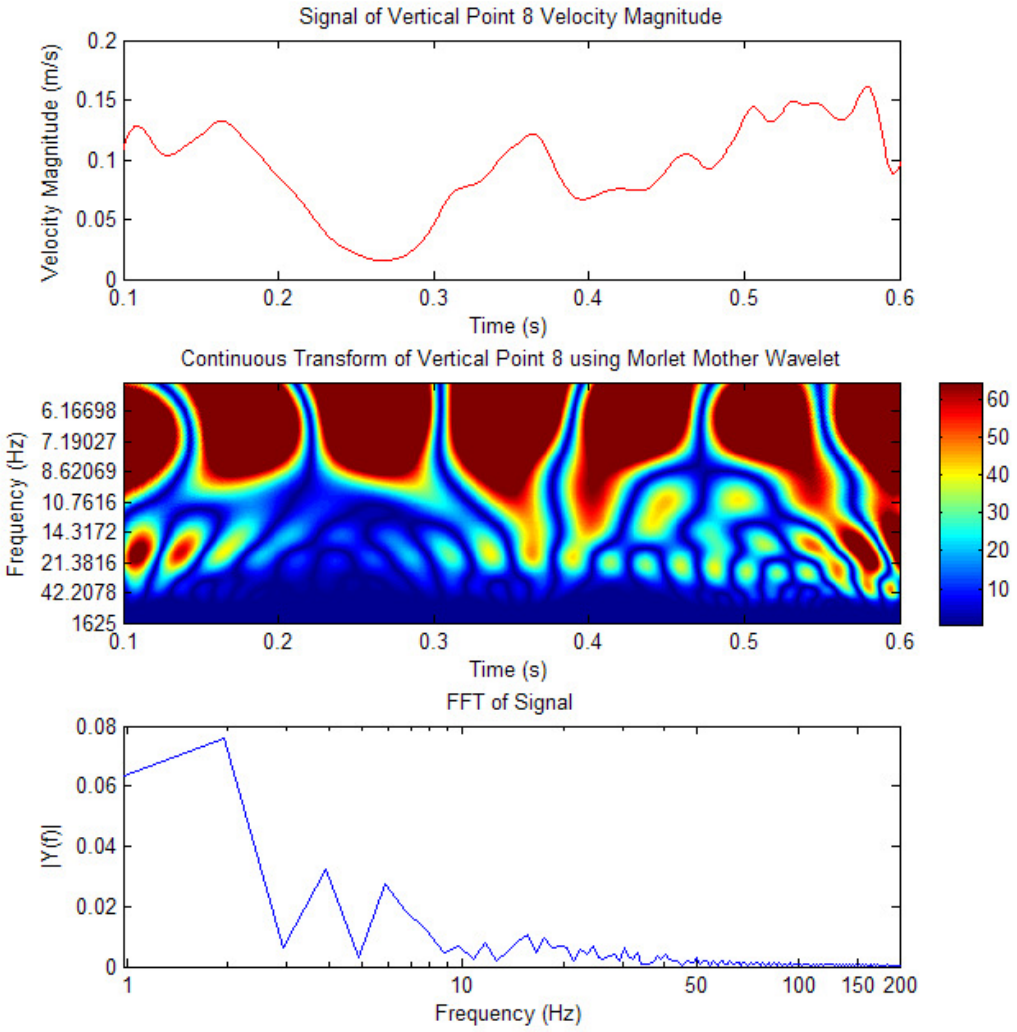

Figure 67. **Wavelet transform of vertical point 8 using the Morlet mother wavelet**

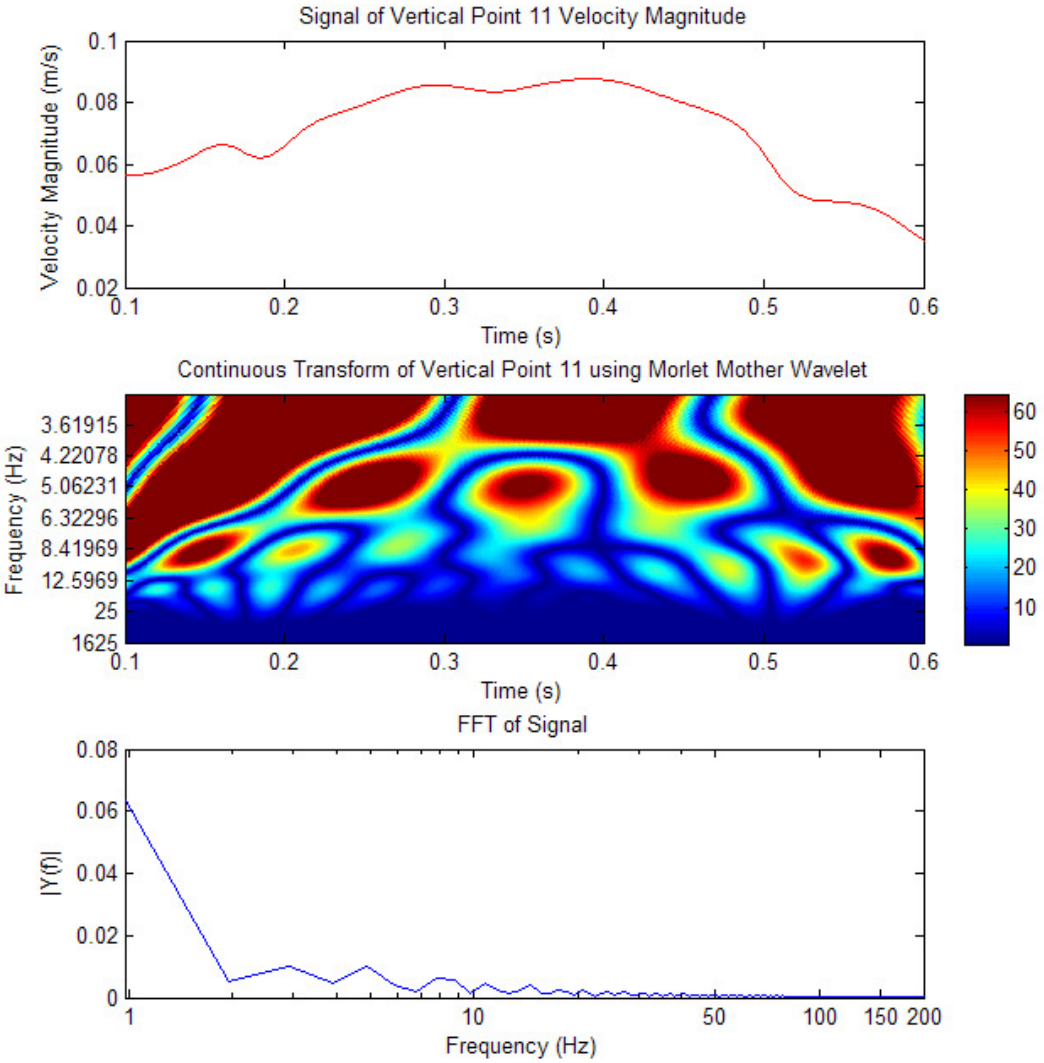

Figure 68. **Wavelet transform of vertical point 11 using the Morlet mother wavelet**

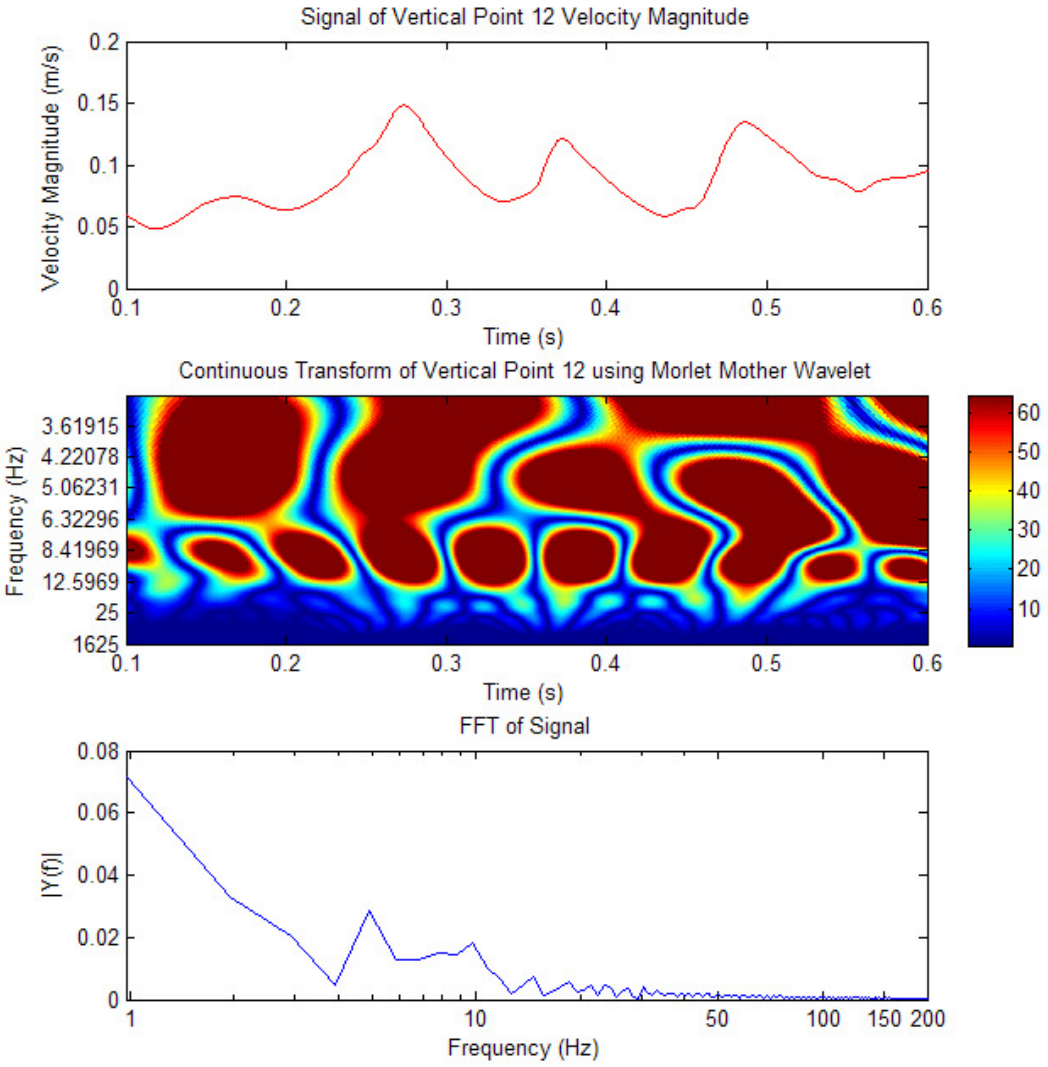

Figure 69. **Wavelet transform of vertical point 12 using the Morlet mother wavelet**

B.2 Horizontal plane points at y=2mm

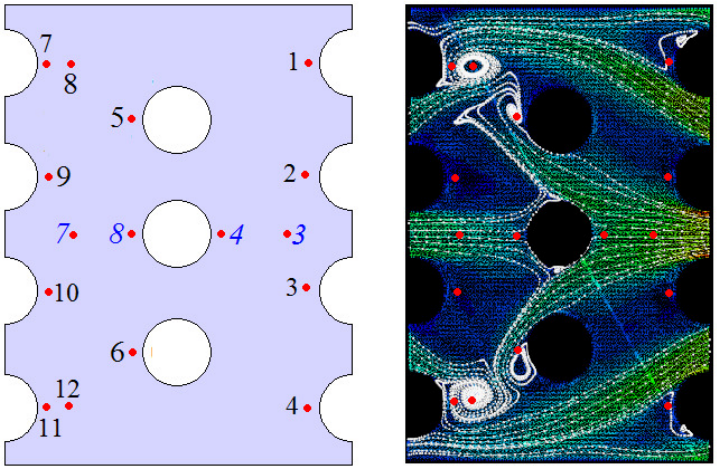

Figure 70. **Locations of signal probes in the horizontal plane 2mm from the bottom plane. Numbers in blue signify the points previously obtained in the vertical mid-plane**

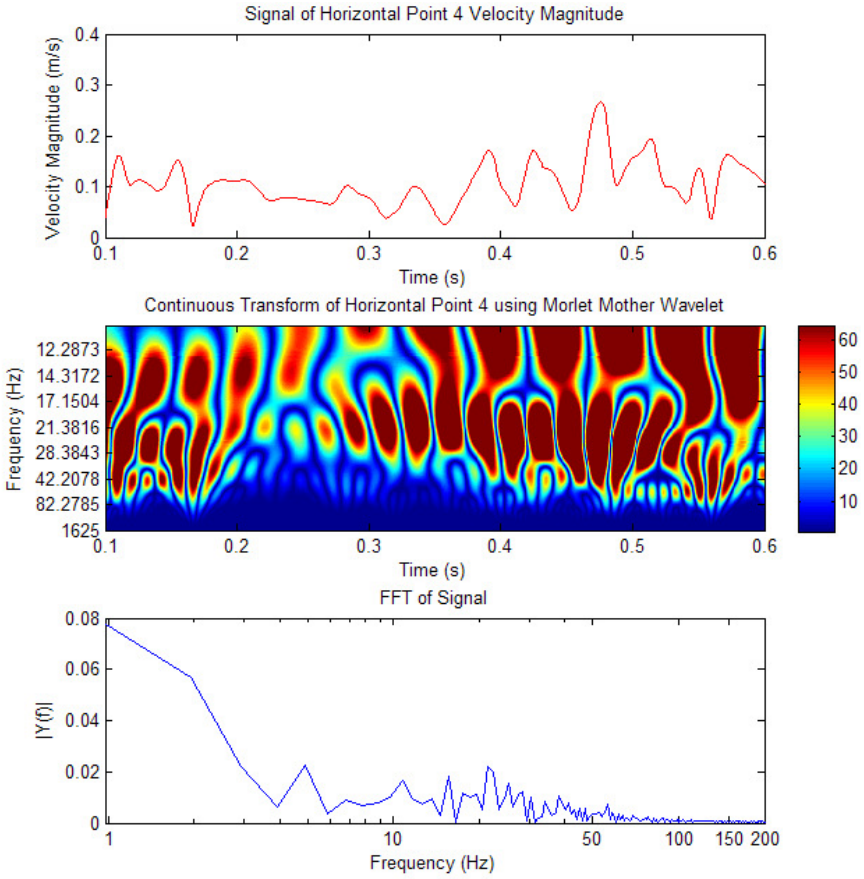

Figure 71. **Wavelet transform of horizontal point 4 using the Morlet mother wavelet**

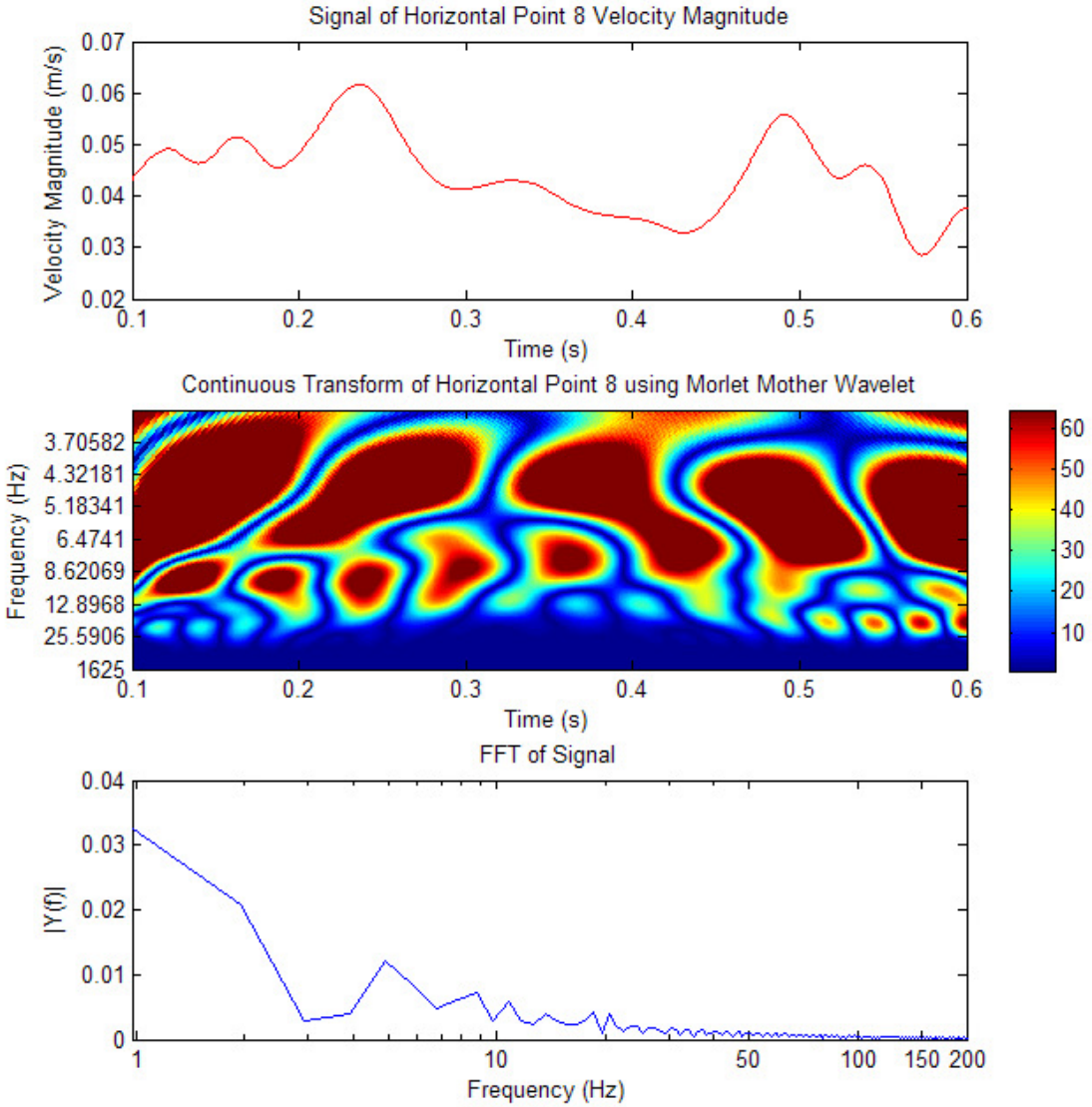

Figure 72. **Wavelet transform of horizontal point 8 using the Morlet mother wavelet**

APPENDIX C

CODES AND MACROS

C.1 Macro for result acquisition during LES simulation. Written for Star-CCM+ v3.06.006

```
// Macro by Nathaniel Salpeter
// Copyright 2008 Texas A&M University

//Macro is designed to run timesteps
// Tasks while running include:
//     Exporting desired scenes to the desired locations every 5
timesteps, changing the filename
//     Exporting desired tables to the desired locations every 1
timesteps, changing the filename
//     Saving the simulation to the desired location ever 50 timesteps,
stepping the filename

//  The above locations and intervals may be adjusted as necessary.

package macro;

import java.util.*;

import star.common.*;
import star.vis.*;
import star.base.neo.*;


public class LESspectralmacro extends StarMacro {

  public void execute() {

int FileName ; FileName=0;
int TimeStep ;

//LES-5-2.8 small jet fluctuation path
String path11 = "/emchome/natesal/Rod Bundle/LES/backupsimfiles/5-
28gpmLES/small-rod-fluctuation-imgs/";
//LES-5-2.8 large jet fluctuation path
String path12 = "/emchome/natesal/Rod Bundle/LES/backupsimfiles/5-
28gpmLES/large-rod-fluctuation-imgs/";
//LES-6-3 Mid Vector Scene location
String path13 = "/emchome/natesal/Rod Bundle/LES/backupsimfiles/5-
28gpmLES/vert-mid-imgs/";
//LES-6-3 large Mid Vector Scene location
String path14 = "/emchome/natesal/Rod Bundle/LES/backupsimfiles/5-
28gpmLES/vert-mid-lg-imgs/";
```

```
//LES-5-2.8 small jet table path-high
String path1211 = "/emchome/natesal/Rod Bundle/LES/backupsimfiles/5-
28gpmLES/small-rod-fluctuation-tbl/high/";
//LES-5-2.8 small jet table path-low
String path1212 = "/emchome/natesal/Rod Bundle/LES/backupsimfiles/5-
28gpmLES/small-rod-fluctuation-tbl/low/";
//LES-5-2.8 large jet table path
String path22 = "/emchome/natesal/Rod Bundle/LES/backupsimfiles/5-
28gpmLES/large-rod-fluctuation-tbl/";
//LES-6-3 Mid table location
String path23 = "/emchome/natesal/Rod Bundle/LES/backupsimfiles/5-
28gpmLES/vert-mid-tbl/";
//LES-6-3 Mid table location
String path24 = "/emchome/natesal/Rod Bundle/LES/backupsimfiles/5-
28gpmLES/vert-mid-lg-tbl/";


//Set save location
String path3 = "/emchome/natesal/Rod Bundle/LES/backupsimfiles/5-
28gpmLES/periodic-saves/";


StringBuffer path211 = new StringBuffer("") ;
StringBuffer path212 = new StringBuffer("") ;
StringBuffer path213 = new StringBuffer("") ;
StringBuffer path214 = new StringBuffer("") ;

StringBuffer path221 = new StringBuffer("") ;
StringBuffer path222 = new StringBuffer("") ;
StringBuffer path223 = new StringBuffer("") ;
StringBuffer path224 = new StringBuffer("") ;


StringBuffer path32 = new StringBuffer("") ;

    Simulation simulation_0 =
      getActiveSimulation();

for(int i = 1; i < 10000; i++){

    FileName = FileName + 1 ;

//getTime

double currentTime=getActiveSimulation().getSolution().getPhysicalTime();

    simulation_0.getSimulationIterator().step(1, true);

if (i % 5 == 0){

    Scene scene_0 =
      simulation_0.getSceneManager().getScene("small-jets-fluctuations");
```

```
path211.append("LES-5-2,8-sml-Hjets-ST-
").append(currentTime).append(".png") ;
scene_0.printAndWait(resolvePath(path11 + path211.toString()), 1, 800,
600);
path211.delete(0,path211.length());

   Scene scene_1 =
      simulation_0.getSceneManager().getScene("large-horiz-
fluctuations");

path212.append("LES-5-2,8-lg-Hjets-ST-
").append(currentTime).append(".png") ;
scene_1.printAndWait(resolvePath(path12 + path212.toString()), 1, 1000,
800);
path212.delete(0,path212.length());

    Scene scene_6 =
      simulation_0.getSceneManager().getScene("high-vert-mid-const");

path213.append("LES-5-2,8-vert-high-mid-ST-
").append(currentTime).append(".png") ;
scene_6.printAndWait(resolvePath(path13 + path213.toString()), 1, 800,
600);
path213.delete(0,path213.length());

    Scene scene_7 =
      simulation_0.getSceneManager().getScene("all-vert-mid-const");

path214.append("LES-5-2,8-vert-lg-mid-ST-
").append(currentTime).append(".png") ;
scene_7.printAndWait(resolvePath(path14 + path214.toString()), 1, 800,
600);
path214.delete(0,path214.length());

}

    XyzInternalTable xyzInternalTable_4 =
      ((XyzInternalTable) simulation_0.getTableManager().getTable("all-
vert-mid"));

xyzInternalTable_4.extract();

    path224.append("LES-5-2,8-vert-all-ST-
").append(currentTime).append(".csv") ;
    xyzInternalTable_4.export(resolvePath(path24 + path224.toString()),
2);
    path224.delete(0,path224.length());



    XyzInternalTable xyzInternalTable_3 =
      ((XyzInternalTable) simulation_0.getTableManager().getTable("high-
jet-2mmhoriz-small"));

xyzInternalTable_3.extract();
```

```
    path221.append("LES-5-2,8-high-sml-Hjet-ST-
").append(currentTime).append(".csv") ;
    xyzInternalTable_3.export(resolvePath(path1211 + path221.toString()),
2);
    path221.delete(0,path221.length());


    XyzInternalTable xyzInternalTable_2 =
      ((XyzInternalTable) simulation_0.getTableManager().getTable("low-
jet-2mmhoriz-small"));

xyzInternalTable_2.extract();

    path221.append("LES-5-2,8-low-sml-Hjet-ST-
").append(currentTime).append(".csv") ;
    xyzInternalTable_2.export(resolvePath(path1212 + path221.toString()),
2);
    path221.delete(0,path221.length());

    XyzInternalTable xyzInternalTable_1 =
      ((XyzInternalTable) simulation_0.getTableManager().getTable("full-
horiz-2mm-3rows"));

xyzInternalTable_1.extract();

    path222.append("LES-5-2,8-horiz-lg-ST-
").append(currentTime).append(".csv") ;
    xyzInternalTable_1.export(resolvePath(path22 + path222.toString()),
2);
    path222.delete(0,path222.length());

    XyzInternalTable xyzInternalTable_0 =
      ((XyzInternalTable) simulation_0.getTableManager().getTable("Mid
Plane Table"));

xyzInternalTable_0.extract();

    path223.append("LES-5-2,8-vert-high-ST-
").append(currentTime).append(".csv") ;
    xyzInternalTable_0.export(resolvePath(path23 + path223.toString()),
2);
    path223.delete(0,path223.length());

    if (i % 100 == 0){

path32.append("LES-5-2,8-ST-@").append(currentTime).append(".sim") ;
simulation_0.saveState(resolvePath(path3 + path32.toString()));
path32.delete(0,path32.length());

    }

    }
  }
}
```

C.2 Program for preparing LES results of wavelet transform decomposition. Written for Matlab v. R2007a.

```
% This program performs averaging on the results as well as splitting
instantaneous velocity components into files

length=187797;  % length of data file
tmin=32.3000;   % Initial Time
tmax=33.0120;   % End Time

sectionlength=187797;

sections=ceil(length/sectionlength);

sectionnumb=0;
sectionstart=0;
sectionend=0;

for i=1:sections;
    if (i == 1);
    sectionstart=1;
    elseif (i ~=1);
    sectionstart=(i-1)*sectionlength;
    end
    if (i ~= sections);
    sectionend=(i)*sectionlength-1;
    elseif (i== sections);
    sectionend=length;
    end

% Go to numericfilezoomed subroutine
 [numb,count,velmag,velx,vely,velz,Z]=
numericfilezoomed(sectionstart,sectionend,tmin,tmax,length);


velmagFN = sprintf('STvelmag%d.csv',sectionnumb);
    dlmwrite(velmagFN, velmag)
velxFN = sprintf('STvelx%d.csv',sectionnumb);
    dlmwrite(velxFN, velx)
velyFN = sprintf('STvely%d.csv',sectionnumb);
    dlmwrite(velyFN, vely)
velzFN = sprintf('STvelz%d.csv',sectionnumb);
    dlmwrite(velzFN, velz)




% Go to numericaveragezoom subroutine
```

```
[AveTotal,xpos,ypos,zpos]=
numericaveragezoom(sectionstart,sectionend,sectionlength,numb,count,secti
onnumb,length,velmag,velx,vely,velz,Z);

xposFN = sprintf('STxpos%d.csv',sectionnumb);
    dlmwrite(xposFN, xpos)
yposFN = sprintf('STypos%d.csv',sectionnumb);
    dlmwrite(yposFN, ypos)
zposFN = sprintf('STzpos%d.csv',sectionnumb);
    dlmwrite(zposFN, zpos)
AveTotalFN = sprintf('STAveTotal%d.csv',sectionnumb);
    dlmwrite(AveTotalFN, AveTotal)

    clear xpos
    clear ypos
    clear zpos
    clear Z


end




function[numb,count,velmag,velx,vely,velz,Z]=
numericfilezoomed(sectionstart,sectionend,tmin,tmax,length)

    numb=1;
tmin=32.3000;
tmax=33.0120;



for n=tmin:0.0005:tmax;
   count=1;

FileName = sprintf('LES-5-2,8-vert-all-ST-%e.csv',n);
time=n;
 if ispc
    FileName = strrep(FileName, 'e+0', 'e+00');
 end


fprintf(FileName);
fprintf('  ');
Z(1)=importdata(FileName);
```

```
for p=sectionstart:sectionend;

    velmagV=Z(1).data(p,1);
    velxV=Z(1).data(p,2);
    velyV=Z(1).data(p,3);
    velzV=Z(1).data(p,4);

    velmag(count,numb)=single(velmagV);
    velx(count,numb)=single(velxV);
    vely(count,numb)=single(velyV);
    velz(count,numb)=single(velzV);

        if (p ~=sectionend);
        count=count+1;
        end
    end

if (n ~= tmax);
numb=numb+1;
end

end
    clear velmagV;
    clear velxV;
    clear velyV;
    clear velzV;

return



function[AveTotal,xpos,ypos,zpos]=
numericaveragezoom(sectionstart,sectionend,sectionlength,numb,count,secti
onnumb,length,velmag,velx,vely,velz,Z)

numb=numb-1;

      count=1;
if (sectionstart==1);
    countmax=sectionend;
elseif (sectionstart ~= 1);
    countmax=sectionend-sectionstart;
end

for p=sectionstart:sectionend;

    xposV=Z(1).data(p,5);
    yposV=Z(1).data(p,6);
    zposV=Z(1).data(p,7);
    xpos(count,1)=single(xposV);
    ypos(count,1)=single(yposV);
    zpos(count,1)=single(zposV);
```

```
     count=count+1;
    end

    clear xposV;
    clear yposV;
    clear zposV;

for p=1:countmax;
    Avevelmag(p)=0;
    Avevelx(p)=0;
    Avevely(p)=0;
    Avevelz(p)=0;

    end

for n=1:numb;
for p=1:countmax;

    Avevelmag(p)=velmag(p,n)+Avevelmag(p);
    Avevelx(p)=velx(p,n)+Avevelx(p);
    Avevely(p)=vely(p,n)+Avevely(p);
    Avevelz(p)=velz(p,n)+Avevelz(p) ;

end
end

    for p=1:countmax;

    Avevelmag(p)=Avevelmag(p)/numb;
    Avevelx(p)=Avevelx(p)/numb;
    Avevely(p)=Avevely(p)/numb;
    Avevelz(p)=Avevelz(p)/numb;

    end

    Avevelmag=Avevelmag';
    Avevelx=Avevelx';
    Avevely=Avevely';
    Avevelz=Avevelz';

    % recombine phase

    for p=1:countmax;
    AveTotal(p,1)=Avevelmag(p);
    AveTotal(p,2)=Avevelx(p);
    AveTotal(p,3)=Avevely(p);
    AveTotal(p,4)=Avevelz(p);
    AveTotal(p,5)=xpos(p,1);
    AveTotal(p,6)=ypos(p,1);
    AveTotal(p,7)=zpos(p,1);
```

```
    end

    return


% Export point data for wavelet decomposition.


numb=1424;
    u=importdata('STvelz1.csv');

for p=1:12;
    for n=1:numb;
usignal(p,n)=0;

    end
end

    for n=1:numb;
         usignal(1,n)=u(6161,n);
         usignal(2,n)=u(73384,n);
         usignal(3,n)=u(65283,n);
         usignal(4,n)=u(58929,n);
         usignal(5,n)=u(137984,n);
         usignal(6,n)=u(163580,n);
         usignal(7,n)=u(93432,n);
         usignal(8,n)=u(115139,n);
         usignal(9,n)=u(164705,n);
         usignal(10,n)=u(6702,n);
         usignal(11,n)=u(102368,n);
         usignal(12,n)=u(59660,n);
    end

    dlmwrite('STvelz-points.csv', usignal);
```

C.3 Program for performing wavelet transform decomposition and the Fast Fourier Transform. Written for Matlab v. R2007a.

```
reset(0);
whitebg
i=9
figure('Position',[0,0,700,700]);
Fs = 2000;                      % Sample rate
lv = 2848*0.0005;               % # of samples multiplied by timestep
signal = y(i,1:lv*2000);
T = 1/Fs;                       % Sample time
L = 2848;                       % Length of signal
t = (0:L-1)*T;

set(subplot(3,1,1),'Xtick',[]);
plot(signal,'r');
title('Signal of Horizontal Point 9 Velocity Magnitude');
xlabel('Time (s)')
ylabel('Velocity Magnitude (m/s)')
set(gca,'Xlim',[200 1200])
set(gca,'XTick',[200:200:1200])
croppedtimelabels = ['0.1';
          '0.2';
          '0.3';
          '0.4';
          '0.5';
          '0.6'];
set(gca,'XTickLabels',croppedtimelabels)
subplot(3,1,2);

set(subplot(3,1,2),'Xtick',[]);
subplot(3,1,2);
maxscale=300;
scales = (1:maxscale);
wname='morl';
cwt(signal,scales,wname,'plot');
colormap(Jet(64));
title('Continuous Transform of Horizontal Point 9 using Morlet Mother
Wavelet');
ylabel('Frequency (Hz)');
xlabel('Time (s)')
tt = get(gca,'Yticklabel');
[r,c] = size(tt);
yl = char(32*ones(r,c));
for k = 1:3:r , yl(k,:) = tt(k,:); end
set(gca,'YLim',[1 maxscale]);
set(gca,'YTick',[1:(maxscale/8):maxscale])

for n=1:9
    temp(n)=1+(maxscale/8)*(n-1);
freqlabel(n)=scal2frq(temp(n),wname,1/Fs);
```

```
freqlabel2(n)=1/(temp(n)*0.0005);
end

set(gca,'Yticklabel',freqlabel);
set(gca,'XLim',[200 1200]);
set(gca,'XTick',[200:200:1200])
croppedtimelabels = ['0.1';
          '0.2';
          '0.3';
          '0.4';
          '0.5';
          '0.6'];
set(gca,'XTickLabels',croppedtimelabels)


subplot(3,1,3);
set(subplot(3,1,3),'Xtick',[]);
plot(Fs*t(1:1424),signal(1:1424))
title('Signal Corrupted with Zero-Mean Random Noise')
xlabel('time (milliseconds)')
NFFT = 2^nextpow2(L);
Y = fft(signal,NFFT)/L;
f = Fs/2*linspace(0,1,NFFT/2+1);

semilogx(f,2*abs(Y(1:NFFT/2+1)),'blue')
title('FFT of Signal')
xlabel('Frequency (Hz)')
set(gca,'XLim',[1 200]);
set(gca,'XTick',[1,10,50,100,150,200])
ylabel('|Y(f)|')
```

VITA

Name: Nathaniel O. Salpeter

Address: Texas A&M University
Department of Mechanical Engineering
3123 TAMU
College Station TX 77843-3123

Email Address: nsalpeter@gmail.com

Education: B.S., Mechanical Engineering, University of Florida, 2007
M.S., Mechanical Engineering, Texas A&M University, 2010